REAL-TIME EVALUATION OF STIMULATION AND DIVERSION IN HORIZONTAL WELLS

A Dissertation

by

SEYED MOHAMMAD TABATABAEI BAFRUEI

Submitted to the Office of Graduate Studies of
Texas A&M University
in partial fulfillment of the requirements for the degree of

DOCTOR OF PHILOSOPHY

December 2011

Major Subject: Petroleum Engineering

Real-Time Evaluation of Stimulation and Diversion in Horizontal Wells

REAL-TIME EVALUATION OF STIMULATION AND DIVERSION IN HORIZONTAL WELLS

A Dissertation

by

SEYED MOHAMMAD TABATABAEI BAFRUEI

Submitted to the Office of Graduate Studies of
Texas A&M University
in partial fulfillment of the requirements for the degree of

DOCTOR OF PHILOSOPHY

Approved by:

Chair of Committee,	Ding Zhu
Committee Members,	A. Daniel Hill
	Christine Ehlig-Economides
	Wayne M. Ahr
Head of Department,	Stephen A. Holditch

December 2011

Major Subject: Petroleum Engineering

ABSTRACT

Real-Time Evaluation of Stimulation and Diversion in Horizontal Wells.

(December 2011)

Seyed Mohammad Tabatabaei Bafruei, B.S.; B.S., Sharif University of Technology;

M.S., University of Louisiana at Lafayette

Chair of Advisory Committee: Dr. Ding Zhu

Optimum fluid placement is crucial for successful acid stimulation treatments of long horizontal wells where there is a broad variation of reservoir properties along the wellbore. Various methods have been developed and applied in the field to determine acid placement and the effectiveness of diversion process, but determining the injection profile during a course of matrix acidizing still remains as a challenge. Recently distributed temperature sensing technology (DTS) has enabled us to observe dynamic temperature profiles along a horizontal wellbore during acid treatments. Quantitative interpretation of dynamic temperature data can provide us with an invaluable tool to assess the effectiveness of the treatment as well as optimize the treatment through on-the-fly modification of the treatment parameters such as volume, injection rate and diversion method.

In this study we first discuss how fluid placement can be quantified using dynamic temperature data. A mathematical model has been developed to simulate the temperature behavior along horizontal wellbores during and shortly after acid treatments. This model couples a wellbore and a near-wellbore thermal model considering the effect of both

mass and heat transfer between the wellbore and the formation. The model accounts for all significant thermal processes involved during a treatment, including heat of reaction, conduction, convection. Then a fast and reliable inversion procedure is used to interpret the acid distribution profiles from the measured temperature profiles.

We extend the real-time monitoring and evaluation of the acid stimulation treatment in horizontal wells to calculate the evolving skin factor as a function of time and location along the wellbore. As the skin factor is a reflection of the injectivity, it will indicate directly if the acid stimulation is effective and if diversion is successful. The approach to monitor the evolving skin along the lateral is to use a proper pressure transient model to calculate skin factor by integrating the inversion results of the temperature data (acid injection profile) with either surface or bottomhole injection pressure. This method can help engineers to optimize an acid stimulation in the field.

DEDICATION

This work is dedicated to

my beloved parents and my brothers.

ACKNOWLEDGEMENTS

I would like to express my sincere appreciation to my advisor and committee chair, Dr. Ding Zhu, for her continues support, guidance, encouragement and patience. Also, I would like to give special thanks to Dr. A. Daniel Hill for his advice and motivation during the course of this study. I enjoyed being their student and without their assistance and advice, this work would not have been accomplished.

I would also like to extend my appreciation to Dr. Christine Ehlig-Economides and Dr. Wayne M. Ahr for serving as my committee members and for their time and invaluable comments.

I would also like to take this opportunity to express my gratitude to my friends and colleagues and the department faculty and staff for making my time at Texas A&M University a great experience.

Last but not least, my special thanks go to my parents for their endless support, encouragement and love during my entire life.

NOMENCLATURE

A_w	wellbore cross sectional area, m^2 [L^2]
a	geothermal gradient, K/m [T/L]
B	formation volume factor, dimensionless
b	surface geothermal temperature, K [T]
C^0_{HCl}	acid concentration in weight fraction, dimensionless
C_p	heat capacity, J/(kg·K) [m/L-t^2-T]
$\mathbf{C}_n$	covariance matrix, dimensionless
c_t	total compressibility, Pa^{-1} [L-t^2/m]
d	vector of the observed data
E	energy, J [m^2/L-t^2]
e	residual vector
$f(\mathbf{x})$	objective function
$f_t(t)$	time function, dimensionless
g	forward model
G	sensitivity matrix
H	enthalpy, J/mol [m^2/L-t^2]
H	Hessian matrix
h	reservoir thickness, m [L]
I_{ani}	permeability anisotropy, dimensionless
J	Jacobian matrix
K	thermal conductivity, W/(m·K) [mL/t^3 -T]

k	reservoir permeability, m^2 [L^2]
$L_{1/2}$	half-length of the horizontal wellbore, m [L]
L	wellbore length, m [L]
M	number of parameters
M_R	molecular weight of carbonate rocks, kg/mol [m]
m	mass, kg [m]
N_{Ac}	acid capacity number, dimensionless
N	number of observed data
n	number of injection rate changes
n'	number of neighboring data points on either side of $y_s(i)$
n_{HCl}	number of moles of HCl consumed by reaction
p_e	reservoir pressure, Pa [m/L-t^2]
p_i	initial reservoir pressure, Pa [m/L-t^2]
p_w	wellbore pressure, Pa [m/L-t^2]
PV_{bt}	pore volume breakthrough, dimensionless
Q_{reac}	reaction heat released by consuming a unit mole of acid, J/(molHCl) [m^2/L-t^2]
q	injection rate, m^3/s [L^3/t]
q_n	injection rate during n^{th} time increment, m^3/s [L^3/t]
$q(t)$	injection rate at time t, m^3/s [L^3/t]
$q(x)$	volumetric flow rate inside the wellbore, m^3/s [L^3/t]
q_r	injection rate inside the formation per unit length of the wellbore, m^2/s [L^2/t]
$\dot{q}$	heat flux caused by heat conduction, W/m^2 [m/t^3]

R_i	reaction heat released in a unit volume of formation during a unit time, J/(m^3·s) [m^2/L^3-t^3]
r	radius, m [L]
r_b	radius affected by acid injection, m [L]
r_{wh}	wormhole penetration depth, m [L]
r_1	inside diameter of the casing or tubing, m [L]
s	skin factor, dimensionless
s_0	initial skin factor, dimensionless
$s(t)$	skin effect at time t, dimensionless
T	temperature, K [T]
T_0	surface temperature of injected fluid, K [t]
t	time, s [t]
t_{sup}	superposition time function, dimensionless
U	overall heat transfer coefficient between inside of tubing or casing and outside casing, J/(m^2·s·K) [m^2/ L^3-t^3-T]
V	volume of acid injected into the formation, m^3 [L^3]
$V_{R\text{-}dis}$	amount of rock that is dissolved during a unit time, m^3/s [L^3/t]
V^0_F	volumetric fraction of fast-reaction rock, dimensionless
W	the fluid mass injection rate, kg/s [m/t]
$\mathbf{x}$	parameters vector
y_s	smoothed value
z	vertical depth, m [L]
z_w	distance of the wellbore from the lower boundary, m [L]

Subscript

A	acid
accu	accumulation
bt	breakthrough
cal	calculated
dis	dissolved
e	reservoir
F	fast reaction
f	formation
H	horizontal
i	number of formation grid
in	input
m	number of wellbore grid
meau	measured
obs	observed
out	output
R	rock
r	radial direction
reac	reaction
s	smoothed
sim	simulated
sup	superposition
V	vertical

w	wellbore
wh	wormhole
x	x-direction

Superscript

n	number of time step

Greek

β_F	dissolving power of acid, dimensionless
ε	small residual, dimensionless
σ	standard deviation, dimensionless
η	wormhole efficiency, dimensionless
ρ	density, kg/m^3 [m/L^3]
μ	viscosity, kg/(s·m) [m/t-L]
ϕ	formation porosity, dimensionless
Δ	prefix for difference

TABLE OF CONTENTS

Page

LIST OF FIGURES

Page

Page

Page

Page

Page

LIST OF TABLES

Page

1. INTRODUCTION

1.1 Background

Matrix acidizing is a common stimulation technique applied to remove near-wellbore formation damage in both vertical and horizontal wells. It involves injecting acid solutions, usually hydrofluoric (HF) and/or hydrochloric (HCl) acids, into the formation to restore the original reservoir permeability through chemical reactions. In an acid treatment, optimum fluid placement is crucial, both for long horizontal wells where there is a broad variation of reservoir properties along the wellbore, and for vertical wells with multiple zones and/or extensive productive intervals. It is difficult to evaluate the placement of stimulation fluids and damage removal in real-time during the courses of matrix acidizing of a horizontal wells or a vertical wells with multiple zones. Pre-job matrix acidizing simulators can provide a theoretical prediction of the acid injection distribution and damage removal with prediction performance based on the limited information about the formation that is going to be treated. However, during the stimulation treatment unknown or unpredictable downhole events can have significant impacts on the results of the treatment.

When the treatment is completed, production logging tools and radioactive tracers sometimes are used to provide some feedback about the effectiveness of the treatment. However, well intervention during the treatment is required to obtain this data. Also, the

---

This dissertation follows the style of the *SPE Journal*.

data is not available until the treatment is finished, which does not allow for real-time treatment monitoring and optimization.

In order to achieve a successful matrix acidizing, it is important to monitor the treatment in real-time. Real-time monitoring of the matrix acidizing can provide us with an invaluable tool to assess the effectiveness of the treatment as well as to optimize the treatment on-the-fly. By monitoring the evolution of the skin factor during the treatment one can ensure that the acidizing treatment is removing the damage from the formation, a sufficient volume of acid is being injected into the formation, and more importantly, the injection is not causing damage to the formation, which can happen if the treatment is not well designed. The effect of the individual fluid stages pumped during the treatment can be evaluated. This information can be used for evaluating the effectiveness of diversion processes as well as optimizing future treatments.

1.2 Literature Review

Several methods for real-time evaluation of matrix acidizing in vertical wells were presented in the past and some of them were applied successfully in the field. These methods use the measurement of pressure (either surface pressure or bottomhole) and injection rate to calculate the evolution of skin factor during a treatment as the indicator for treatment effectiveness. To calculate the skin factor during the treatment, these methods either assume a steady-state flow is in effect in the region around the wellbore, or assume a transient flow regime and use a pressure transient solution to calculate the skin factor during the treatment.

McLeord and Coulter (1969) were the first to present a method for monitoring the acidizing treatment based on pressure transient analysis. Their method considers each stage of injection or shut-in during a treatment as a short individual well test. The skin factor during these test periods can be determined by applying the standard pressure transient analysis. This method must be considered as an approximate method since the analysis of pressure transient is valid only if the skin factor is constant during the test period. This is not the case when reactive fluids are injected into the formation. Hence, in order to apply the method it requires the injection of a slug of inert fluid each time an assessment of the damage removal is desired, which is usually impractical. In addition, this method provides an intermittent measurement of the skin factor during a treatment and not a continuous record as skin measurements are allowed only at discrete times during the course of the treatment.

Paccaloni (1979a,b and 1993) was the first to present a simple method for continuous calculation of the skin factor during the treatment using instantaneous pressure and injection rate. This method was based on steady-state Darcy flow in the region affected by acid injection. The skin factor in this method can be calculated as

$$p_w - p_e = \frac{141.2qB\mu}{kh}\left(\ln\frac{r_b}{r_w} + s\right) \quad \text{.....(1.1)}$$

where r_b is the radius affected by acid injection (Paccaloni suggests a value of 4 ft to be used). Assuming the reservoir properties are known, the bottomhole pressure corresponding to the prevailing injection rate can be predicted for any value of skin factor. Then the wellhead injection pressures can be derived from the bottomhole pressure by a calculation of hydrostatic head and friction pressure drop. If the wellhead pressure is plotted against the injection rate, the evolving skin factor can be read from the

graph as the treatment proceeds. In this method, the assumption of steady-state flow overestimates the skin factor because transient flow is in effect during treatments. Furthermore, abrupt changes in the injection rate can also be interpreted as changes in skin factor. This is not a serious problem because the error is relatively constant and the evolution of the skin factor is more important than its absolute value.

Prouvost and Economides (1987, 1989) introduced a technique that allows a continuous calculation of skin factor during an acid stimulation treatment. Their method simulates reservoir pressure response to the injection of fluids, using sequence of flow rates actually measured during the job execution. Each simulation is performed with a constant skin, s_0. At any time, the difference between the simulated pressure response, $p_{sim}(t,s_0)$ and the measured value, $p_{meas}(t)$ is interpreted as the difference between the actual skin value and the value which was used for the simulation, s_0. Since all other effects, which influence the pressure response are accounted for in the simulation, the difference between the simulated and the actual pressure response is attributed to the changing skin. Therefore,

$$s(t) = s_0 + \frac{kh}{141.2q(t)B\mu}\left[p_{meas}(t) - p_{sim}(t, s_0)\right] \quad \text{.....(1.2)}$$

where $s(t)$ and $q(t)$ are the skin effect and the injection rate at time t, respectively. In this method the simulation of the pressure response requires good knowledge of the reservoir and the initial value of skin factor, which can be obtained from a pre-treatment pressure transient test.

This method is best suited to treatments in which the rate schedule is known a priori, so that the simulation can be done before the treatment. However, with a suitably fast simulator, this technique can presumably be applied as a real-time monitoring method,

even when the rate schedule is not known before the treatment or is changed during the course of the treatment.

In spite of Paccaloni's method which does not consider the effect of diverting agents on the pressure response, Prouvost and Economides accounted for the effect of diverting agents by subtracting the increased pressure attributed to the diverting agent pressure drop from the bottomhole pressure. For this method to be valid, diverting agents must be injected in a batch of a fluid that does not affect the damage skin factor.

In 1994, Behenna applied Prouvost and Economides' method to calculate the evolving skin factor during the course of matrix acidizing. He considered the effect of the diverting agent by subtracting the diverting agent pressure drop from the bottomhole pressure used in the skin calculation. In addition, he suggested that the examination of the rate of change of skin factor with respect to time can provide more information on the rate of skin factor decrease or increase. This information may help indicate depth and severity of formation damage or the efficiency of diverting agent slugs used during the treatment. However, derivative plot requires smoothing to eliminate the effect of noisy data.

Montgomery et al. (1995) implemented Prouvost and Economides' technique into a computer program for real-time monitoring of the matrix acidizing. To obtain the estimate of reservoir properties and initial skin factor required in this method, they suggest using a pretreatment injectivity test in which an inert fluid is injected at several different rates. Then they analyzed the rate-pressure response of the injectivity test assuming steady-state flow, as in Paccaloni's method.

In 1996, Hill and Zhu presented the inverse injectivity versus superposition time function plot for monitoring the evolving skin factor during a matrix acidizing treatment. Their method was originally based on the concept of well test analysis. They adopted the theory from a standard injectivity test by use of the approximate line source solution for transient flow during the injection. They showed that the pressure transient response to injection for multiple injection rates can be written as

$$\frac{p_i - p_w}{q_n} = m\Delta t_{\sup} + b \quad \text{.....(1.3)}$$

where m and b are function of reservoir and fluid properties and skin factor and Δt_{sup} is the superposition time function. According to this equation, a plot of inverse injectivity versus the superposition time function yields a straight line with a slope of m and an intercept of b. As they discussed, during the treatment, the parameters defining the slope, m, do not change. Among the parameters defining the intercept, b, the only one that changes as acid is injected is the skin factor. As a result, each inverse injectivity/superposition time point lies on a straight line having a slope, m, with its intercept depending on the skin factor at that moment. Thus, a family of constant skin curves can be calculated and plotted on a diagnostic chart of inverse injectivity vs. superposition time function before the treatment, and the skin change can be monitored by locating the inverse injectivity as a function of superposition time on the chart.

This method can be used to evaluate the effectiveness of both stimulation and diversion. During an effective acidizing treatment, skin factor decreases, which causes the inverse injectivity to also decrease. However, diverting agents cause an increase in the apparent skin factor and hence cause the inverse injectivity to increase.

This method has been widely used in the field and successful field applications in both oil and gas wells (da Motta et al., 1997 and Zhu et al., 1998) have shown the substantial value of real-time monitoring in well stimulation.

Following the same approach as the inverse injectivity method, Zhu et al. (2000) developed a technique for real-time monitoring of acidizing treatment in horizontal wells. In this method, evolution of the overall skin factor during a matrix acidizing is calculated explicitly from pressure and flow rate data using a proper pressure transient model for horizontal wells. However, matrix acidizing is significantly different in horizontal wells compared to vertical wells. To evaluate matrix acidizing in vertical wells, it is assumed that the variation in reservoir properties is not significant along the treatment interval, therefore, the near-wellbore formation damage distribution and also acid distribution during the treatment can be assumed to be uniform. However this is not common in matrix acidizing of horizontal wells. The near-wellbore formation damage distribution and the acid distribution along the horizontal wellbore are both affected by a longer wellbore length and a broader variation in the reservoir properties along the wellbore. This causes a non-uniform skin effect and acid injection distribution in matrix acidizing of horizontal wells. Hence, for more accurate evaluation of the matrix acidizing treatment and effectiveness of the diversion process in horizontal wells, it is highly desired to monitor the evolution of skin factor along the lateral instead of only monitoring the overall skin factor.

To achieve this goal it is first required to determine the acid distribution along the wellbore during the course of matrix acidizing. Recently, there have been several studies to address this issue by using distributed temperature sensing technology (DTS). This

technology enables us to observe a dynamic temperature profile along the wellbore during treatments as opposed to conventional temperature logs which can only provide us with a snapshot of the temperature profile during a shut-in period. DTS technology uses a fiber-optic cable assembly that can be deployed in several configurations in the wellbore, and more importantly, across the perforated intervals. DTS systems generally do not interfere with flow and can be used for short-term as well as permanent monitoring. This technology has been successfully applied in the field for the flow profiling purpose (Johnson et al., 2006; Yoshika et al., 2007a,b; Wang et al., 2008 and Li and Zhu, 2010) but its application for monitoring stimulation treatment is mainly limited to qualitative interpretation of DTS data.

In 2006, Clanton et al. presented a successful case history of the DTS application for real-time downhole monitoring of multi-stage acid stimulation treatments performed on vertical wells that contain multiple non-isolated pay intervals. They indicated that the collected temperature profiles across the multiple pay intervals yielded valuable information for identifying the zones that acid penetrates and also the effectiveness of diversion methods.

Glasbergen et al. (2009a) described the qualitative and quantitative interpretation of DTS data during the course of matrix acidizing in vertical wells. They indicated that a qualitative evaluation of a continuous wellbore temperature profile can provide a visual assessment of fluid placement, diversion effect and the existence of crossflow of fluids between zones within the wellbore. For quantification of the flow distribution during a treatment, they first analyzed the effect of flow distribution on the temperature profile and used the results of this analysis to try to quantify the flow distribution from the

measured temperature profile by solving the inverse problem. They discussed the difficulty regarding solving the inverse problem in real-time and suggested that different techniques are required to get to quantification of the flow distribution. For the cases that temperature profile shows a specific characteristic, they introduced a type curve method to ease the solution of inverse problem in real-time. For the cases that inversion of temperature data leads to a non-unique solution, they introduced the tracer slug concept to determine the flow distribution during the treatment. The concept consists of making a sequence of temperature disturbances intentionally using a small volume of fluid with a different temperature signature compared to the majority of fluids being injected and then tracing the leading and trailing edge of the slug at different times and determining the fluid velocity profile along the perforations. Then the velocity profile can easily be converted to a flow rate profile inside the wellbore. The tracer slug concept offers a fast and simple method to determine the acid injection distribution, however, there are a few limitations associated with this method which hinders its application in some cases. The method requires change in the operation and a sequence of temperature disturbances needs to be created repeatedly from the beginning to the end of the treatment. The tracer can lose its signature with time due to convection and conduction with the surroundings.

Later Glasbergen et al. (2007 and 2009b) presented and discussed several case histories where DTS was applied to evaluate the effectiveness of the diversion methods using the tracer slug concept in vertical wells. They confirmed that the tracer slug method is not applicable for every treatment. They developed a candidate selection criterion by defining a dimensionless DTS number, N_{DTS} as

$$N_{DTS} = \frac{ID^2 h}{17.1582\ T_{DTS}\ Q_{BH}} \quad \text{.....(1.4)}$$

In this equation, *ID* is the inner diameter of the completion in inch, h is the total measured length of the completion in feet, T_{DTS} is the data acquisition time in second between two consecutive DTS profiles and Q_{BH} is the bottomhole rate in bbl/min. The DTS number is in fact a measure of the number of times an anomaly would be shown in the completed interval in case the flow rate is constant to the bottom of the completion.

1.3 Objective

The objective of this study is to develop a comprehensive method for real-time monitoring of matrix acidizing in horizontal wells. The goal is to evaluate the treatment in real-time by calculating the evolving skin factor as a function of injection time and location along the wellbore. As the skin factor is a reflection of the injectivity, it will indicate directly if the acid stimulation is effective and if diversion is successful.

Since the skin effect and the acid injection distribution along the horizontal wellbore is not uniform, to calculate the evolution of the skin factor along the lateral, it is first necessary to determine the injection profile during the course of matrix acidizing. In this study we address this issue by applying the distributed temperature sensing technology.

To analyze the continuous temperature data, we will first develop a mathematical model to simulate the temperature behavior during the matrix acidizing and to understand the effect of some parameters such as the distribution of stimulation fluid along the lateral and the effectiveness of the diversion processes on the transient temperature response. This model can be developed by coupling a wellbore and a near-wellbore thermal model considering the effects of both mass and heat transfer between the wellbore and the

formation. The model will account for all the significant thermal processes involved during a treatment, including heat of reaction, conduction and convection.

Then an inversion procedure needs to be applied to interpret the acid distribution profile from the measured temperature data. Since the inverse problem in this case needs to be solved in real-time, a gradient-based inversion method can be a good candidate, however, the highly non-linear nature of this problem may cause this method to be inefficient. Therefore, to determine an appropriate inversion procedure for this case, it is intended to evaluate both gradient-based and stochastic inversion methods. In general, gradient-based methods are fast, but they may result in local minimums. Stochastic methods can avoid the local minimum problem because they can search the global parameter space, however, when the parameter number is large, computation becomes extremely expensive, which hinders its application in some cases.

After solving the inverse problem and determining the acid injection distribution during the treatment, we can then use a proper pressure transient model to calculate the evolving skin factor along the lateral using the surface or bottomhole pressure and the inversion results from the temperature data.

2. FORWARD MODEL DEVELOPMENT

2.1 Introduction

In this section, a forward model is developed to simulate temperature behavior during acid stimulation treatment in horizontal wells. This model couples a wellbore and a near-wellbore thermal model considering the effects of both mass and heat transfer between the wellbore and the formation. The models account for all significant thermal processes involved during a treatment, including heat of reaction, conduction and convection.

Figure 2.1 shows the heat transfer process during acid injection over a segment of a horizontal well. This includes heat of convection along the wellbore caused by injection flux, heat convection from the wellbore into the formation caused by communication between permeable formation and wellbore, heat conduction due to the temperature difference between injected fluid and formation geothermal temperature, and heat generated by chemical reaction between injected acid and formation rock. As illustrated in this figure, during an acid stimulation treatment, convection is the primary heat transfer mechanism inside the wellbore. Near-wellbore conditions also affect the wellbore temperature behavior by controlling the heat conducted to the wellbore. Near-wellbore region can be divided into communicating and non-communicating sections. During treatment, there is no convection over the non-communicating sections, therefore, conduction is the only thermal process affecting the near-wellbore temperature response. However, along the communicating sections or where stimulation fluid exits the wellbore, convection, conduction and heat of reaction come into play and affect the near-wellbore temperature response.

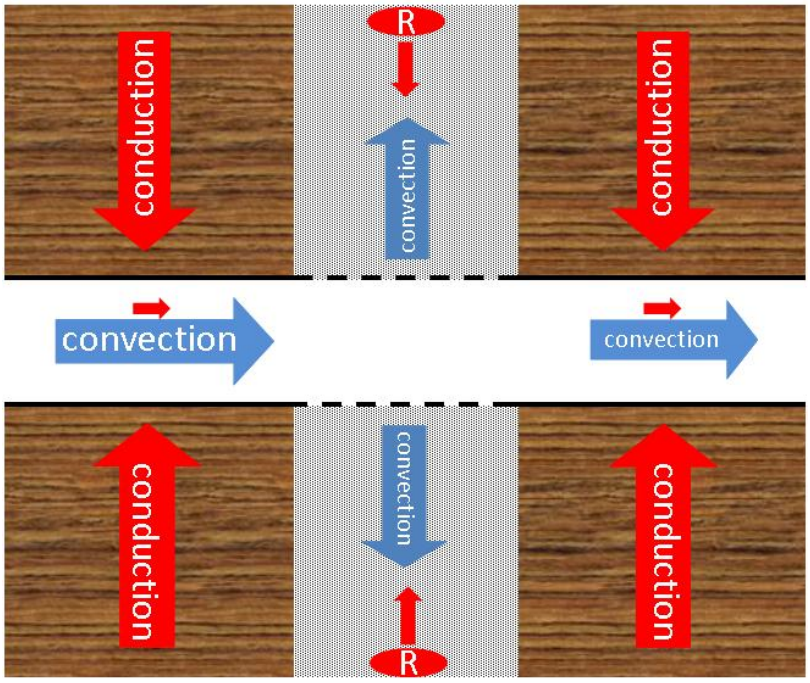

Fig. 2.1—Illustration of thermal processes involved during matrix acidizing of a horizontal well.

In this study, the wellbore model is used to solve the temperature profile along the wellbore where we measure the temperature by DTS. The model includes the effects of convection and conduction in the wellbore and conduction from the formation.

The near-wellbore model is used to simulate the transient temperature response in the formation during a treatment. The model includes the effects of convection and conduction in the near-wellbore region and also heat generated by the reaction between acid and rocks.

The wellbore and near-wellbore model equations are discretized and solved numerically using finite difference method. Since the conduction term in the wellbore model is defined by the near-wellbore model, these two models are coupled and solved simultaneously by applying appropriate initial and boundary conditions.

2.2 Near-Wellbore Thermal Model

2.2.1 Communicating Sections

Communicating sections are defined as those parts of the lateral that fluid exits the wellbore and flow into the formation. They can be perforated zones or pre-perforated sections of a slotted linear. In openhole completion the entire lateral can be considered as a communicating section.

Assuming radial flow of an incompressible fluid in the near wellbore region, the near-wellbore thermal model for communicating sections can be derived by considering conduction and convection in the near-wellbore region. For the convection term, the flux is dominated by wormhole propagation; therefore, a wormhole growth model is required as well. In addition to heat transfer caused by flow, we need to account for the reaction between acid and carbonate rocks which generates heat and results in a temperature increase. To simplify the problem, it is reasonable to assume that reaction occurs primarily at the tip of the wormholes.

Figure 2.2 illustrates the physical system of acid injection into the formation (Tan et al., 2009). Wormholes are directly developed from the wellbore. At the front of this wormhole region, there is a small reaction region defined by the newly created wormhole during a unit time. Besides the wormhole and the reaction regions, there are also the spent acid region and the formation region. In the spent acid region, the fluid is water containing reaction products, calcium chloride and CO_2. The formation region has not been touched by acid and is filled with original formation fluid.

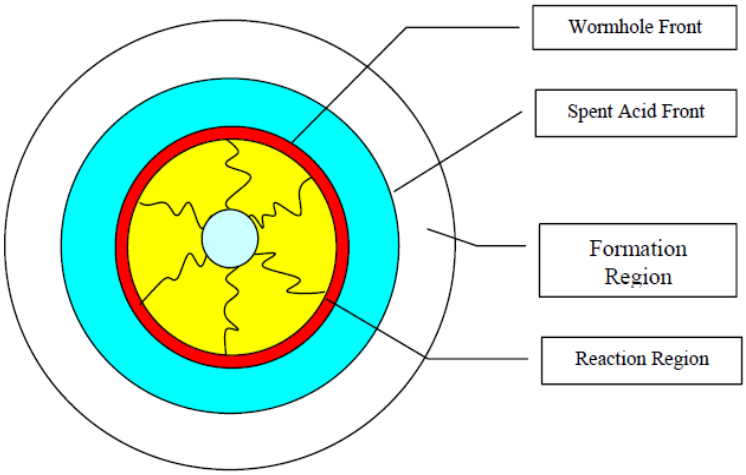

Fig. 2.2—Physical system assumed to develop the near-wellbore thermal model.

To formulate the near-wellbore model, we apply the energy balance over a control volume in the near wellbore region (**Fig. 2.3**) as follows:

$$E_{in} - E_{out} + E_{reaction} = E_{accu} \quad \text{.....(2.1)}$$

where E_{in} is the energy flows into the control volume, E_{out} is the energy flows out of the control volume, $E_{reaction}$ is the energy generated by reaction between acid and rock, and E_{accu} is the energy accumulation in the control volume.

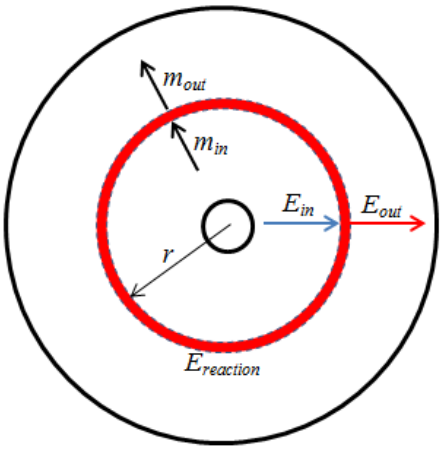

Fig. 2.3—Energy and mass transfer over a control volume of the near-wellbore region.

The energy flows into or out of the control volume are controlled by both convection and conduction. They can be expressed as

$$E_{in} = \rho_A C_{pA} q_r T_f(r)\Delta x\Delta t + \dot{q}(r) \times 2\pi r\Delta x\Delta t \quad \text{.....(2.2)}$$

$$E_{out} = \rho_A C_{pA} q_r T_f(r+\Delta r)\Delta x\Delta t + \dot{q}(r+\Delta r) \times 2\pi (r+\Delta r)\Delta x\Delta t \quad \text{.....(2.3)}$$

where $T_f(r)$ is the formation temperature, ρ_A and C_{pA} are the density and the heat capacity of the acid solution, respectively. Δt is the injection time, r is the radius, q_r is the injection rate inside the formation per unit length of the wellbore and $\dot{q}$ is the heat flux caused by heat conduction.

The energy created by reaction is

$$E_{reaction} = R_i \times 2\pi r\Delta r\Delta x\Delta t \quad \text{.....(2.4)}$$

where R_i is the heat of reaction released in a unit volume of formation during a unit time.

The energy accumulation in the control volume can be written as

$$\begin{aligned} E_{accu} &= 2\pi r\Delta x\Delta r\phi\left(\rho_A C_{pA} T_f(r)\Big|_{t+\Delta t} - \rho_A C_{pA} T_f(r)\Big|_t\right) \\ &+ 2\pi r\Delta x\Delta r(1-\phi)\left(\rho_R C_{pR} T_f(r)\Big|_{t+\Delta t} - \rho_R C_{pR} T_f(r)\Big|_t\right) \end{aligned} \quad \text{.....(2.5)}$$

where ρ_R and C_{pR} are the density and the heat capacity of the rock, respectively and ϕ is the formation porosity.

Substituting Eqs. 2.2 through 2.4 into Eq. 2.1, we have

$$\begin{aligned} &\rho_A C_{pA} q_r \frac{\left[T_f(r) - T_f(r+\Delta r)\right]}{\Delta r} + 2\pi \frac{\left[r\dot{q}(r) - (r+\Delta r)\dot{q}(r+\Delta r)\right]}{\Delta r} + R_i \times 2\pi r \\ &= 2\pi r\phi \frac{\left(\rho_A C_{pA} T_f(r)\Big|_{t+\Delta t} - \rho_A C_{pA} T_f(r)\Big|_t\right)}{\Delta t} + \\ &2\pi r(1-\phi)\frac{\left(\rho_R C_{pR} T_f(r)\Big|_{t+\Delta t} - \rho_R C_{pR} T_f(r)\Big|_t\right)}{\Delta t} \end{aligned} \quad \text{.....(2.6)}$$

Taking limits as $\Delta t \to 0$ and $\Delta r \to 0$, the energy balance equation can be written as

$$-\rho_A C_{pA} q_r \frac{\partial T_f(r)}{\partial r} + 2\pi\left(\frac{\partial[r\dot{q}(r)]}{\partial r}\right) + R_i \times 2\pi r = 2\pi r\phi\rho_A C_{pA} \frac{\partial T_f(r)}{\partial t} + 2\pi r(1-\phi)\rho_R C_{pR} \frac{\partial T_f(r)}{\partial t} \quad \text{.....(2.7)}$$

The heat flux caused by radial heat conduction in the formation ($\dot{q}$) can be expressed as

$$\dot{q}(r) = -K_f \frac{\partial T_f(r)}{\partial r} \quad \text{.....(2.8)}$$

where K_f is the thermal conductivity of the formation.

By substituting Eq. 2.8 into Eq. 2.7, the final form of the near-wellbore thermal model can be expressed as

$$\frac{\rho_A C_{pA}}{2\pi} q_r \frac{1}{r}\frac{\partial T_f(r)}{\partial r} - \frac{K_f}{r}\left(\frac{\partial T_f(r)}{\partial r} + r\frac{\partial^2 T_f(r)}{\partial r^2}\right) - R_i + \left[\phi\rho_A C_{pA} + (1-\phi)\rho_R C_{pR}\right]\frac{\partial T_f(r)}{\partial t} = 0 \quad \text{.....(2.9)}$$

In this equation, the first term accounts for heat convection, the second term accounts for the heat conducted in the acid solution and the rock, and the third term is the reaction heat and the last denotes the energy change in the control volume of the formation.

To solve the energy balance equation, the heat of reaction, R_i, that is shown as a source term in the equation, needs to be determined first. By definition, R_i is the heat of reaction released in a unit volume of formation during a unit time and it can be expressed as

$$R_i = \frac{Q_{reac} n_{HCl}}{2\pi r \Delta r \Delta t} \quad \text{.....(2.10)}$$

where Q_{reac} is the reaction heat released by consuming a unit mole of acid and n_{HCl} is the number of moles of HCl consumed by reaction which can be determined by

$$n_{HCl} = \frac{2V_{R-dis}\rho_R}{M_R} \quad \text{.....(2.11)}$$

where M_R is the molecular weight of carbonate rocks (limestone or dolomite) and $V_{R\text{-}dis}$ is the amount of rock that is dissolved during a unit time. $V_{R\text{-}dis}$ can be calculated as

$$V_{R-dis} = \eta\pi\left[r_{wh}^2(t+\Delta t) - r_{wh}^2(t)\right](1-\phi) \quad \text{.....(2.12)}$$

where r_{wh} is the wormhole penetration depth and η is the wormhole efficiency defined as the volumetric fraction of the rock dissolved in the region penetrated by acid. Economides et al. (1993) suggests that the wormhole efficiency can be estimated from linear core flood data as being

$$\eta = N_{Ac} PV_{bt} \quad \text{.....(2.13)}$$

where PV_{bt} is the number of pore volume of acid injected at the time of wormhole breakthrough at the end of the core. This approach is equivalent to assuming that a fixed number of pore volume of acid is needed to propagate wormholes to a given distance. N_{Ac} in the above equations is the acid capacity number, defined as the ratio of amount of mineral dissolved by the acid in the pore space of a unit volume of rock to the amount of mineral present in the unit volume of rock. N_{Ac} can be calculated as follow.

$$N_{Ac} = \frac{\phi\beta_F C^0_{HCl}\rho_A}{(1-\phi)V^0_F\rho_R} \quad \text{.....(2.14)}$$

where β_F is the dissolving power of 100% HCl, C^0_{HCl} is acid concentration in weight fraction and V^0_F is the volumetric fraction of fast-reaction rock.

Eq. 2.12 suggests that to determine $V_{R\text{-}dis}$ we need to apply a wormhole model to be able to track the wormhole growth. In addition, a wormhole model is required to track the wormhole penetration into the formation because wormhole propagation dominates the acid flow. The temperature profile in the formation during treatment is directly related to

the flow field. In this study, we have applied the volumetric model presented by Economides et al. (1993) to simulate the wormhole growth. r_{wh} can be expressed as

$$r_{wh} = \sqrt{r_w^2 + \frac{N_{Ac} V}{\eta \pi \phi h}} \quad \text{.....(2.15)}$$

where V is the volume of acid injected into the formation.

Substituting the definition of wormhole efficiency into the above equation gives

$$r_{wh} = \sqrt{r_w^2 + \frac{V}{PV_{bt} \pi \phi h}} \quad \text{.....(2.16)}$$

Then by substituting Eq. 2.16 into Eq. 2.12 and rearranging, we have

$$V_{R-dis} = \frac{\eta q_r \Delta t}{PV_{bt} \phi}(1-\phi) \quad \text{.....(2.17)}$$

Substituting Eq. 2.17 into Eq. 2.11, yields

$$n_{HCl} = \frac{2\eta \rho_R q_r \Delta t}{M_R PV_{bt} \phi}(1-\phi) \quad \text{.....(2.18)}$$

And finally the heat of reaction can be determined by

$$R_i = \frac{\eta Q_{reac} \rho_R q_r}{\pi r \Delta r M_R PV_{bt} \phi}(1-\phi) \quad \text{.....(2.19)}$$

The reaction heat released by consuming a unit mole of acid, Q_{reac}, is controlled by the acid type and the minerals present in the formation. The detailed calculation of Q_{reac} is discussed later in Section 3.

2.2.2 Non-Communicating Sections

Non-communicating sections are those parts of the lateral that fluid does not exit the wellbore. They can be non-perforated sections on a slotted linear or a base pipe.

During treatment, the only thermal process involved in theses sections is heat conduction and there is no convection and reaction effects associated with these sections (see Fig. 2.1). Therefore, we can drop the convention and reaction terms in the energy balance equation for communicating sections (Eq. 2.9). Consequently, the near-wellbore thermal model for non-communicating sections can be expressed as

$$-\frac{K_f}{r}\left(\frac{\partial T_f(r)}{\partial r}+r\frac{\partial^2 T_f(r)}{\partial r^2}\right)+\left[\phi\rho_A C_{pA}+(1-\phi)\rho_R C_{pR}\right]\frac{\partial T_f(r)}{\partial t}=0 \quad \text{.....(2.20)}$$

2.3 Wellbore Thermal Model

The wellbore model is used to solve the temperature profile along the wellbore where we measure the temperature by DTS. The model considers the convection of heat because of injection, the conduction of heat in the wellbore, and the conduction of heat because of the temperature difference between the wellbore fluid and the formation (see Fig. 2.1).

To develop this model, we can apply the energy and mass balance over a control volume of the wellbore assuming 1D flow of a single-phase, incompressible fluid as shown in **Fig. 2.4**.

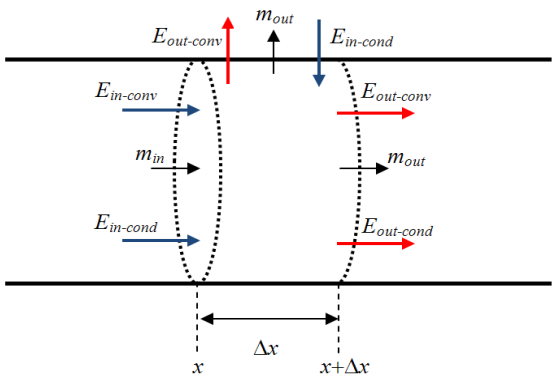

Fig. 2.4—Energy and mass transfer over a control volume of the wellbore.

The energy and mass balance over the control volume can be written as

$$E_{in} - E_{out} = E_{accu} \quad \text{.....(2.21)}$$

$$mass_{in} = mass_{out} \quad \text{.....(2.22)}$$

As we can see in Fig. 2.4, both convection and conduction affect the energy flows into or out of the control volume. Accounting for both of these heat transfer mechanisms the E_{in} and E_{out} can be defined as

$$E_{in} = \rho_A C_{pA} q(x) T_w(x) \Delta t + \dot{q}_r \times 2\pi r \Delta x \Delta t + \dot{q}_x \times \pi r^2 \Delta t \quad \text{.....(2.23)}$$

$$E_{out} = \rho_A C_{pA} q(x+\Delta x) T_w(x+\Delta x) \Delta t + \rho_A C_{pA} q_r T_w(x) \Delta x \Delta t - \dot{q}_{x+\Delta x} \times \pi r^2 \Delta t \quad \text{.....(2.24)}$$

where $T_w(x)$ is the temperature of the fluid in the wellbore at distance x from the heel, $q(x)$ is the volumetric flow rate inside the wellbore, q_r is the injection rate into the formation per unit length of the wellbore, $\dot{q}_x$ and $\dot{q}_r$ are the heat fluxes caused by heat conduction inside the wellbore and from the formation, respectively. $\dot{q}_x$ and $\dot{q}_r$ can be defined by the following equations.

$$\dot{q}_x = K_A \left. \frac{\partial T_w}{\partial x} \right|_x \quad \text{.....(2.25)}$$

$$\dot{q}_r = K_f \left. \frac{\partial T_f}{\partial r} \right|_{r=r_w} \quad \text{.....(2.26)}$$

where K_A and K_f is the thermal conductivity of the acid solution and formation, respectively. Since the thermal conductivity of the acid solution is small and also temperature difference inside the wellbore is very small the heat conduction inside the wellbore is very insignificant.

The energy accumulation in the control volume can be written as

$$E_{accu} = \rho_A C_{pA} A_w T_w(x)\Delta x\Big|_{t+\Delta t} - \rho_A C_{pA} A_w T_w(x)\Delta x\Big|_t \quad \text{.....(2.27)}$$

where A_w is the wellbore cross sectional area.

Substituting Eqs. 23 through 27 into Eq. 2.21, and rearranging the equation, we have

$$\begin{aligned} &\rho_A C_{pA} \frac{[q(x)T_w(x) - q(x+\Delta x)T_w(x+\Delta x)]}{\Delta x} + 2\pi r K_f \left.\frac{\partial T_f}{\partial r}\right|_{r=r_w} \\ &- \rho_A C_{pA} q_r T_w(x) + \pi r^2 K_A \frac{\left(\left.\frac{\partial T_w}{\partial x}\right|_{x=x+\Delta x} - \left.\frac{\partial T_w}{\partial x}\right|_{x=x}\right)}{\Delta x} \quad \text{.....(2.28)} \\ &= \frac{\rho_A C_{pA} A_w T_w(x)\Delta t\Big|_{t+\Delta t} - \rho_A C_{pA} A_w T_w(x)\Delta t\Big|_t}{\Delta t} \end{aligned}$$

Then from the mass balance (Eq. 2.22), we have

$$q(x)\Delta t = q(x+\Delta x)\Delta t + q_r \Delta x \Delta t \quad \text{.....(2.29)}$$

Assuming Δx is very small, yields

$$\frac{\partial q(x)}{\partial x} = -q_r \quad \text{.....(2.30)}$$

Substituting q_r into Eq. 2.28, and taking limits as $\Delta t \to 0$ and $\Delta x \to 0$, we have

$$\begin{aligned} &- \rho_A C_{pA} \frac{\partial[q(x)T_w(x)]}{\partial x} + 2\pi r K_f \left.\frac{\partial T_f}{\partial r}\right|_{r=r_w} - \rho_A C_{pA}\left(-\frac{\partial q(x)}{\partial x}\right)T_w(x) + \pi r^2 K_A \frac{\partial^2 T_w}{\partial x^2} \quad \text{.....(2.31)} \\ &= \rho_A C_{p_A} A_w \frac{\partial T_w}{\partial t} \end{aligned}$$

Finally with simplification, the wellbore thermal model can be expressed by the following equation.

$$\rho_A C_{pA} q(x) \frac{\partial T_w}{\partial x} - 2\pi r_w K_f \left.\frac{\partial T_f}{\partial r}\right|_{r=r_w} - \pi r_w^2 K_A \frac{\partial^2 T_w}{\partial x^2} + \pi \rho_A C_{pA} r_w^2 \frac{\partial T_w}{\partial t} = 0 \quad \text{.....(2.32)}$$

The first term in this equation represents the net effect of heat convection, the second term describe the effect of conduction from the formation which is defined by the near-wellbore thermal model (Eq. 2.9), and the third term describes the effect of conduction inside the wellbore which is negligible. The last term denotes the energy change in the control volume of the wellbore.

This model can be applied for both communicating and non-communicating sections of the wellbore. However, along the non-communicating sections, the volumetric flow rate inside the wellbore, $q(x)$, is constant; but along the communicating sections, $q(x)$ changes depending on the injection profile along that specific communicating section.

2.4 Forward Model Solution

Because the developed partial differential energy balance equations for wellbore and near-wellbore are extremely non-linear, we need to discretize these equations and solve them numerically. However, these two equations have to be solved simultaneously with appropriate initial and boundary conditions. This is because to solve the wellbore energy balance equation (Eq. 2.32) we must know the formation temperature gradient at the wellbore which is defined by the near-wellbore energy balance equation (Eq. 2.9). To solve the near-wellbore model we need to know the wellbore temperature which defines one of the boundary conditions for equation.

The solution of the coupled wellbore and near-wellbore model (known as forward model) simulates the transient temperature behavior in the wellbore during a treatment. The forward model can help us to understand the relationship between the temperature

behavior and thermal properties of acid and rock, wellbore configuration, surface injection rate and more importantly acid distribution.

2.4.1 Finite Difference Equation for the Near-Wellbore Model

To discretize the energy balance equations we use the finite difference method. We approximate the first derivative by backward differences and the second derivative by central differences. The discretized form of the near-wellbore energy balance equation can be expressed as

$$\frac{\rho_A C_{pA}}{2\pi}\frac{q_r}{r_i}\left(\frac{T^n_{f,i}-T^n_{f,i-1}}{\Delta r}\right)-\frac{K_f}{r_i}\left(\frac{T^n_{f,i}-T^n_{f,i-1}}{\Delta r}+r_i\frac{T^n_{f,i+1}-2T^n_{f,i}+T^n_{f,i-1}}{(\Delta r)^2}\right) \quad \text{.....(2.33)}$$
$$-R_i+\left[\phi\rho_A C_{pA}+(1-\phi)\rho_R C_{pR}\right]\frac{T^{n+1}_{f,i}-T^n_{f,i}}{\Delta t}=0$$

where $T^n_{f,i}$ is the temperature at i^{th} grid at n^{th} time step.

Rearranging this equation gives the solution of the temperature at grid i at $(n+1)^{th}$ time step as

$$T^{n+1}_{f,i}=T^n_{f,i}+\left(\frac{\Delta t}{\phi\rho_A C_{pA}+(1-\phi)\rho_R C_{pR}}\right)\left[-\frac{\rho_A C_{pA}}{2\pi}\frac{q_r}{r_i}\left(\frac{T^n_{f,i}-T^n_{f,i-1}}{\Delta r}\right)\right. \quad \text{.....(2.34)}$$
$$\left.+R_i+\frac{K_f}{r_i}\left(\frac{T^n_{f,i}-T^n_{f,i-1}}{\Delta r}+r_i\frac{T^n_{f,i+1}-2T^n_{f,i}+T^n_{f,i-1}}{(\Delta r)^2}\right)\right]$$

The following boundary conditions can be used to solve the above equation

$$T_f\Big|_{r=r_w}=T_w \quad \text{.....(2.35)}$$

$$T_f\Big|_{r=r_e}=T_e \quad \text{.....(2.36)}$$

where T_w is the wellbore temperature and T_e is the geothermal temperature.

Assuming the initial temperature everywhere in the formation is equal to the geothermal temperature, the initial condition can be written as

$$T_f\Big|_{t=0,r} = T_e \quad \text{.....(2.37)}$$

Solving the near-wellbore model numerically allows us to take into account the thermal effects of different completions. This can be done by adjusting the near-wellbore grid size and assigning different thermal properties to the grids to account for the effects of different materials in the near-wellbore region such as formation, liner, cement, etc.

2.4.2 Finite Difference Equation for the Wellbore Model

Using the same finite difference scheme as near-wellbore model, the discretized form of the wellbore energy balance equations is

$$\rho_A C_{pA} q_m \frac{T^n_{w,m} - T^n_{w,m-1}}{\Delta x} - 2\pi K_f r_w \frac{\partial T_f}{\partial r}\bigg|_{r=r_w,m} - \pi r_w^2 K_A \frac{T^n_{w,m+1} - 2T^n_{w,m} + T^n_{w,m-1}}{\Delta x^2} + \pi \varphi_A C_{pA} r_w^2 \frac{T^{n+1}_{w,m} - T^n_{w,m}}{\Delta t} = 0 \quad \text{.....(2.38)}$$

where $T^n_{w,m}$ is the temperature at m^{th} grid at n^{th} time step. And therefore, the temperature at grid m at $(n+1)^{th}$ time step can be solved by

$$T^{n+1}_{w,m} = T^n_{w,m} + \left(\frac{\Delta t}{\pi \varphi_A C_{pA} r_w^2}\right)\left[2\pi K_f r_w \frac{\partial T_f}{\partial r}\bigg|_{r=r_w,m} + \pi r_w^2 K_A \frac{T^n_{w,m+1} - 2T^n_{w,m} + T^n_{w,m-1}}{\Delta x^2} - \rho_A C_{pA} q_m \frac{T^n_{w,m} - T^n_{w,m-1}}{\Delta x}\right] \quad \text{.....(2.39)}$$

To solve this equation the following boundary condition can be used.

$$T_w\Big|_{x=0} = T_A \quad \text{.....(2.40)}$$

where T_A is the injected acid temperature at the heel.

Assuming the thermal equilibrium between wellbore and formation before acid injection, the initial temperature along the entire wellbore is equal to the formation temperature. Therefore, the initial condition for the above equation can be expressed as

$$T_w\big|_{t=0} = T_e \quad \text{.....(2.41)}$$

2.4.3 Coupling Procedure

To couple the wellbore and near-wellbore energy balance equations, a simple procedure is developed. This procedure assumes that the temperature along the entire wellbore is known at time step *n*, and we want to calculate the temperature along the wellbore for the next time step, *n*+1. Following describes this procedure:

1. Start with the first wellbore segment (*m*=1).
2. Assume a temperature for the segment, $T^{n+1}_{w,m\text{-}assumed}$.
3. Use the assumed temperature as the boundary condition for the near-wellbore energy balance equation and solve the discretized form of the near-wellbore energy balance equation (Eq. 2.34) to determine the formation temperature gradient at the wellbore which can be defined as

$$\left.\frac{\partial T_f}{\partial r}\right|_{r=r_w,m} = \frac{T^{n+1}_{f,1} - T^{n+1}_{f,0}}{\Delta r} \quad \text{.....(2.42)}$$

4. Use the calculated formation temperature gradient at the wellbore to solve the discretized wellbore energy balance equation (Eq. 2.39) and calculate the temperature at the segment number *m*, $T^{n+1}_{w,m\text{-}calculated}$.
5. Repeat steps 2 through 3 until the following criteria meets.

$$\frac{\left|T^{n+1}_{w,m-assumed} - T^{n+1}_{w,m-calculated}\right|}{T^{n+1}_{m-calculated}} < e \quad \text{.....(2.43)}$$

where *e* is a small residual which depending on the desired level of accuracy can be in the range of 0.001 to 0.01. Note that, the calculated temperature ($T^{n+1}_{w,m\text{-}calculated}$) can be used as a new guess for step 2.

6. Repeat steps 2 through 5, moving toward the toe of the lateral to calculate the temperature at each segment.

2.5 Forward Model Validation

In this section, we first discuss the validation of the near-wellbore and the wellbore model separately. Both models are simplified to be able to be solved analytically, and we compare the results with numerical solutions. We also address the validation of the coupled model by comparing the results of the numerical solution of the coupled model with Ramey's analytical solution of the wellbore temperature during injection.

2.5.1 Near-Wellbore Model Validation

The near-wellbore energy balance equation contains a source term due to the reaction and a second derivative term due to the conduction. Presence of these two terms in the model makes it to be very difficult to be solved analytically. If we ignore the conduction and reaction effects and only consider the convection effect in the near-wellbore region, then we can solve the model analytically. However, with this approach we are only able to validate the convection term in the near-wellbore model, but not the entire model. Following shows the model with only the convection term.

$$\frac{\rho_A C_{pA}}{2\pi} q_r \frac{1}{r} \frac{\partial T_f(r)}{\partial r} + \left[\phi \rho_A C_{pA} + (1-\phi)\rho_R C_{pR}\right] \frac{\partial T_f(r)}{\partial t} = 0 \quad \text{.....(2.44)}$$

This equation can be rearranged and expressed as

$$\frac{\partial T_f(r)}{\partial t} + f(r)\frac{\partial T_f(r)}{\partial r} = 0 \quad \text{.....(2.45)}$$

where

$$f(r) = \frac{\rho_A C_{pA} q_r}{2\pi\left[\phi\rho_A C_{pA} + (1-\phi)\rho_R C_{pR}\right]}\frac{1}{r} \quad \text{.....(2.46)}$$

Eq. 2.45 is a simple non-linear transport equation which describes the movement of the injected acid front in the formation. In this equation, $f(r)$ defines the acid front speed which is a function of radius, r. The further the acid gets, the slower the front moves.

Assuming the same boundary and initial conditions discussed in the previous section, following describes the solution of Eq. 2.45 by applying the method of characteristics.

It is first required to parameterize the boundary as

$$r_\Gamma(s) = \begin{cases} s \rightarrow s \geq 0 \\ 0 \rightarrow s < 0 \end{cases} \text{ and } t_\Gamma(s) = \begin{cases} 0 \rightarrow s \geq 0 \\ -s \rightarrow s < 0 \end{cases} \quad \text{.....(2.47)}$$

Then we can define $F(R)$ as

$$F(R) = \int_{r_w}^{R} \frac{1}{f(\xi)} d\xi \rightarrow \frac{\partial F(R)}{\partial R} = \frac{1}{f(R)} \quad \text{.....(2.48)}$$

Now the characteristics, $R(t,s)$, can be computed as

$$\begin{cases} \dfrac{\partial R(t,s)}{\partial t} = f(R(t,s)) \\ R(t_\Gamma(s), s) = r_\Gamma(s) \end{cases} \quad \text{.....(2.49)}$$

Therefore, we have

$$\frac{\partial R(t,s)}{\partial t}\frac{1}{f(R(t,s))} = 1 \longrightarrow \frac{\partial R(t,s)}{\partial t}\frac{\partial F(R(t,s))}{\partial R} = 1 \longrightarrow \frac{\partial F(R(t,s))}{\partial t} = 1 \quad \text{.....(2.50)}$$

Integrating over the time domain gives

$$\int_{t_\Gamma(s)}^{t} \frac{\partial F(R(\tau,s))}{\partial \tau} d\tau = t - t_\Gamma(s) \quad \text{.....(2.51)}$$

$$F(R(t,s)) - F(R(t_\Gamma(s),s)) = t - t_\Gamma(s) \longrightarrow F(R(t,s)) = F(r_\Gamma(s)) + t - t_\Gamma(s) \quad \text{.....(2.52)}$$

By change the variable as

$$\Phi(t,s) = T_f(R(t,s),t) \quad \text{.....(2.53)}$$

We have

$$\frac{\partial \Phi(t,s)}{\partial t} = \frac{\partial T_f(R(t,s),t)}{\partial t} + \frac{\partial R(t,s)}{\partial t}\frac{\partial T_f(R(t,s),t)}{\partial R} = 0 \quad \text{.....(2.54)}$$

Again integrating over the time domain results in

$$\int_{t_\Gamma(s)}^{t} \frac{\partial \Phi(\tau,s)}{\partial \tau} d\tau = 0 \quad \text{.....(2.55)}$$

$$\Phi(t,s) = \Phi(t_\Gamma(s),s) = T_f(R(t_\Gamma(s),s),t_\Gamma(s)) = T_f(r_\Gamma(s),t_\Gamma(s)) \quad \text{.....(2.56)}$$

Thus

$$T_f(R(t,s),t) = T_f(r_\Gamma(s),t_\Gamma(s)) \quad \text{.....(2.57)}$$

If $s < 0$, we have $\begin{cases} r_\Gamma(s) = 0 \\ t_\Gamma(s) = -s \end{cases}$ .....(2.58)

Considering the parameterization and boundary conditions, Eqs. 2.57 and 2.58 yield

$$T_f(R(t,s),t) = T_f(r_\Gamma(s),t_\Gamma(s)) = T_f(0,-s) = T_w \quad \text{.....(2.59)}$$

Therefore, we have

$$T_f(r,t) = T_w \text{ if } s < 0 \quad \text{.....(2.60)}$$

From Eq. 2.52 we can write

$$F(R(t,s)) = F(0) + t + s \quad \text{.....(2.61)}$$

As a result, we have

$$s = F(R(t,s)) - t \quad \text{.....(2.62)}$$

Substituting s from the above equation into Eq. 2.60, gives

$$T_f(r,t) = T_w \text{ if } F(r) < t \text{ or } \int_{r_w}^{r} \frac{1}{f(\xi)} d\xi < t \quad \text{.....(2.63)}$$

$$\text{If } s \geq 0 \text{, we have } \begin{cases} r_\Gamma(s) = s \\ t_\Gamma(s) = 0 \end{cases} \quad \text{.....(2.64)}$$

Considering the parameterization and initial condition, Eqs. 2.63 and 2.64 gives

$$T_f(R(t,s),t) = T\ (r_\Gamma(s), t_\Gamma(s)) = T\ (s,0) = T_e \quad \text{.....(2.65)}$$

Therefore, we can write

$$T_f(r,t) = T_e \text{ if } s \geq 0 \quad \text{.....(2.66)}$$

From Eq. 2.62, we have

$$T_f(r,t) = T_e \text{ if } \int_{r_w}^{r} \frac{1}{f(\xi)} d\xi > t \quad \text{.....(2.67)}$$

$\int_{r_w}^{r} \frac{1}{f(\xi)} d\xi > t$ can be computed considering the definition of $f(r)$, Eq. 2.46, and therefore, the solution of the near-wellbore energy balance equation with only convection term can be expressed as

$$\begin{cases} T_f(r,t) = T_w & \text{if} \quad \dfrac{\pi\left[\phi\rho_A C_{pA} + (1-\phi)\rho_R C_{pR}\right]\left(r^2 - r_w^2\right)}{\rho_A C_{pA} q_r} < t \\ T_f(r,t) = T_e & \text{if} \quad \dfrac{\pi\left[\phi\rho_A C_{pA} + (1-\phi)\rho_R C_{pR}\right]\left(r^2 - r_w^2\right)}{\rho_A C_{pA} q_r} > t \end{cases} \quad \text{.....(2.68)}$$

This analytical solution (Eq. 2.68) can be used to verify the numerical solution when we only consider the convection effect. A comparison between the results of analytical and numerical solution is presented in **Fig. 2.5**. In this case, it is assumed that the

wellbore temperature is constant during the injection at a value of 80 °F, and the formation temperature is assumed to be 170 °F. Injected rate is assumed to be 0.01 bbl/min per unit length of the wellbore, and remains constant during the injection. The other parameters used to simulate this case are summarizes in **Table 2.1**. As we can see in Fig. 2.5, the numerical solution is in a very good agreement with the analytical solution. Not only the numerical solution is able to simulate the position of the injected acid front accurately but also it is capturing the shape of the acid front (shock) precisely without introducing numerical dispersion error. This is important because the conduction effect on the temperature response is almost at the same level as the as numerical dispersion effect. To investigate the effect of numerical dispersion on the results, we set up different scenarios by changing the size of the grids and also including conduction in the numerical simulation.

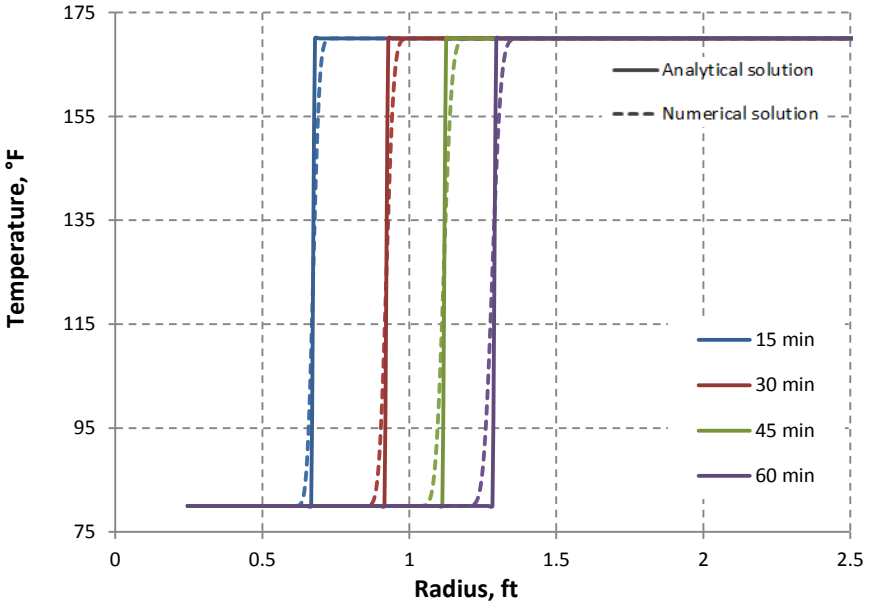

Fig. 2.5—Comparison of the analytical and numerical solutions for the near-wellbore temperature response (convection effect only).

TABLE 2.1—INPUT DATA USED TO VALIDATE THE NEAR-WELLBORE MODEL		
Heat capacity of rock (C_{pR})	1000	J/(kg·K)
Heat capacity of acid (C_{pA})	4187	J/(kg·K)
Density of rock (ρ_R)	2500	kg/m3
Density of acid (ρ_A)	1080	kg/m3
Thermal conductivity of formation (K_f)	3.6	W/(m·K)
Injected acid temperature (T_A)	300 (80)	K (ºF)
Reservoir temperature (T_e)	350 (170)	K (ºF)
Injection rate inside the formation (q_r)	0.0000869 (0.01)	m^2/sec (bbl/min/ft)
Wellbore radius (r_w)	0.076 (0.25)	m (ft)
Porosity (ϕ)	0.2	fraction

Figure 2.6 illustrates a comparison of numerical solutions for two different cases. In the first case, only convention effect is included and the formation is discretized with relatively coarse grids. In the second case, the conduction effect is included as well as the convection effect, and formation is discretized with very fine grids to minimize the numerical dispersion. We can observe that, both cases show a very similar temperature profiles at the acid front. This reveals that if we are not careful, numerical dispersion can be easily interpreted as conduction effect. In addition, error introduced by numerical dispersion can significantly affect the accuracy of simulating the convection effect. This fact is shown in **Fig. 2.7** more clearly. This figure shows the simulated temperature profiles in the formation for two different grid sizes. In this case, only convection is included in the model. As we can see when grids are coarse and therefore numerical dispersion presents, the position of the acid front is not captured properly. Thus, to be able to accurately simulate the effects of both conduction and conduction, it is necessary to minimize the numerical dispersion by constraining the grid size. Suggested grid size should be about 1 ft.

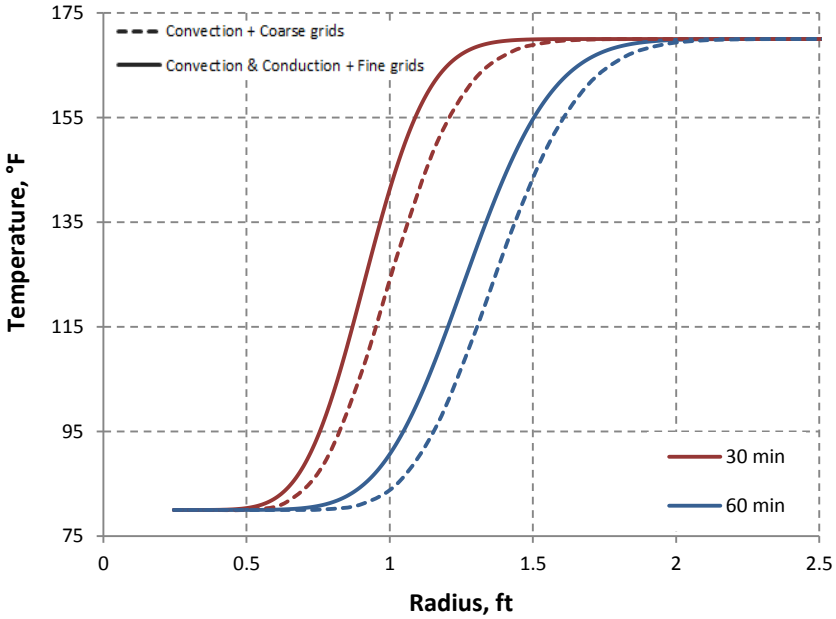

Fig. 2.6—Comparison of the conduction and numerical dispersion effects on the simulated near-wellbore temperature profile.

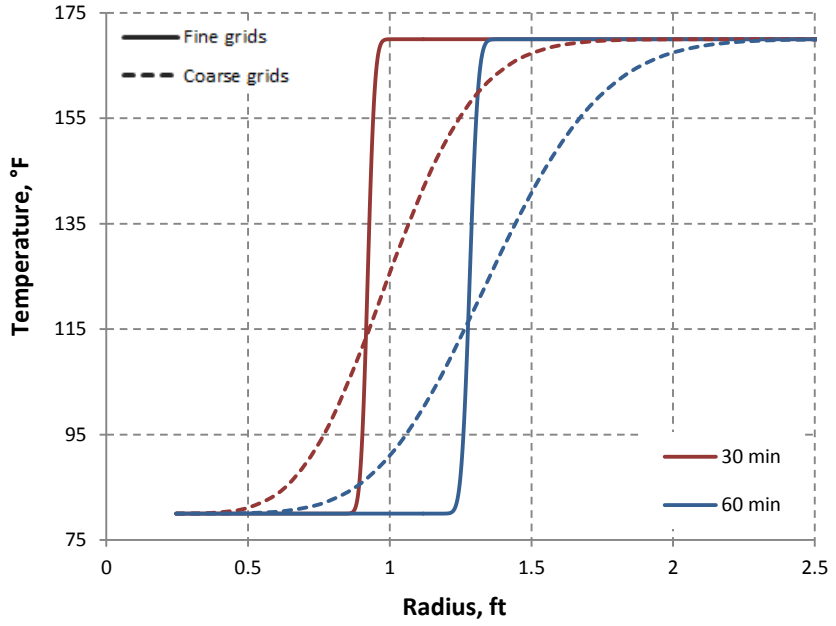

Fig. 2.7—Numerical dispersion effect on the simulated near-wellbore temperature profile.

2.5.2 Wellbore Model Validation

The same as near-wellbore model, there is no analytical solution available for the wellbore energy balance equation because this equation contains a conduction term that is defined by the near-wellbore model. Using the same approach as the near-wellbore model, we ignore the conduction effect from the formation. In addition, the conduction effect inside the wellbore can be ignored since it has an insignificant effect on the temperature behavior in the wellbore during injection. Thus the wellbore model can be reduced to the following form which only includes the convection term.

$$\rho_A C_{pA} q(x) \frac{\partial T_w}{\partial x} + \pi \rho_A C_{pA} r_w^2 \frac{\partial T_w}{\partial t} = 0 \quad \text{.....(2.69)}$$

Rearranging the above equation yields

$$\frac{\partial T_w}{\partial t} + f(x) \frac{\partial T_w}{\partial x} = 0 \quad \text{.....(2.70)}$$

where

$$f(x) = \frac{q(x)}{\pi r_w^2} \quad \text{.....(2.71)}$$

Similar to the near-wellbore model with only convection term included (Eq. 2.45), Eq. 2.70 is also a simple non-linear transport equation which describes the movement of acid front inside the wellbore with a velocity of $f(x)$. Eq. 2.71 suggests that the volumetric flow inside the wellbore defines the acid front movement. As acid enters the formation, flow rate inside the wellbore, and consequently fluid velocity decreases along the lateral. Eq. 2.70 is exactly in the same form as Eq. 2.45. Therefore, similar to the previous section and applying the method of characteristics with the boundary and initial

conditions discussed in the previous section, the solution of the wellbore energy balance equation with only convection term can be written as

$$\begin{cases} T_w(x,t) = T_e & \text{if} \quad \int_0^x \frac{1}{f(\xi)} d\xi > t \\ T_w(x,t) = T_A & \text{if} \quad \int_0^x \frac{1}{f(\xi)} d\xi < t \end{cases} \quad \text{.....(2.72)}$$

If we assume the acid injection distribution is uniform, $f(x)$ can be expressed as

$$f(x) = a\left(1 - \frac{x}{L}\right) \quad \text{.....(2.73)}$$

where

$$a = \frac{q_{inj}}{\pi r_w^2} \quad \text{.....(2.74)}$$

and L is the wellbore length.

Therefore, the solution of Eq. 2.69 assuming the uniform acid distribution is

$$\begin{cases} T_w(x,t) = T_A & \text{if} \quad x < (1 - e^{-\frac{a}{l}t})L \\ T_w(x,t) = T_e & \text{if} \quad x \geq (1 - e^{-\frac{a}{l}t})L \end{cases} \quad \text{.....(2.75)}$$

Now this analytical solution (Eq. 2.75) can be used to verify the convection effect in the wellbore model. **Fig. 2.8** illustrates a comparison between the results of numerical and analytical solutions for an openhole completion. We also assumed that the acid distribution is uniform along the entire wellbore. Injection rate is 10 bbl/min. Other parameters used in this example are shown in **Table 2.2**. We can see a very good agreement between the numerical solution and the analytical solution which verifies the accuracy of our numerical simulation.

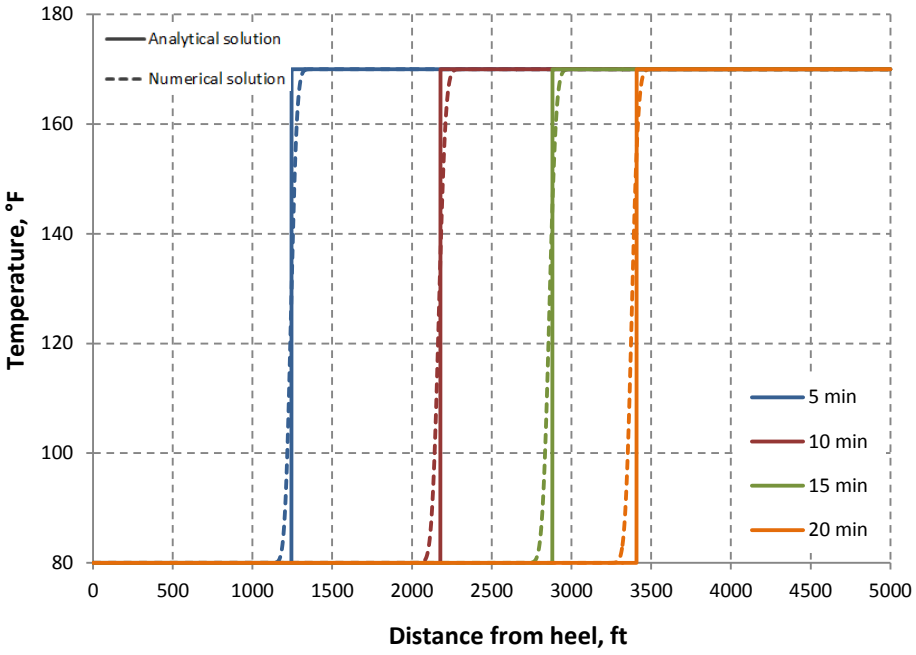

Fig. 2.8—Comparison of the analytical and numerical solutions for the wellbore temperature behavior (convection effect only).

TABLE 2.2—INPUT DATA USED TO VALIDATE THE WELLBORE MODEL		
Wellbore length (L)	5000	ft
Injected acid temperature (T_A)	80	°F
Reservoir temperature (T_e)	170	°F
Injection rate (q_{inj})	10	bbl/min
Wellbore radius (r_w)	0.25	ft

Note that, the same as simulating the temperature behavior in the formation, numerical dispersion can have a destructive impact on simulated wellbore temperature behavior. **Fig. 2.9** shows the simulated wellbore temperature profiles for the previous example for two different grid sizes. Again, it can be seen that, when grid size is relatively large the position and the shape of the acid front is not simulated accurately due to the error introduced by numerical dispersion. Therefore, it is necessary to optimize the size of the wellbore grids to minimize the numerical dispersion while computation time is acceptable.

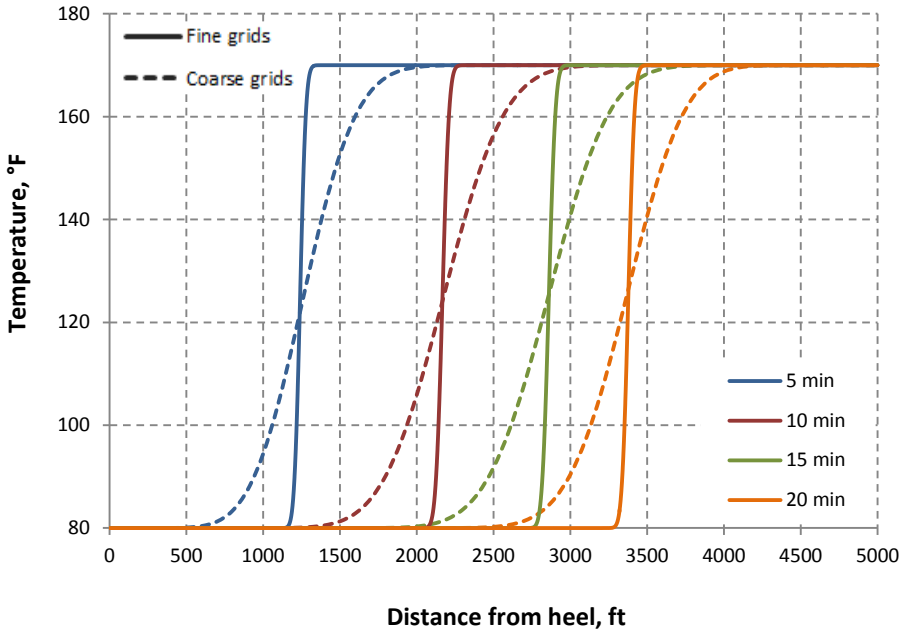

Fig. 2.9—Numerical dispersion effect on the wellbore temperature profile.

2.5.3 Coupled Model Validation

To validate the coupled model, we used the Ramey's analytical solution of the wellbore temperature during injection. Ramey's wellbore thermal model (Ramey, 1962) was developed for vertical wells for the case of flow in wellbore without inflow or outflow (non-communicating sections of the wellbore). His model assumes that heat transfer in the wellbore is steady-state, while heat transfer inside the formation is unsteady radial conduction. His model for flow of liquid in vertical wells is

$$T_w(z,t) = az + b - aA + (T_0 + aA - b)e^{-z/A} \quad \text{.....(2.76)}$$

where

$$A = \frac{WC_{pf}\left[K_f + r_1 U f_t(t)\right]}{2\pi r_1 U K_f} \quad \text{.....(2.77)}$$

and a is the geothermal gradient, b is the surface geothermal temperature, T_0 is the surface temperature of injected fluid, z is the vertical depth, W is the fluid mass injection rate, C_{pf} is the heat capacity of injected fluid, r_1 is the inside diameter of the casing or tubing and U is the overall heat transfer coefficient between inside of tubing or casing and outside casing. $f_t(t)$ in this equation is the time function and can be estimated from solutions for radial heat conduction from an infinitely long cylinder.

Assuming a constant geothermal temperature along horizontal wells, Eq. 2.76 can be modified by excluding the geothermal gradient term and be suitable for horizontal wells. Therefore, Ramey's model for flow of liquid in horizontal wells can be expressed as

$$T_w(x,t) = T_e + (T_A - T_e)e^{-x/A} \quad \text{.....(2.78)}$$

Comparison of the results of our numerical simulation with the results obtained from Eq. 2.78 can verify the coupled model along the non-communicating sections of the wellbore. This verification is shown in **Fig. 2.10**. In this example, it is assumed that the first 4000 ft of the lateral is not perforated and therefore the calculated wellbore temperature along this portion of the lateral can be used for the verification purpose. We assumed the temperature of injected acid at heel is 80 °F, while formation temperature is 170 °F. **Table 2.3** summarizes the other parameters used for this example.

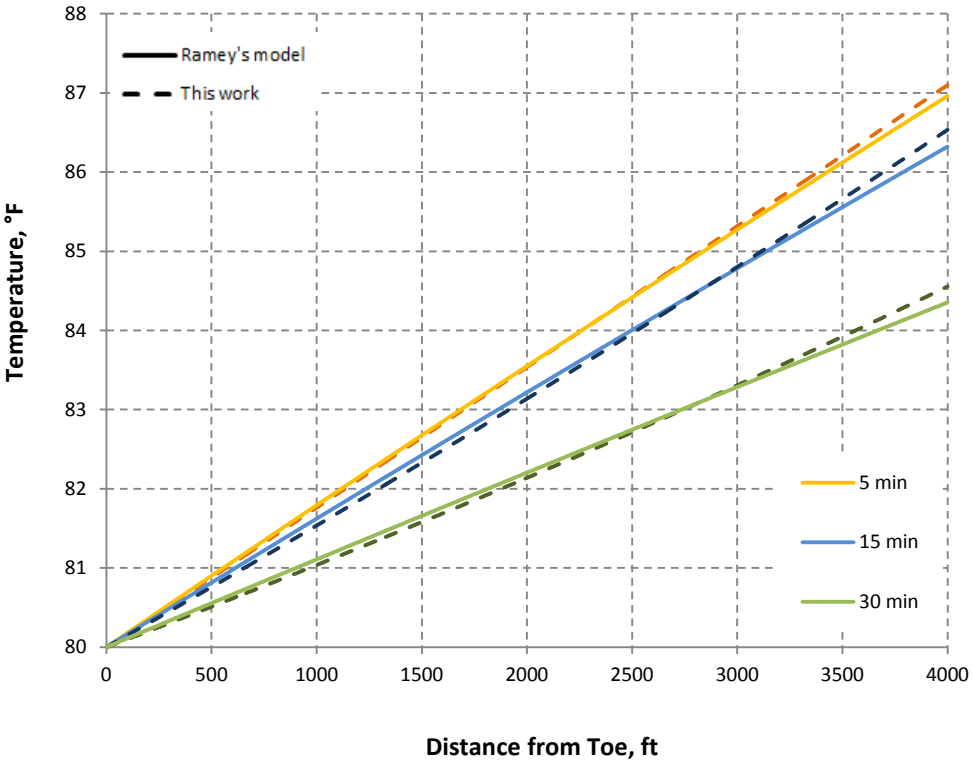

Fig. 2.10—Comparison of our numerical simulation calculated wellbore temperature with modified Ramey's analytical solution.

TABLE 2.3—INPUT DATA USED FOR THE COUPLED MODEL VERIFICATION		
Injection rate (q_{inj})	0.06625 (25)	m^3/sec (bbl/min)
Heat capacity of rock (C_{pR})	1000	J/(kg·K)
Heat capacity of acid (C_{pA})	4187	J/(kg·K)
Density of rock (ρ_R)	2500	kg/m3
Density of acid (ρ_A)	1080	kg/m3
Thermal conductivity of formation (K_f)	3.6	W/(m·K)
Molecular weight of rock (M_R)	0.1	Kg/mol
Injected acid temperature (T_A)	300 (80)	K (ºF)
Reservoir temperature (T_e)	350 (170)	K (ºF)
Wellbore radius (r_w)	0.076 (0.25)	m (ft)
Porosity (ϕ)	0.2	fraction
Pore volume breakthrough (PV_{bt})	0.95	fraction

As we can observe, the simulated temperature profiles matches the temperature profile obtained from the Ramey's modified analytical solution well. The good agreement

between the results confirms the accuracy of the coupled model, specifically verifies that the effect of conduction from the formation is modeled well in the model.

3. FORWARD MODEL RESULTS AND DISCUSSION

3.1 Introduction

In this section, the developed forward model has been applied to several hypothetical cases to study the effects of acid distribution and diversion effectiveness on transient wellbore temperature behavior during both injection and shut-in periods. The objective is to determine if dynamic temperature data can provide us with enough information to identify the acid flow profile. Some sensitivity studies are performed to discuss the factors that affect the temperature behavior during treatments.

The fluid and formation parameters used in this section are given in **Tables 3.1 and 3.2**, respectively.

TABLE 3.1—INJECTED ACID PROPERTIES

Acid type	15 % HCl	
Density of acid (ρ_A)	1080	kg/m^3
Viscosity of acid (μ_A)	0.5	cp
Thermal conductivity of acid (K_A)	0.6	W/(m·K)
Heat capacity of acid (C_{pA})	4187	J/(kg·K)
Injected acid temperature (T_A)	300 (80)	K (ºF)
Acid capacity number (N_{Ac})	0.02	fraction
Pore volume breakthrough (PV_{bt})	0.95	fraction

TABLE 3.2—FORMATION PROPERTIES

Formation type	Limestone	
Density of rock (ρ_R)	2500	kg/m^3
Viscosity of formation fluid (μ_f)	0.5	cp
Thermal conductivity of formation (K_f)	3.6	W/(m·K)
Heat capacity of rock (C_{pR})	1000	J/(kg·K)
Molecular weight of rock (M_R)	0.1	Kg/mol
Reaction heat (Q_{reac})	4855	J/(molHCl)
Reservoir temperature (T_e)	350 (170)	K (ºF)
Average reservoir permeability (k_{avg})	10	md
Porosity (ϕ)	0.2	fraction
Reservoir pressure (P)	3200	psi

3.2 Matrix Acidizing of a Horizontal Well with Cased-Hole Completion

In this example, a 2500 ft horizontal well is considered to be completed with a pre-perforated liner. It is assumed that the liner has five sets of perforations with different length and DTS is installed permanently outside the liner. **Fig. 3.1** illustrates the wellbore configuration, while **Table 3.3** summarizes the dimensions of wellbore and liner.

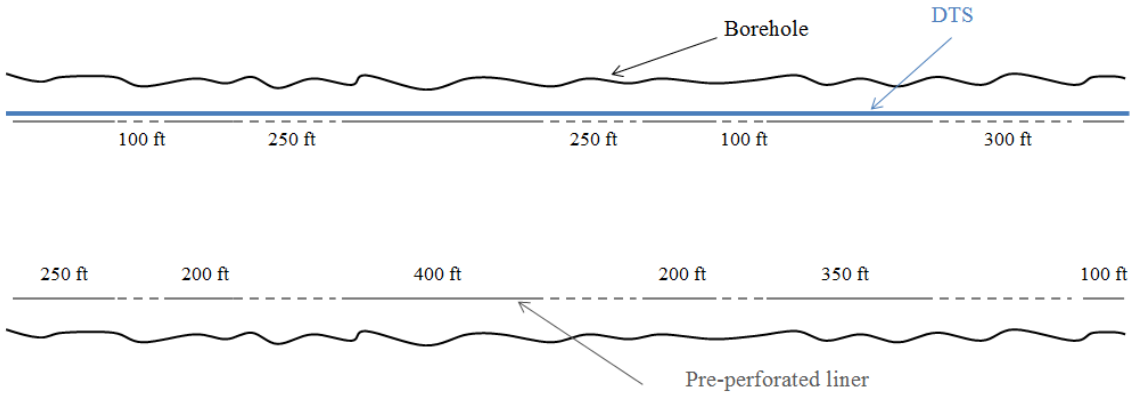

Fig. 3.1—Wellbore configuration assumed in this example.

TABLE 3.3—DIMENSIONS OF WELLBORE AND LINER		
Wellbore length (L)	2500	ft
Wellbore radius (r_w)	0.25	ft
Outer diameter of liner (OD)	5	in
Inner diameter of liner (ID)	4.408	in

It is assumed that the formation is homogeneous along the wellbore while the damage distribution is not uniform, and therefore, each communicating zone has assigned a different initial skin factor as given in **Table 3.4**. Non-uniform damage distribution causes the injectivity of each zone to be different and as a result, acid distributes non-uniformly along the wellbore during the injection. To predict the acid distribution during this treatment, a horizontal well matrix acidizing simulator (Mishra et al. 2007) is used. The treatment is simulated considering the wellbore configuration, fluid and formation

properties and surface injection rate of 10 bpm. The simulated outcomes of this treatment are presented in **Figs. 3.2 through 3.4**. As we can observe, formation damage is being removed (see Fig. 3.2) and the injectivity of each zone is increased during the treatment (see Fig. 3.3). However, since the acid distribution is not uniform, each zone shows a different skin evolution. The acid distribution changes throughout the treatment due to the change of injectivity for each zone. **Table 3.5** summarizes the acid distribution for each perforated zone during this treatment, while Fig. 3.4 shows how the fluid flux changes as a function of injection time for each of these five zones. Initially more acid is injected into the first and third zones. The second zone takes only small portion of the injected acid since it has higher skin factor (Table 3.3). But as the second zone is being stimulated and its formation damage being removed, and also as acid moves down the wellbore and reaches the fourth and fifth zones, the acid distribution becomes uniform. Results suggest that the treatment was successful because after 30 minutes of acid injection, formation damage is removed and the original permeability is restored in all five zones.

TABLE 3.4—ASSUMED INITIAL FORMATION DAMAGE SKIN FACTOR AND LENGTH OF EACH COMMUNICATING ZONE IN THIS EXAMPLE

	Perforation #1	Perforation #2	Perforation #3	Perforation #4	Perforation #5
Perforation length, ft	100	250	250	100	300
Initial skin factor	9.12	38.63	4.39	9.89	2.04
Reservoir permeability, md	10	10	10	10	10

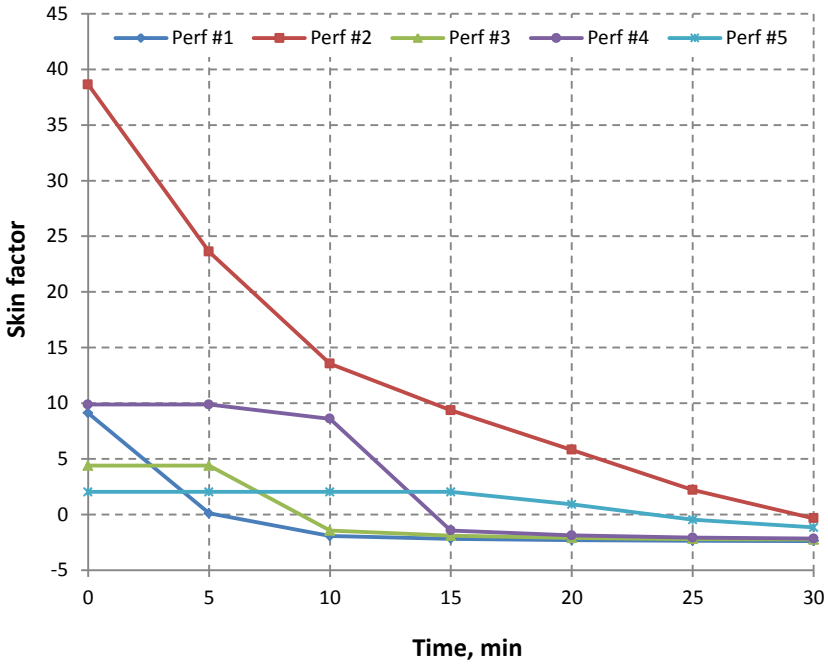

Fig. 3.2—Skin evolution during this treatment.

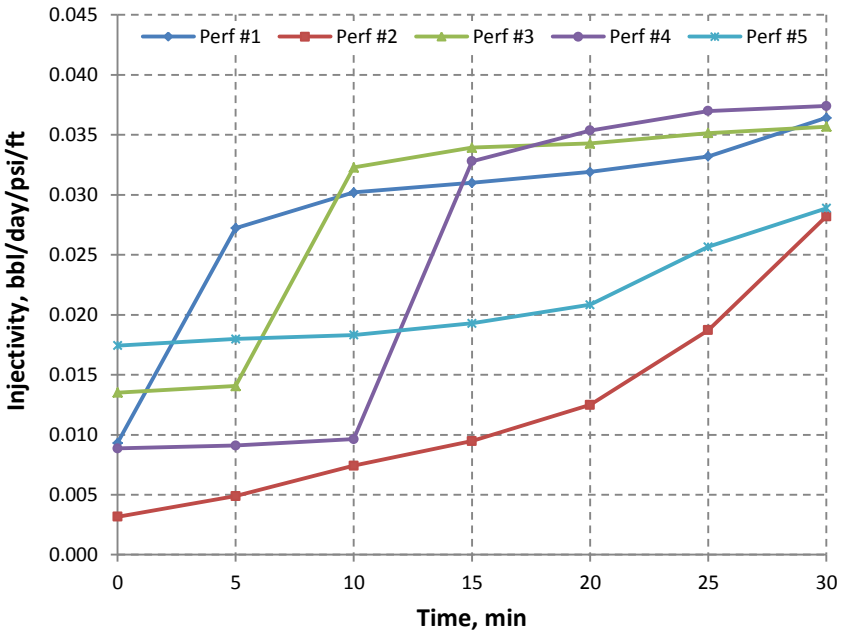

Fig. 3.3—Injectivity evolution during this treatment.

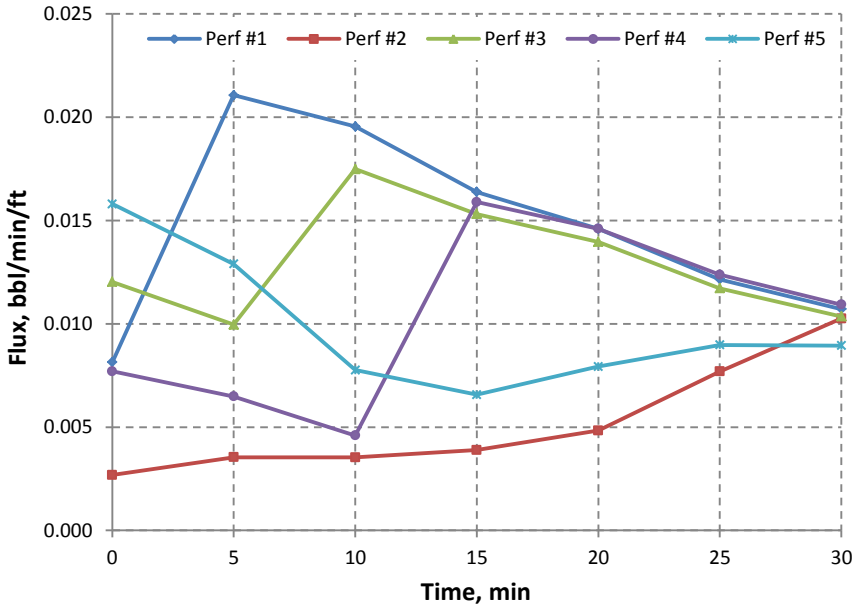

Fig. 3.4—Flux variation during this treatment.

TABLE 3.5—ACID DISTRIBUTION VARIATION DURING THIS TREATMENT							
Time, min	0	5	10	15	20	25	30
Perforation #1	8.1%	21.1%	19.5%	16.4%	14.6%	12.2%	10.7%
Perforation #2	6.7%	8.9%	8.8%	9.7%	12.1%	19.2%	25.6%
Perforation #3	30.1%	24.9%	43.7%	38.3%	34.9%	29.3%	25.9%
Perforation #4	7.7%	6.5%	4.6%	15.9%	14.6%	12.4%	10.9%
Perforation #5	47.4%	38.7%	23.3%	19.7%	23.8%	26.9%	26.8%

Now using the simulated acid distribution (Fig. 3.4 or Table 3.4) as the input for the forward model, the wellbore temperature behavior during this treatment can be predicted. **Fig. 3.5** shows the simulated wellbore temperature profiles. The thermal properties of the liner used to simulate the wellbore temperature are given in **Table 3.6**. As we can observe, temperature data can help us track the acid front movement. This can assist us in determining how far acid is injected down the wellbore or if we are able to treat the entire lateral. Moreover, it can be observed that the wellbore temperature decreases as the cooler fluid is pumped down the wellbore. When the wellbore is being flushed by a

cooler fluid and heat convection makes the temperature decreases, the conduction from the formation will warm the wellbore fluid up. In this process, heat convection dominates the heat transfer. Since the resulting temperature is also determined by how much acid enters into each zone, correctly simulated fluid temperature can help us to evaluate the acid distribution along the wellbore. If we enlarge the bottom part of the Fig. 3.5, we can see (**Fig. 3.6**) that there are some features on temperature profiles that correspond to the flow distribution. These features can help us to interpret the acid distribution from the temperature. For a communicating zone, the temperature feature depends on how much acid is entering the zone and the location of the zone. The amount of acid placed in each zone impacts the effect of conduction from the formation to that section of the wellbore. When acid leaks off into a zone, it causes the near-wellbore region to cool down, and also results in less conduction. **Fig. 3.7** compares the near-wellbore temperature responses of the first (low injectivity) and second (high injectivity) communicating zones and a non-communication section at ten minutes after acid enters these zones or passes by. Four different regions can be distinguished in the near-wellbore temperature response of the communicating sections; the low-temperature section near the wellbore caused by heat convection due to acid leakoff, the dispersed section caused by conduction, the temperature peak caused by reaction heat and finally the region that has not been touched by acid with the original geothermal temperature. The higher injection rate in the first zone causes the fluid to penetrate deeper into the formation and fades the conduction effect toward the wellbore. But the conduction effect at the wellbore in the second zone is still significant due to the low injection rate into this zone or the low convection effect.

Note that, the non-communicating sections only show the second (dispersion due to conduction) and fourth region (geothermal temperature). No convection and reaction associated with these sections since there is no acid leakoff.

In addition to conduction effects, as acid passes through the wellbore and enters the communicating zones, flow rate inside the wellbore decreases which results in less convection effects as we go further down the wellbore. As we can observe from Fig. 3.6, anytime acid passes through the intervals that take fluid, a significant change in the slope occurs on the temperature curve due to reduction in the flow rate and as a results reduction in convection effects beyond this interval.

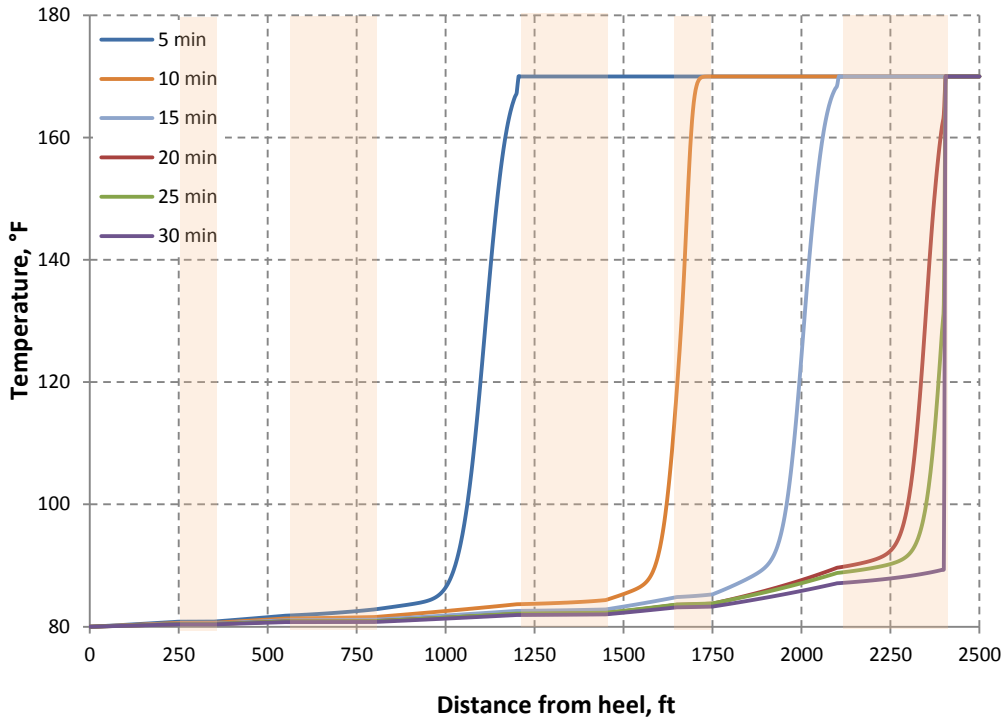

Fig. 3.5—Simulated wellbore temperature behavior during this treatment.

TABLE 3.6—LINER PROPERTIES		
Density of liner (ρ_L)	7800	kg/m^3
Thermal conductivity of liner (K_L)	25	W/(m·K)
Heat capacity of liner (C_{pL})	460	J/(kg·K)

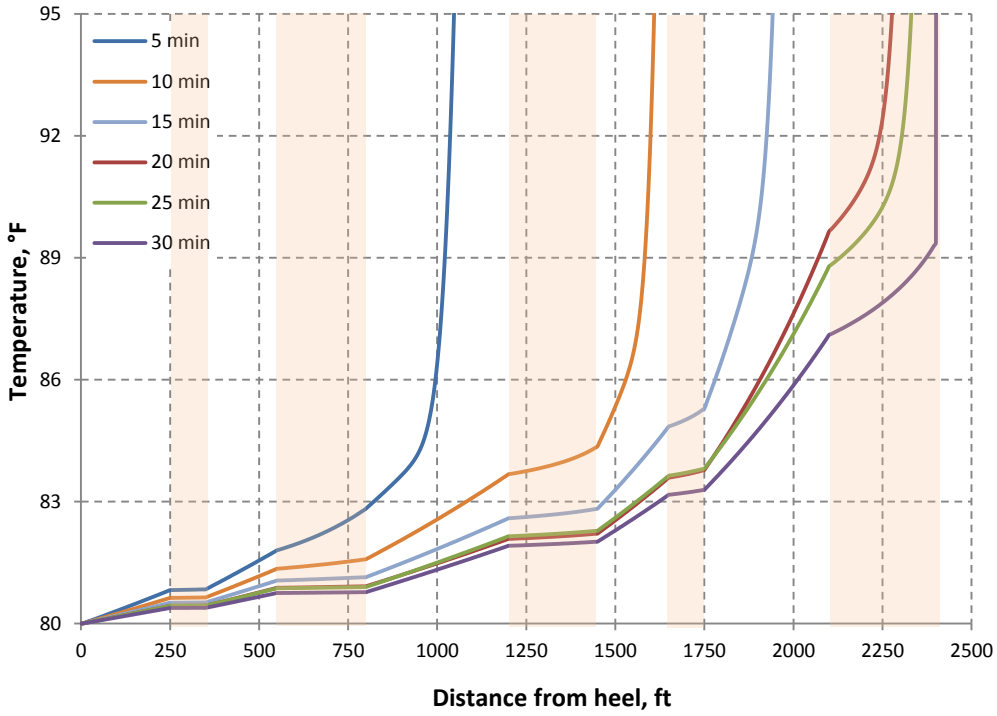

Fig. 3.6—Close-up view of the simulated wellbore temperature behavior.

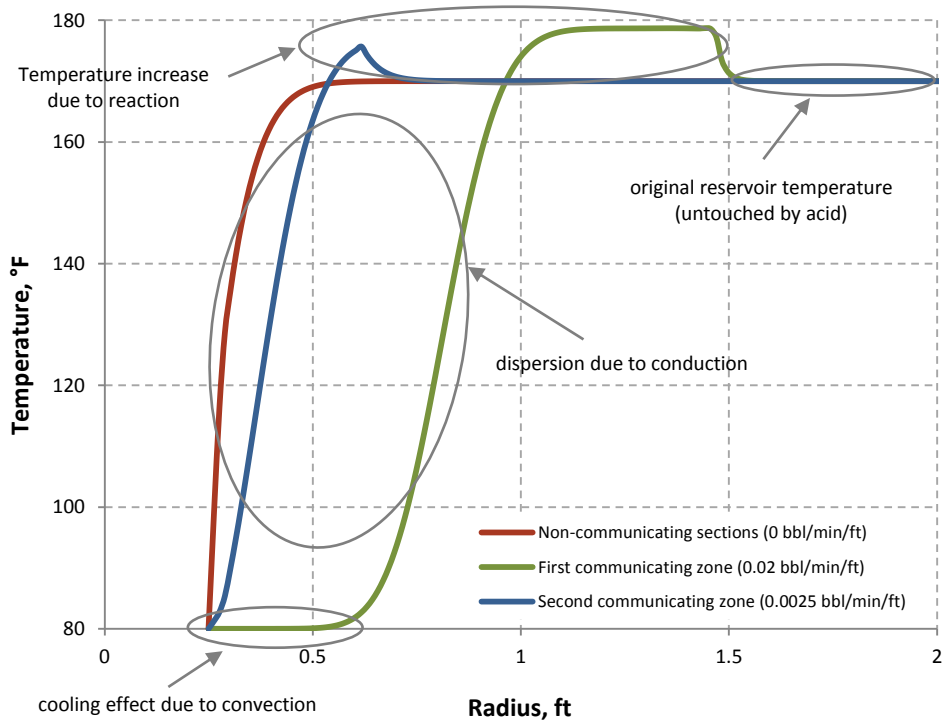

Fig. 3.7—Simulated near-wellbore temperature response for the non-communicating sections and first and second communicating zones.

3.3 Matrix Acidizing of a Horizontal Well with Openhole Completion

In this example we use a 5000 ft horizontal well with openhole completion. The formation along the lateral is presumed to be homogenous with permeability of 10 md, except for two small intervals with relatively higher permeabilities (1000 md). These high-perm zones are located 1800 and 3700 ft from the heel and each one is 25-ft long. Lateral is divided into five sections, three low-perm sections and the two high-perm sections in between. Similar to the previous example, a matrix acidizing simulator for horizontal well is used to simulate the treatment considering 20 bpm injection rate. **Figs. 3.8 through 12** show the simulated results of the acid treatment in this case. Since the low-perm sections are long, therefore skin, injectivity and flux vary along these sections. The results are presented in the form of the average value of kin factor and flux for these sections. The injectivity of the high-perm sections are much higher than the ones for low-perm sections. Therefore, most acid flows into the high-perm zones (higher flux), resulting in insufficient stimulation of the low-perm sections.

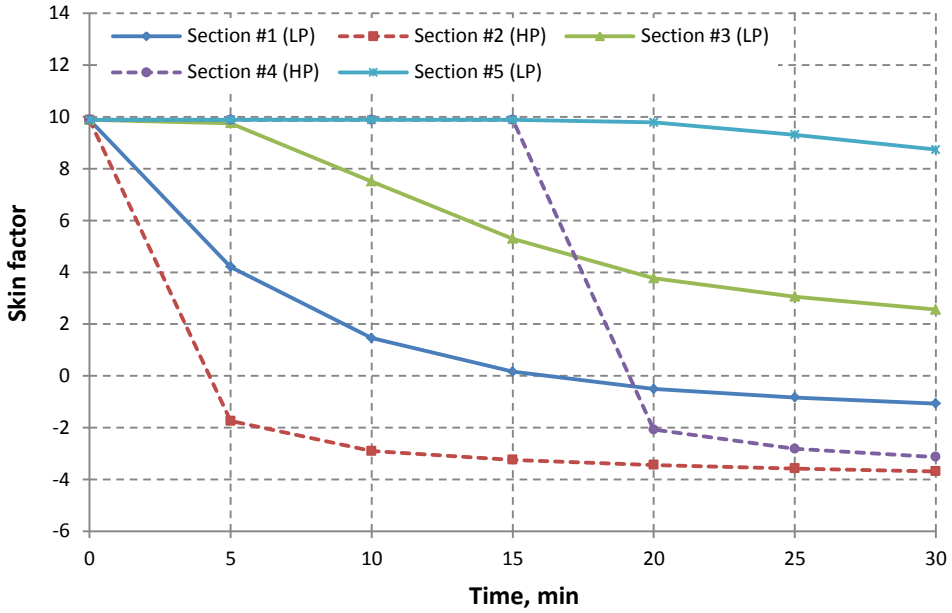

Fig. 3.8—Average skin evolution during this treatment.

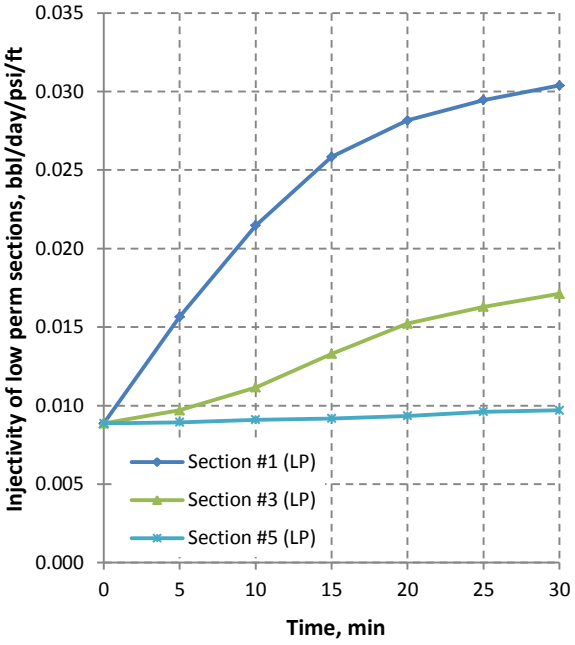

Fig. 3.9—Average injectivity evolution of low-perm sections.

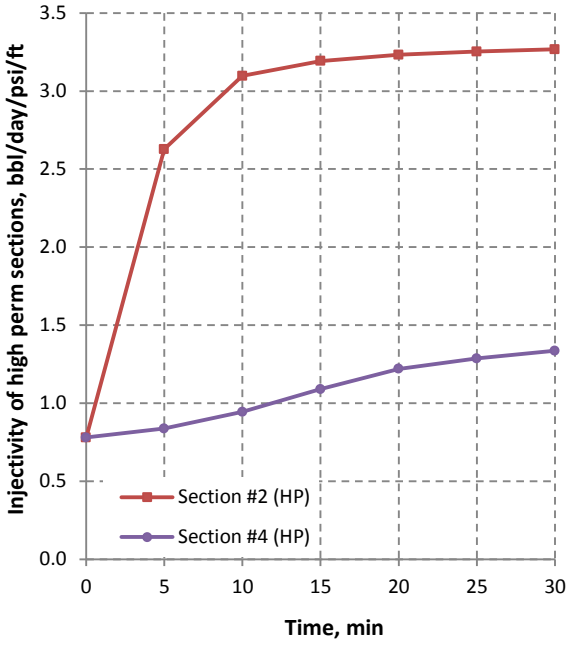

Fig. 3.10—Average injectivity evolution of high-perm sections.

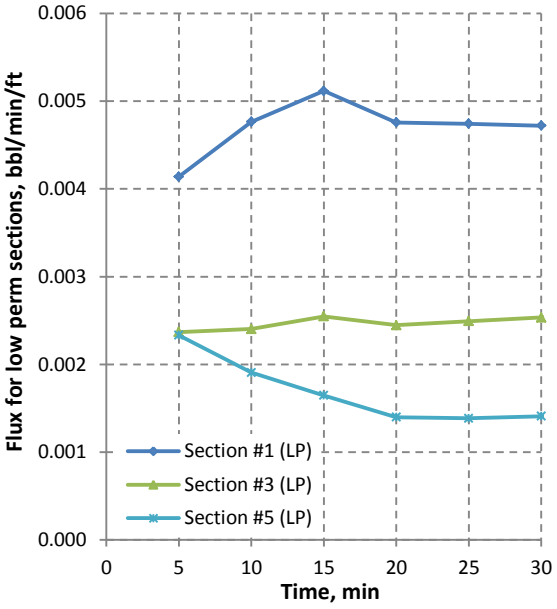

Fig. 3.11—Average flux variation of low-perm sections.

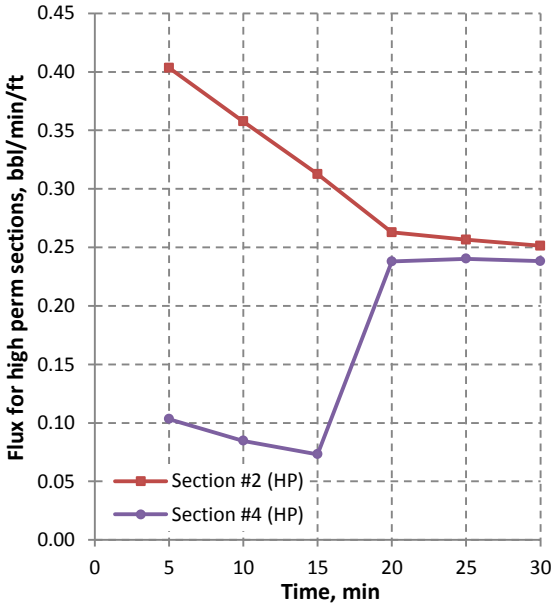

Fig. 3.12—Average flux variation of high-perm sections.

Similar to the previous example, using the acid distribution generated by the simulation as the input for our forward model, we can predict the wellbore temperature

behavior during the treatment. **Fig. 3.13** shows the simulated temperature profiles for this example. Since not much acid enters the low-perm sections, the volumetric flow rate inside the wellbore is high along the first and third sections. This causes the convection to have dominant effect on the wellbore temperature behavior along these sections. Therefore, we observe a rapid cooling in the wellbore. However, temperature data in this case can be used to locate the high-perm zones because as acid passes through these zones, flow rate inside the wellbore decreases significantly. Less convection effects, and therefore, more conduction effects result in a significant change in the slop of the temperature profile as well as the location of the acid front.

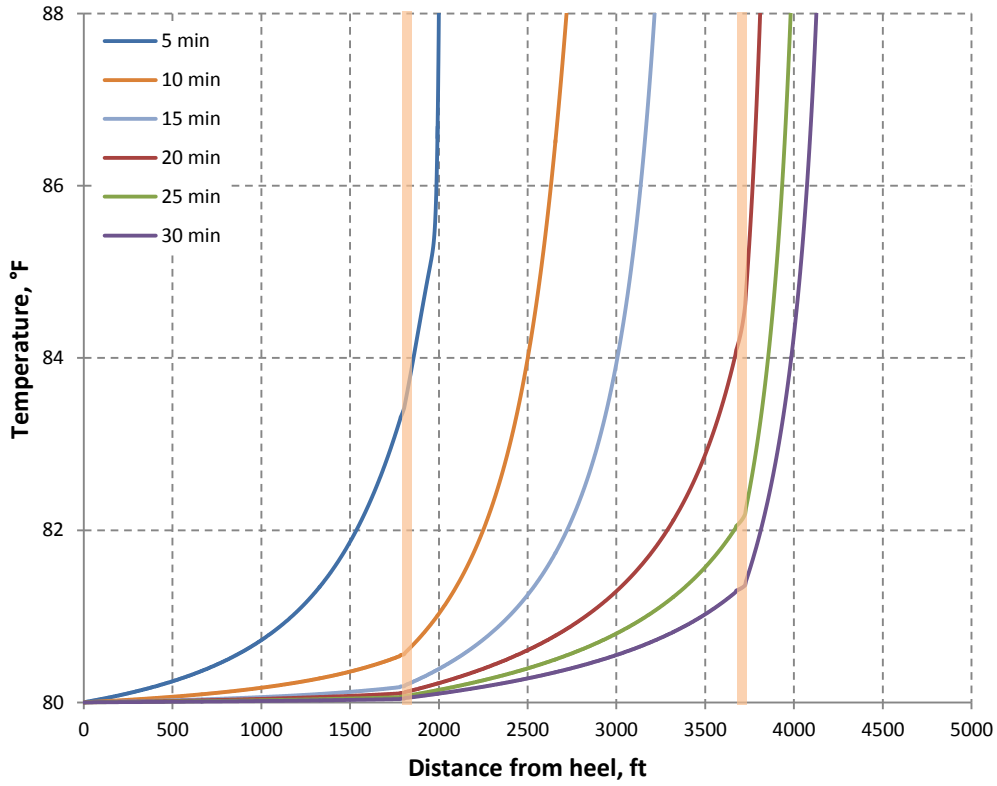

Fig. 3.13—Simulated wellbore temperature behavior during this treatment.

3.4 Effect of Diversion

It was observed that after 30 minutes of injection, the formation damage was not fully removed in the third and fifth sections (see Fig. 3.8). This suggests that diversion may be required to redistribute acid injection profile and divert the fluid from the two high-perm zones to the low-perm sections in this case. We assume following the primary acid injection, viscosified acid is injected for 30 minutes to improve the effectiveness of the treatment. We consider two different scenarios. In the first case, it is assumed that diversion cannot divert acid from high-perm sections to low-perm sections significantly, representing an unsuccessful diversion. In the second case, diversion is assumed to be successful. **Figs. 3.14 through 3.17** show the simulated acid flux for the unsuccessful and successful diversion cases, respectively. As we can see, for the unsuccessful case, flux does not change very much after diversion is applied but for the successful case flux is significantly reduced in the high-perm zones. The simulated temperature data after applying diversion is shown in **Figs. 3.18 and 3.19** for the two cases, respectively. The temperature behaviors of these two cases are distinctively different. This reveals that temperature data can help us to determine the effectiveness of diversion process. When diversion is successful, acid is diverted to the low-perm sections, and as a result, the entire lateral can be stimulated. This can be identified by tracking the acid front in temperature data. In this example, temperature data shows that the entire lateral cools down as a result of successful diversion while for the unsuccessful diversion, the last 500 ft of the lateral shows almost no change in the temperature compared with the initial temperature.

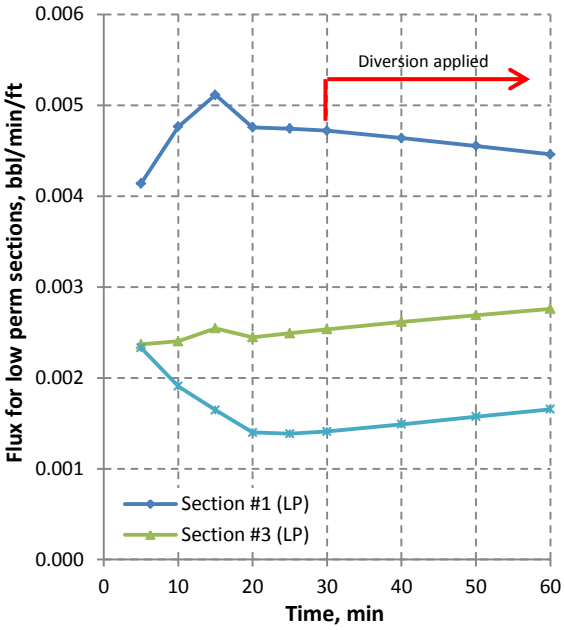

Fig. 3.14—Average flux variation of low-perm sections after an unsuccessful diversion.

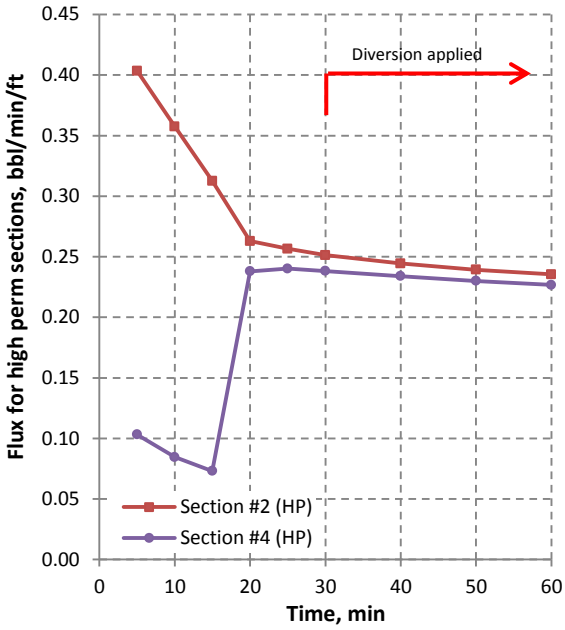

Fig. 3.15—Average flux variation of high-perm sections after an unsuccessful diversion.

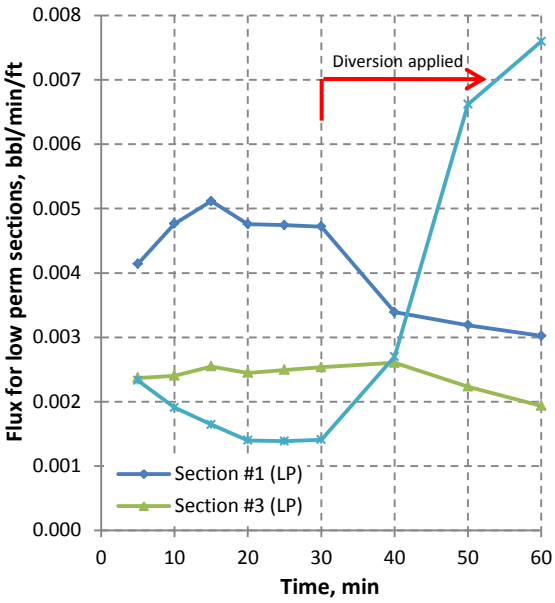

Fig. 3.16—Average flux variation of low-perm sections after a successful diversion.

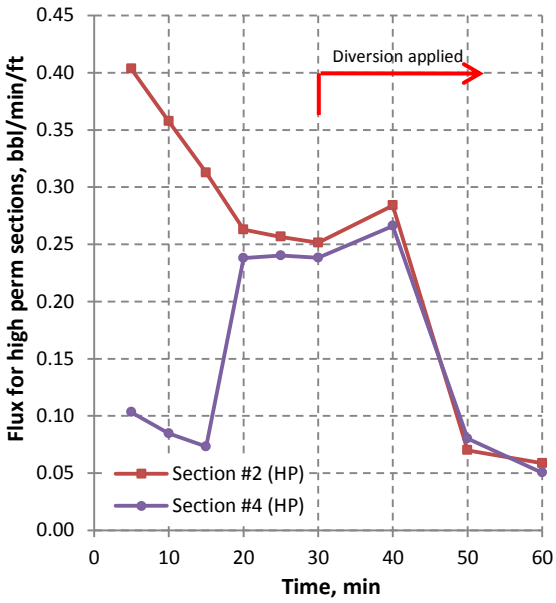

Fig. 3.17—Average flux variation of high-perm sections after a successful diversion.

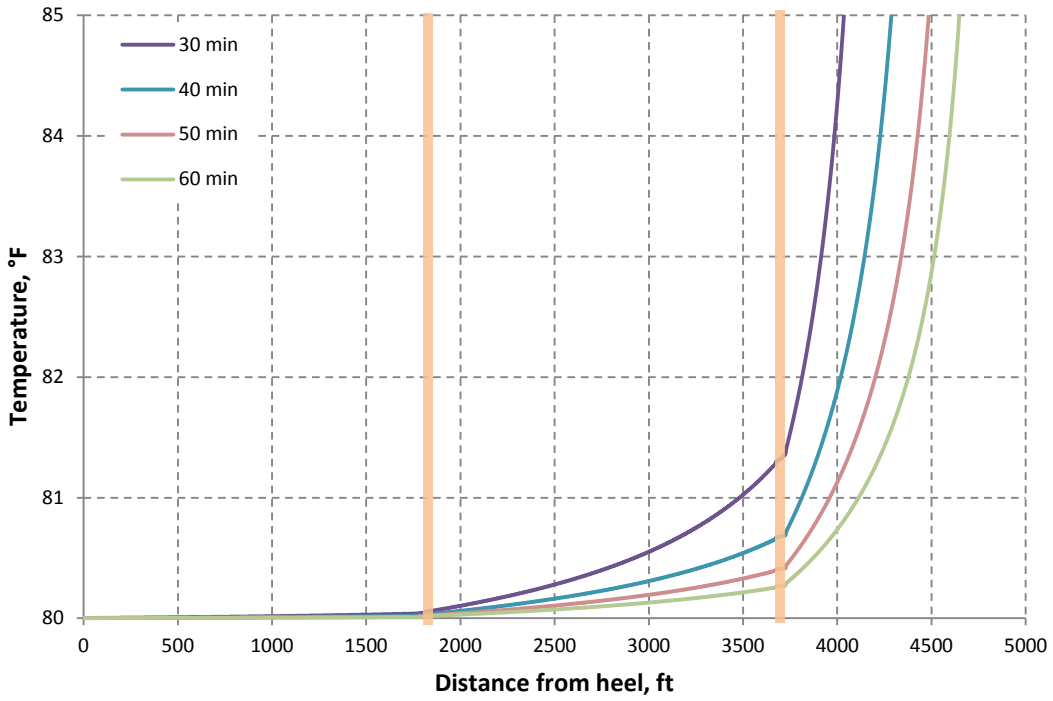

Fig. 3.18—Simulated wellbore temperature behavior after an unsuccessful diversion.

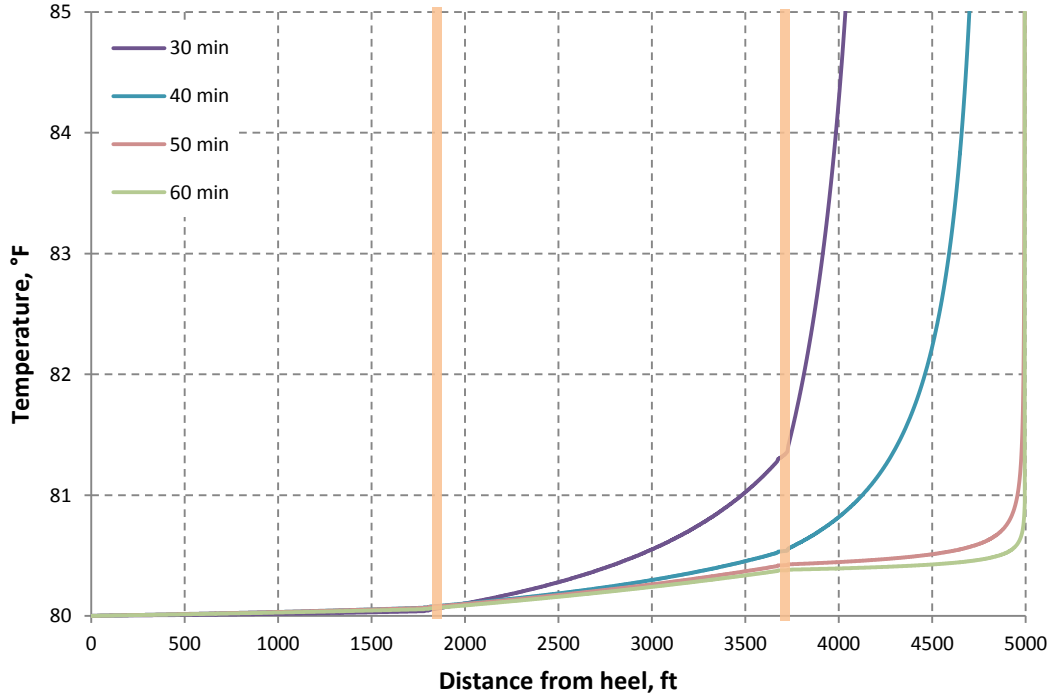

Fig. 3.19—Simulated wellbore temperature behavior after a successful diversion.

3.5 Effect of Injection Rate

According to the forward model convection has a significant impact on temperature behavior during treatment. It cools down the wellbore and the near-wellbore region. Convection is mainly controlled by volumetric flow rate inside the wellbore which is a function of injection rate and acid distribution. Previously we discussed how acid distribution affects the temperature profile and in this section we investigate the effect of surface injection rate on temperature behavior during acid treatments. We use the same example as in the previous section. We assume three different injection rates for acid stimulation. Although different injection rates results in different acid distribution and acidizing outcome, we assume the same acid distribution for comparison purpose. So that, the temperature behavior during the treatment is simulated considering the acid distribution given in Table 3.4 and injection rate of 5, 10 and 15 bpm. **Fig. 3.20** shows a comparison between the temperature profiles of these three different injection rates. The first observation is that the acid front is different. Acid front is about 1700 ft far from the heel after 20 minutes when injection rate is 5 bpm, and is 2250 ft and 2350 ft when injection rate is 10 and 20 bpm, respectively. We can observe that cooling occurs much faster when injection rate is higher. This is because, convection is dominant in higher injection rate and conduction effect is not significant enough to impact the temperature behavior. In case of very high injection rate, cooling can occur very fast and this can make the interpretation of the temperature data very difficult.

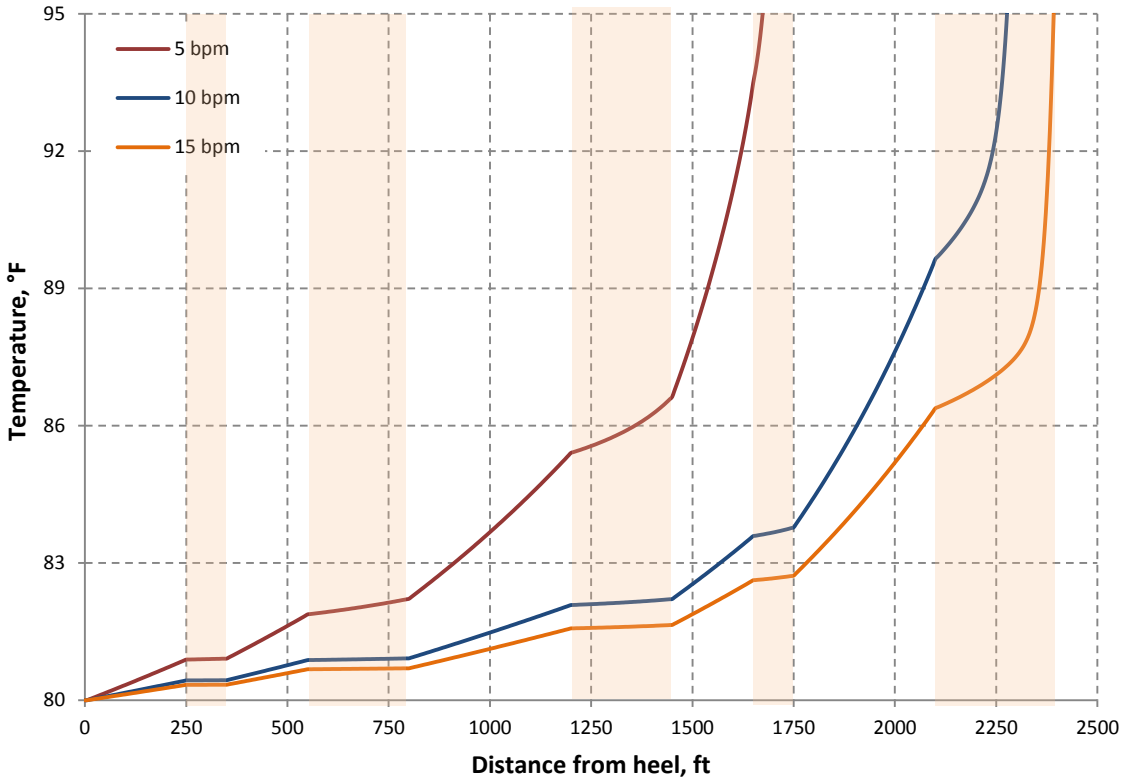

Fig. 3.20—Simulated wellbore temperature behavior for different injection rates.

3.6 Effect of Formation Temperature

The temperature difference between injected acid and formation controls the conduction from the formation to the wellbore which is the main source of information in interpretation of the temperature data. Higher temperature difference between formation and injected fluid, results in higher conduction and therefore more information to interpret the acid distribution from the temperature data. **Fig. 3.21** illustrates the simulated temperature behavior for three different formation temperatures, 120, 170 and 240 °F. Injected acid temperature and other parameters are assumed to be the same as the ones used in the first example. It can be observed that when the temperature difference is small (T_e=120 °F), conduction effect is very insignificant while higher temperature difference (T_e=170 °F or T_e=240 °F) cause more conduction and therefore more

temperature difference along the wellbore. For example, after 20 minutes of injection the entire wellbore has almost the same temperature (only 5 °F temperature difference along the wellbore) when formation temperature is 120 °F, while the temperature difference along the wellbore is about 10 °F and 20°F when formation temperature is 170 °F and 240 °F, respectively. Therefore, the interpretation of the temperature data is much easier when the temperature difference between injected acid and formation is high.

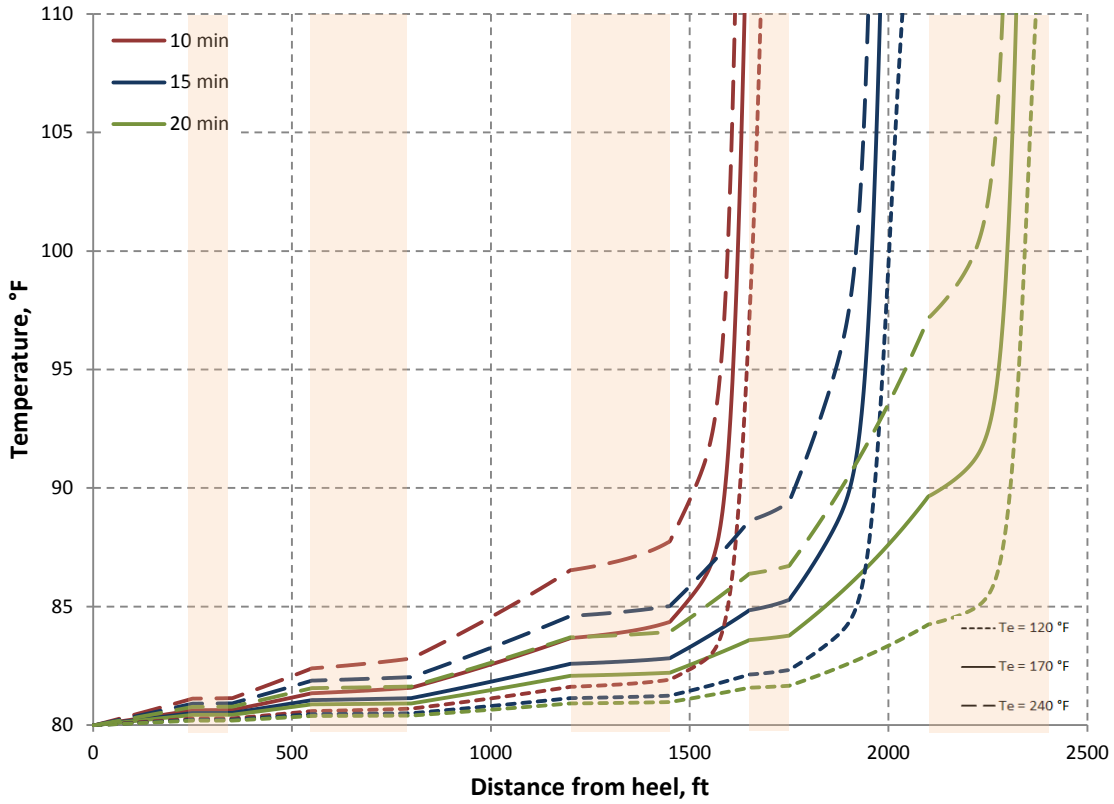

Fig. 3.21—Simulated wellbore temperature behavior for different formation temperatures.

3.7 Effect of Formation Type

Formation type affects the wellbore temperature behavior in two different ways. It determines the rate of conduction from formation to wellbore which is controlled by the thermal properties of the formation. It also controls the amount of heat generated by

chemical reaction between formation and acid. The heat of reaction is controlled by the acid type and the minerals present in the formation. In this study we mainly focus on carbonate rocks which are usually either limestone or dolomite. The thermal properties of these two types of rock are not very different (Thomas, 1973), thus the rate of conduction for both is almost the same. But when they react with hydrochloric acid (HCl) their heat of reaction is not the same. Therefore, the acid stimulation of limestone and dolomite can cause different wellbore temperature behavior. To investigate the effect of formation type on wellbore temperature behavior, we first calculate the reaction heat of hydrochloric acid and different carbonate rocks (limestone and dolomite). Then assuming the same condition used in the previous example, the wellbore temperature behavior during acid stimulation for both limestone and dolomite are simulated and compared.

Heat generated from a reaction is expressed as enthalpy of reaction or energy change of a reaction (ΔH). If the energy is required, ΔH is positive, and if energy is released, ΔH is negative. Heat of reaction can be calculated as

$$Q_{reac} = \Delta H = \sum \Delta H_{\text{product}} - \sum \Delta H_{\text{reactant}} \quad \text{.....(3.1)}$$

where Q_{reac} is the reaction heat and $\Delta H_{\text{product}}$ and $\Delta H_{\text{reactant}}$ are the enthalpies of formation of all products and reactants, respectively.

Note that, the enthalpy of formation of a compound (ΔH) is the change of enthalpy that accompanies the formation of one mole of a substance in its standard state from its constituent elements in their standard states (the most stable form of the element at one bar of pressure and the specified temperature, usually 298.15 K or 25 degrees Celsius).

The reaction between limestone and dolomite can be written as

Limestone: $2HCl + CaCO_3 \rightarrow CaCl_2 + CO_2 + H_2O$ .....(3.2)

Dolomite: $4HCl + CaMg(CO_3)_2 \rightarrow CaCl_2 + MgCl_2 + 2CO_2 + 2H_2O$ .....(3.3)

According to the definition of the heat of reaction (Eq. 3.1) and the enthalpies of the reactant and products that are given in **Table 3.7**, the reaction heat of limestone and dolomite with HCl is 1.16 kcal/molHCl (4855 J/molHCl) and 1.36 kcal/molHCl (5692 J/molHCl), respectively. Following shows the calculation of the reaction heat of limestone and dolomite.

$$Q_{reac}\Big|_{Limestone} = \frac{1}{2}\left[(-209.15)+(-94.05)+(-68.32)\right]-\left[2\times(-39.85)+(-289.5)\right] \quad \text{.....(3.4)}$$
$$= 1.16\ \text{kcal}$$

$$Q_{reac}\Big|_{dolomite} = \frac{1}{4}\left[(-209.15)+(-189.76)+2\times(-94.05)+2\times(-68.32)\right] \quad \text{.....(3.5)}$$
$$-\left[4\times(-39.85)+(-558.8)\right] = 1.36\ \text{kcal}$$

TABLE 3.7—ENTHALPY OF THE REACTANTS AND PRODUTCS (Perry et al. 1963)

Substance	ΔH, kcal/mol
$CaCo_3$	-289.5
$CaMg(CO_3)_2$	-558.8
$CaCl_2$	-209.15
$MgCl_2$	-189.76
HCl	-39.85
H_2O	-68.32
CO_2	-94.05

Using the calculated reaction heats, the forward model is applied to simulate the wellbore temperature behavior during the acid stimulation of both limestone and dolomite. The simulated temperature profiles are shown in **Fig. 3.22**. As we can see, the wellbore temperature for dolomite is slightly higher than the one for limestone. This is because the reaction heat of hydrochloric acid and dolomite is higher than the reaction heat of hydrochloric acid and limestone. However, the difference in wellbore temperature

response for these two formation types is very small and negligible. The reason for the small difference is that the higher reaction heat of dolomite causes a tiny increase in the peak in the near-wellbore temperature response, and this has an insignificant effect on the temperature gradient at the wellbore as shown in **Fig. 3.23**. Therefore, it can be concluded that the formation type has an insignificant effect on temperature response.

It should be noted that, the primary objective of this work was to study the real-time monitoring of horizontal wells in carbonate reservoirs. However, if the formation is sandstone, the general approach developed in this study is still valid. The only issue that needs to be considered is the different acid leak-off mechanisms in sandstone and carbonate reservoirs. In carbonate reservoirs acid leaks off into the formation by creating wormholes while in sandstone, it penetrates radially. This difference shows up in the calculation of reaction heat in the forward model. Therefore, this part of the forward model needs to be modified if it is intended to apply this study to an acid stimulation treatment in sandstone reservoir.

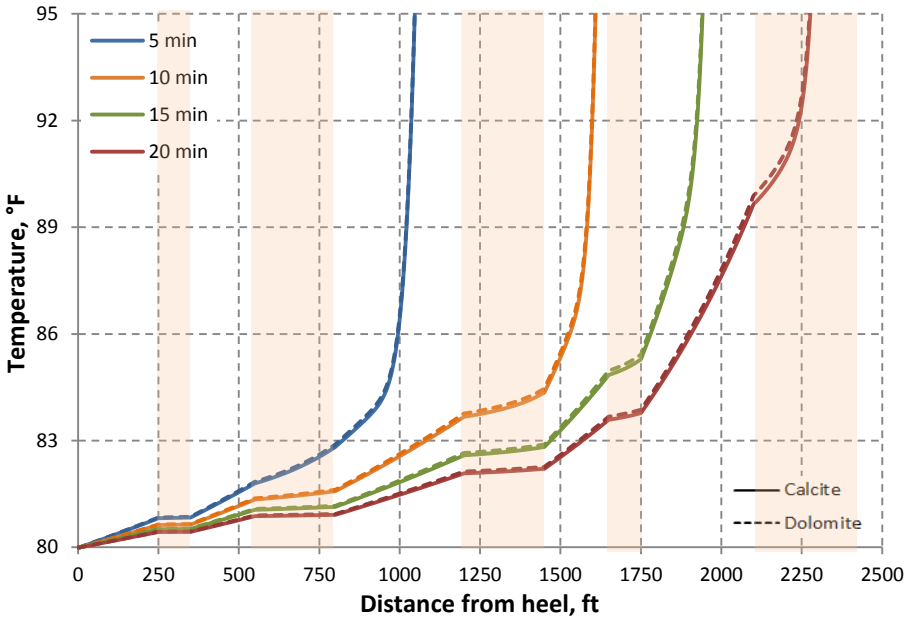

Fig. 3.22—Simulated wellbore temperature behavior for limestone and dolomite.

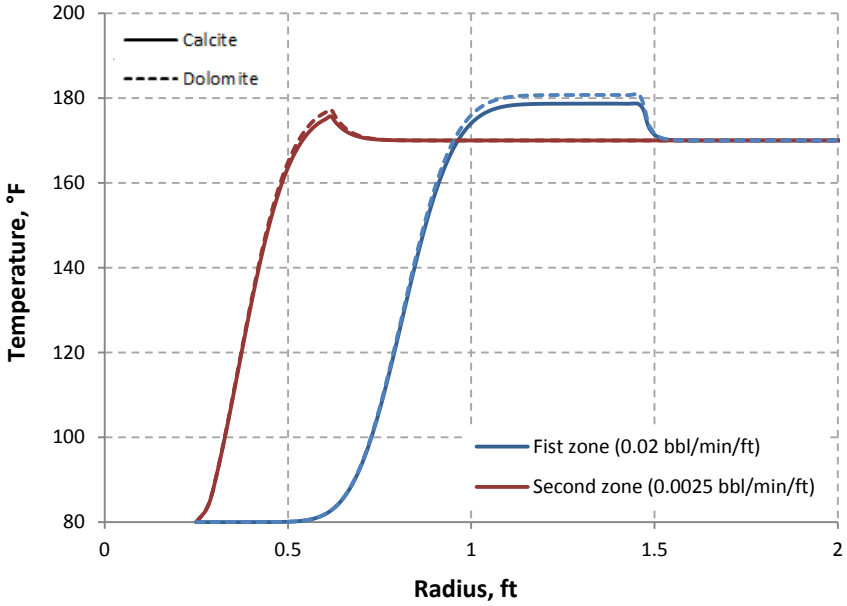

Fig. 3.23—Simulated near-wellbore temperature response for limestone and dolomite.

3.8 Wellbore Temperature Behavior during Shut-In

If a well is shut in for a while after acid injection and we keep monitoring the wellbore temperature, we should be able to extract additional information about the acid injection distribution. As we discussed earlier, during injection, wellbore cooling may limit the ability to analyze the temperature data, especially when the injection rate is very high. However, since it is very unlikely that crossflow occurs in horizontal well during shut-in, we can assume that there is no convection, and therefore, conduction is the only heat transfer mechanism affecting the wellbore temperature. Conduction from the formation causes the wellbore temperature to warm up. The locations that take more acid during the injection will warm up slower compared with the locations that take less acid. The temperature information during shut-in can help to confirm the acid injection distribution.

To simulate the wellbore temperature behavior during shut-in, the forward model for simulation of temperature behavior during injection can be applied with some

modifications. Since there is no convection during shut-in, all the convection terms in the model needs to be disregarded. In addition, it is assumed that during shut-in no reaction occurs between acid and rocks, therefore, the reaction term in the near-wellbore model is not included.

In this section, considering the horizontal well matrix acidizing examples discussed earlier, the modified forward model is applied to simulate the wellbore temperature behavior during shut-in. It is assumed that wells are shut-in for half an hour after the injection. **Fig. 3.24** illustrates the simulated temperature profiles right before and during the shut-in for the cased-hole horizontal well example. As we can see, all non-communicating sections warm back much faster than the communicating sections. However, communicating zones warm back with different rates. The rate of warm back in a zone depends on how much acid is placed into the zone. In this case, the second and the last zones warm back faster than the others since less acid is placed into these zones.

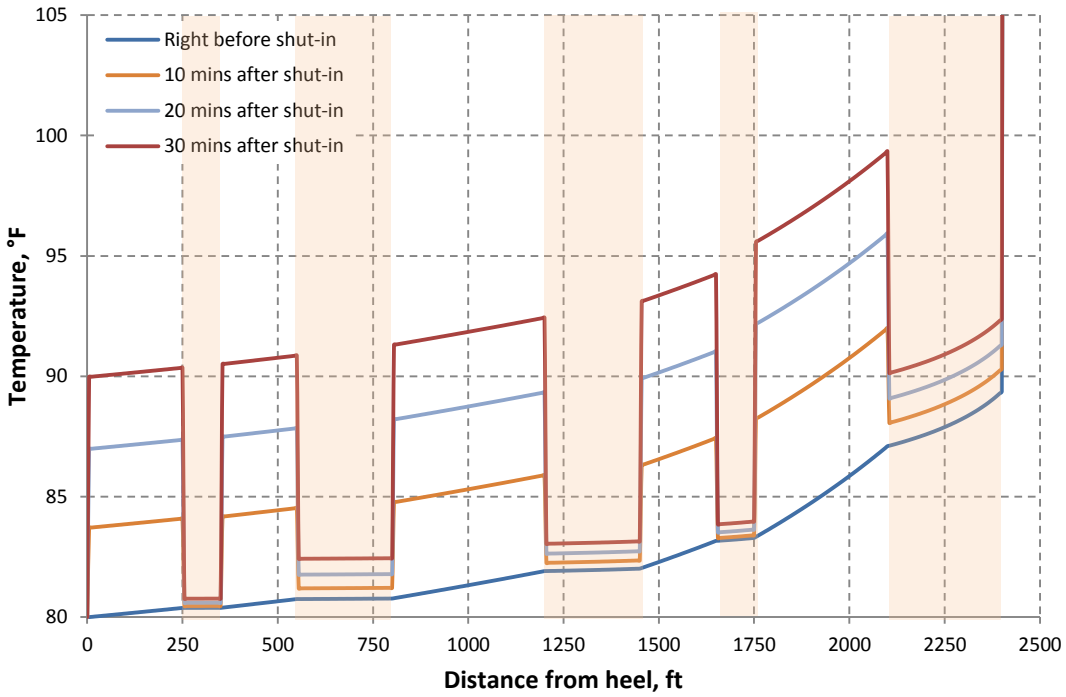

Fig. 3.24—Simulated shut-in temperature behavior of the cased-hole example.

Figures 3.25 and 3.26 show the simulated temperature profiles right before and during the shut-in for the unsuccessful and successful diversion cases of openhole horizontal well example. It can be observed that the high-perm sections show different temperature behavior than the low-perm zones. The high perm zones do not show any sign of warm-back even after 30 minutes, while low-perm sections warm back a couple of degrees. In addition, we can observe that each low-perm section warms back with different rate. This is because the fluid loss that occurs before the second and third low-perm sections reduces the amount of acid placed into these sections.

A comparison between the shut-in temperature behavior of the unsuccessful and successful diversion cases reveals that the shut-in temperature behavior of these two cases are significantly different. The low-perm section close to the toe warm backs faster when diversion is not successful because small amount of acid is placed into this section. When diversion is successful, this part of the lateral warm backs slower since more acid is placed into this section compared to the unsuccessful case.

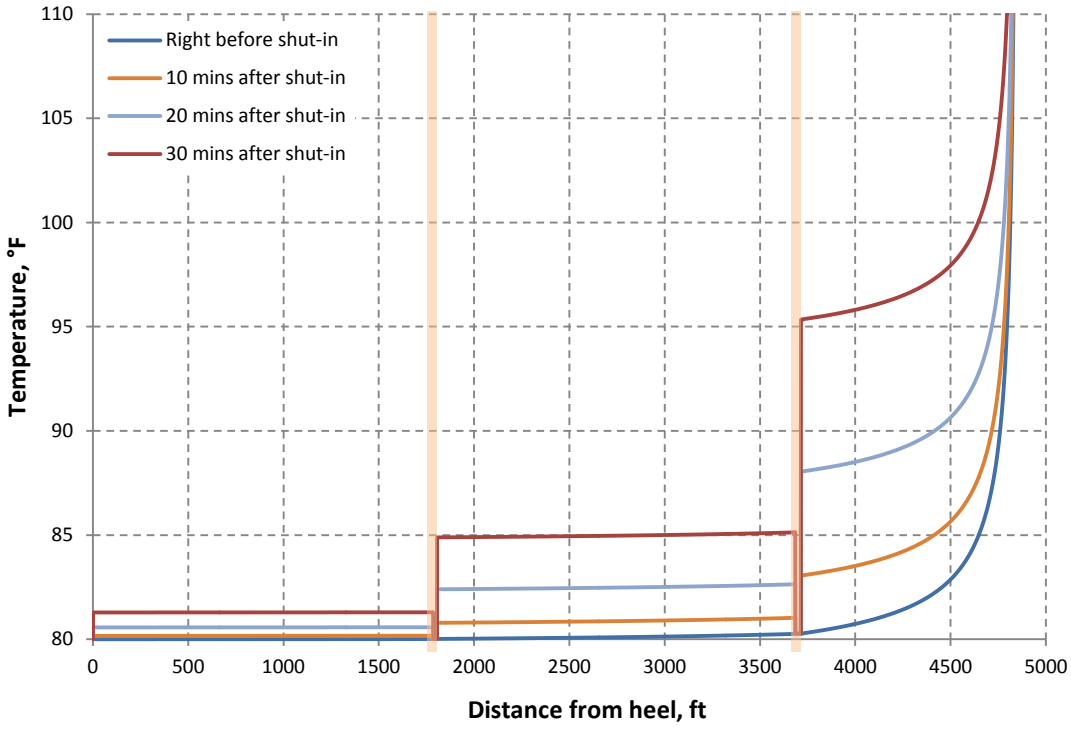

Fig. 3.25—Simulated shut-in temperature behavior of the unsuccessful diversion case of the openhole example.

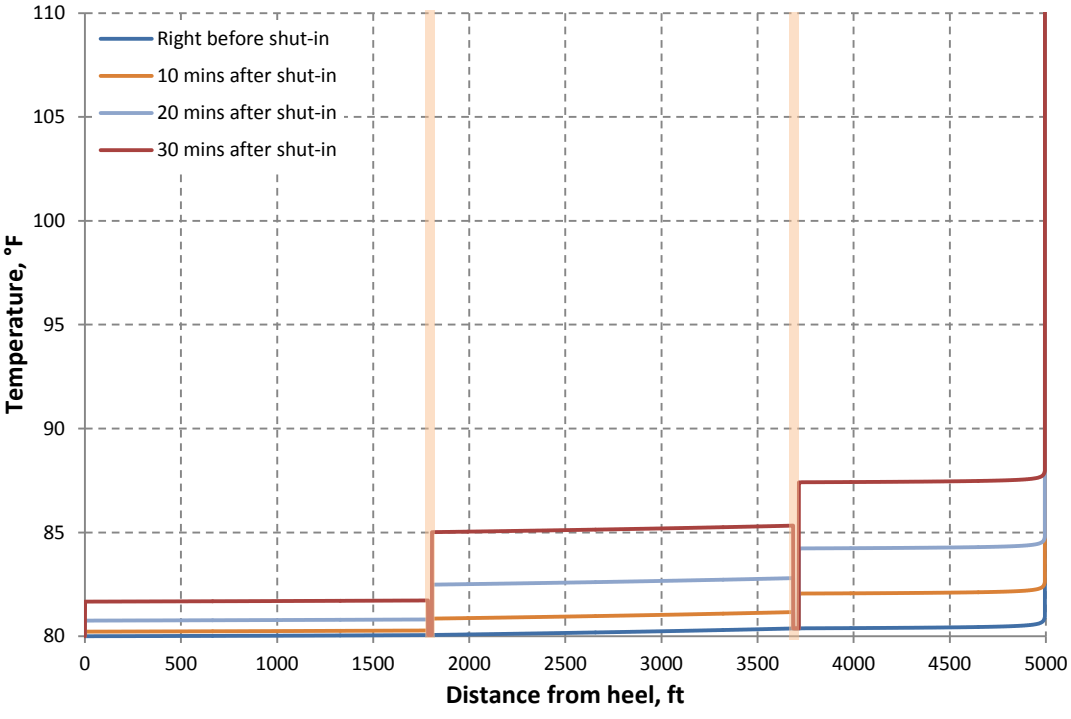

Fig. 3.26—Simulated shut-in temperature behavior of the successful diversion case of the openhole example.

4. INVERSE MODEL DEVELOPMENT

4.1 Introduction

The forward model described in the previous section is used to simulate the wellbore temperature behavior during treatment as wells as identify the key factors affecting the temperature data. In this section, we present an inversion procedure (inverse model) to interpret the acid distribution along the wellbore from the dynamic temperature data measured during an acid stimulation treatment.

Inverse models can be considered as a least-squares nonlinear regression problem. They search a particular domain and find the solution by minimizing the objective function which describes the discrepancy between measured and simulated data. The general form of an objective function can be written as (Oliver et al., 2008)

$$f(\mathbf{x}) = \frac{1}{2}\left(\mathbf{d} - g(\mathbf{x})\right)^T \mathbf{C}_n^{-1}\left(\mathbf{d} - g(\mathbf{x})\right) \quad \text{.....(4.1)}$$

where $\mathbf{x}$ represents the parameters vector, $\mathbf{d}$ is the vector of the observed data, g denotes the forward model, and $\mathbf{C}_n$ is the covariance matrix to take into account measurement errors or different units of different type of data. The objective function can also be written as

$$f(\mathbf{x}) = \frac{1}{2}\mathbf{e}^T\mathbf{e} \quad \text{.....(4.2)}$$

where $\mathbf{e}$ is the residual vector between observation and forward model calculation, and can be expressed as

$$\mathbf{e} = \mathbf{C}_n^{-1/2}\left(\mathbf{d} - g(\mathbf{x})\right) \quad \text{.....(4.3)}$$

In this study, we regard the wellbore temperature profile as observed data and acid distribution as the parameter to be estimated from the temperature. The objective function for this case is simplified to

$$f(\mathbf{x}) = \sum_{i=1}^{N} (T_{obs} - T_{cal})^2 \quad \text{.....(4.4)}$$

where N represents the number of measured or calculated temperature data along the wellbore and T_{obs} and T_{cal} refer to the measured and forward model calculated temperature data, respectively.

The general idea of the inverse model is to start with an initial guess of acid distribution and run the forward model to simulate the temperature profile until we match the measured the temperature data. The most important steps in between is how to update the parameter vector to provide accurate results with minimum computation time.

In general there are two types of inversion methods, stochastic methods and Gauss-Newton or gradient-based methods. The main difference between these two methods is the algorithm being used to update the parameters. Gradient-based inversion methods update the parameters by calculating the search vector using the gradient or the Hessian of the objective function. This requires the calculation of parameter sensitivities, which are partial derivatives of the observed data with respect to model parameters. Generally, the gradient-based methods provide faster convergence. However, they perform poorly in cases of highly non-linear systems which in these cases the method may result in local minima. In such a case, a unique solution is not guaranteed. Stochastic methods can avoid the local minimum problem because they can update the parameters by searching the global parameter space. The main drawback of stochastic methods is that when the

parameter number is large, computation becomes expensive, which hinders its application in some cases.

In this study, we investigated Levenberg-Marquardt (L-M) algorithm (Marqardt, 1963, Oliver et al., 2008) as a gradient-based method and Markov chain Monte Carlo (MCMC) algorithm (Hastings, 1970, Robert and Casella, 1999, Oliver et al., 1997 and Wadsley, 2005) as a stochastic method. The following describes these two inversion methods in detail and then we introduce a procedure to efficiently invert the measured temperature data during an acid stimulation treatment.

4.2 Markov Chain Monte Carlo Method

The general idea of MCMC method is to construct a Markov chain by sampling from a proposal distribution. In this case, the proposal distribution is uniform because all the samples have the same probability. The algorithm for implementing this method follows these steps:

1. Start with an initial guess for acid injection distribution. In this study, if there is no prior information we assume the acid distribution is uniform.
2. Run the forward model and calculate the wellbore temperature profile ($\mathbf{T}_n$).
3. Use Eq. 4.4 to calculate the objective function (f_n).
4. Update the assumed acid distribution ($\mathbf{q}_n$) by generating a new one ($\mathbf{q}_{n+1}$) from a proposal distribution which in this study a uniform probability distribution is assumed.
5. Use the new guess for the acid distribution ($\mathbf{q}_{n+1}$) and run the forward model again to calculate a new wellbore temperature profile ($\mathbf{T}_{n+1}$).

6. Calculate the new objective function (f_{n+1}).
7. Use the Metropolis-Hastings criterion (Metropolis et al., 1953) to accept the new guess of acid distribution ($\mathbf{q}_{n+1}$) as

$$\rho(\mathbf{x}_n, \mathbf{x}_{n+1}) = \min\left(1, \frac{q(\mathbf{x}_n \mid \mathbf{x}_{n+1})\,\pi(\mathbf{x}_{n+1})}{q(\mathbf{x}_{n+1} \mid \mathbf{x}_n)\,\pi(\mathbf{x}_n)}\right) \quad \text{.....(4.5)}$$

where in this case,

$$\mathbf{x}_n = \mathbf{q}_n \quad \text{.....(4.6)}$$

$$\pi(\mathbf{x}_n) = e^{-f_n} \quad \text{.....(4.7)}$$

and $q(\mathbf{x}_{n+1} \mid \mathbf{x}_n) = q(\mathbf{x}_n \mid \mathbf{x}_{n+1})$ since a uniform probability distribution is assumed. Therefore, we have

$$\rho(\mathbf{q}_n, \mathbf{q}_{n+1}) = \min\left(1, \frac{e^{-f_{n+1}}}{e^{-f_n}}\right) \quad \text{.....(4.8)}$$

8. If the new guess for acid distribution is accepted, use this value for the acid distribution and follow steps 2 to 7 to update the acid injection distribution until temperature history is matched. if it is not accepted go to step 4 and generate a new guess (another $\mathbf{q}_{n+1}$) from the proposal distribution and repeat the following steps.

Full MCMC procedure is computationally expensive mainly because the acceptance rate of direct MCMC is usually small and most proposals will be rejected since sampling in MCMC is random and independent of the parameters to be estimated. One way to improve the full MCMC is to increase the acceptance rate by modifying the proposal. Ma et al. (2008) proposed a modified MCMC algorithm (random walk MCMC algorithm) where the proposal distribution is modified by perturbing the current acid distribution. It

means that we first guess an acid distribution from independent uniform distribution, and then use this guess to constrain the new one as

$$\mathbf{q}_{n+1} = \mathbf{q}_n + \Delta\mathbf{q}_n \quad \text{.....(4.9)}$$

where in this study, the small perturbation ($\Delta\mathbf{q}_n$) is set to be about 10% of the $\mathbf{q}_n$ ($\Delta\mathbf{q}_n$=0.1$\mathbf{q}_n$).

In step 4, if the new acid distribution generated form the uniform probability distribution does not satisfy the constraint (Eq. 4.9), we reject it and generate a new one until it agrees with the constraint.

4.3 Levenberg-Marquardt Method

The Levenberg-Marquardt algorithm is a blend of the Gauss-Newton method and the gradient descent method (Oliver et al, 2008). In spite of the MCMC method which parameter vector is updated arbitrary by sampling from a proposal distribution, in this method the parameter vector is updated by adding a gradient-relative term at each iteration step as follows:

$$\mathbf{x}_{n+1} = \mathbf{x}_n + \delta\mathbf{x}_n \quad \text{.....(4.10)}$$

where

$$\delta\mathbf{x}_n = -(\mathbf{H} + \lambda\mathbf{I})^{-1}\mathbf{J}^T\mathbf{e} \quad \text{.....(4.11)}$$

H in this equation is the Hessian matrix of the objective function, $f(\mathbf{x})$. For low residuals or quasi-linear system, the Hessian matrix can be approximated by (Data-Gupta and King, 2007)

$$\mathbf{H} = \mathbf{J}^T\mathbf{J} \quad \text{.....(4.12)}$$

where **J** is the Jacobian matrix which is defined as the gradient of **e**.

$$\mathbf{J} = \nabla \mathbf{e} \quad \text{.....(4.13)}$$

Considering the definition of the residual vector, **e**, which is described by Eq. 4.3, the Jacobian matrix can be written as

$$\mathbf{J} = \nabla\left[\mathbf{C}_n^{-1/2}\left(\mathbf{d} - g(\mathbf{x})\right)\right] = -\mathbf{C}_n^{-1/2}\nabla g(\mathbf{x}) \quad \text{.....(4.14)}$$

where in this equation, ∇ g(**x**) is the sensitivity matrix of the forward model, **G**, which defines how the i^{th} data, $\mathbf{d}_i = g_i(\mathbf{x})$, is affected by changes in the j^{th} model parameter, $\mathbf{x}_j$. It can be calculated as

$$\mathbf{G} = \nabla g(\mathbf{x}) = \begin{bmatrix} \frac{\partial g_1}{\partial \mathbf{x}_1} & \frac{\partial g_1}{\partial \mathbf{x}_2} & \cdots & \frac{\partial g_1}{\partial \mathbf{x}_M} \\ \frac{\partial g_2}{\partial \mathbf{x}_1} & \frac{\partial g_2}{\partial \mathbf{x}_2} & \cdots & \frac{\partial g_2}{\partial \mathbf{x}_M} \\ \vdots & \vdots & \ddots & \vdots \\ \frac{\partial g_N}{\partial \mathbf{x}_1} & \frac{\partial g_N}{\partial \mathbf{x}_2} & \cdots & \frac{\partial g_N}{\partial \mathbf{x}_M} \end{bmatrix}_{N \times M} \quad \text{.....(4.15)}$$

where M and N are the number of parameters and the number of observed data, respectively.

If there is no analytical solution for the forward model as in this case, the sensitivity matrix can be calculated by perturbation method. For example, the first element in the matrix can be obtained by

$$\frac{\partial g_1}{\partial \mathbf{x}_1} = \frac{g_1(\mathbf{x}_1 + \Delta\mathbf{x}_1, \mathbf{x}_2, \cdots, \mathbf{x}_M) - g_1(\mathbf{x}_1, \mathbf{x}_2, \cdots, \mathbf{x}_M)}{\Delta\mathbf{x}_1} \quad \text{.....(4.16)}$$

Each column of the sensitivity matrix requires one forward simulation run; therefore, to obtain the sensitivity matrix, M forward simulation runs are needed.

The procedure to implement the L-M method is very simple and follows these steps:

1. Start with an initial guess for acid distribution.
2. Run the forward model and calculate the wellbore temperature profile ($\mathbf{T}_n$) and

then calculate the objective function (f_n).

3. Compute the sensitivity matrix, $\mathbf{G}_n$, with perturbation method. In this study, we set the perturbation to 10% of the parameter ($\Delta\mathbf{x}_i=0.1\mathbf{x}_i$).
4. Calculate the search vector ($\delta\mathbf{x}$ or in this case $\delta\mathbf{q}$) as

$$\delta\mathbf{q}_n = \delta\mathbf{x}_n = -(\mathbf{G}^T\mathbf{C}_n^{-1}\mathbf{G} + \lambda\mathbf{I})^{-1}\mathbf{G}^T\mathbf{C}_n^{-1}(\mathbf{d} - g(\mathbf{x})) \quad \text{.....(4.17)}$$

Note that, the value of damping factor, λ, can affect updating the parameters and consequently the computation time. In this study λ is set to be equal to the average of the eigenvalue of the Hessian matrix.

5. Update the acid injection distribution as

$$\mathbf{q}_{n+1} = \mathbf{q}_n + \delta\mathbf{q}_n \quad \text{.....(4.18)}$$

6. Run the forward model again and obtain the new wellbore temperature profile ($\mathbf{T}_{n+1}$) and then calculate the new objective function (f_{n+1}).
7. Repeat steps 2 through 6 until the following criterion meets.

$$\left|\frac{f_{n+1} - f_n}{f_n}\right| < \varepsilon \quad \text{.....(4.19)}$$

where ε is a small residual that defines the desired level of accuracy.

4.4 Inversion Procedure

To be able to monitor and evaluate the acid stimulation treatment in real-time, a fast inversion procedure is necessary. In this section, we introduce a fast procedure for inverting the temperature data during acid stimulation treatment and determining the injection profile. This procedure can be used for both inversion algorithms described above (MCMC or LM).

We use the example of 2500-ft long horizontal well presented in the previous section to demonstrate this procedure. The observed temperature data is in a perfect condition since it is generated by the forward model. Also the true injection profile is known. The impact of noise and resolution on inversion results will be investigated later in the next section. All inversion results in this section and the next section are presented in terms of flux and the unit is bbl/min/ft.

Figure 4.1 shows the observed temperature profile after five minutes of injection. The temperature profile indicates that at 5 minutes of injection, the acid front has passed the first and second perforation zones and has not reached the other zones. Therefore, this profile can only provide us with some information about the injection profile of the first 1000 ft of the wellbore.

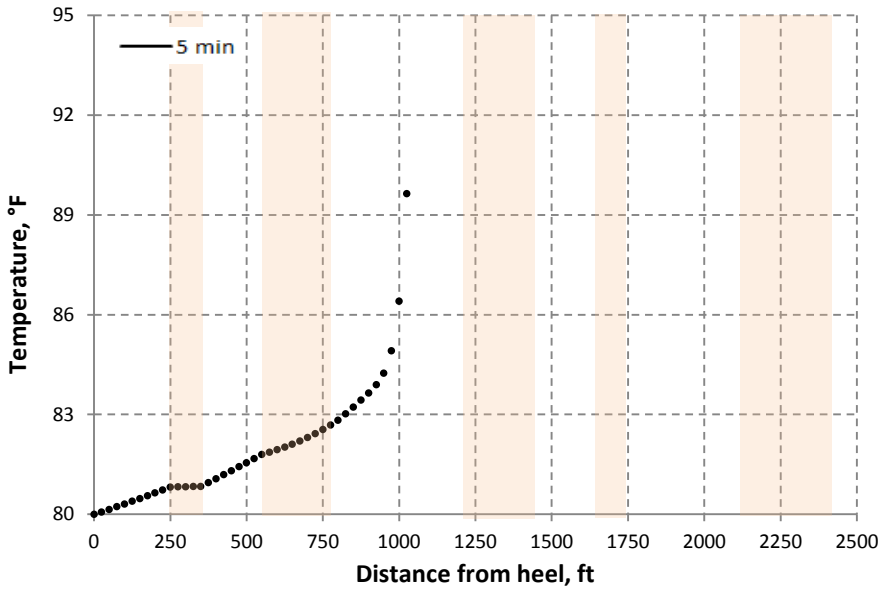

Fig. 4.1—Observed temperature profile after five minutes of injection.

There are two different ways to invert this profile. One way is inverting the entire profile at one step which requires solving the inverse problem for two parameters, flux associate with the first and second zones. This method can be challenging because the

inverse problem is required to be solved for more than one parameter. We first applied the LM method to invert the temperature profile but the inversion did not converge since the relationship between the acid distribution and temperature profile is highly non-linear. **Fig. 4.2** illustrates three different views of the objective function for this case. Objective function looks like a valley (see Figs. 4.2a and b). However, down this valley where the values of the objective function are very low, the objective function looks like a bended saw (Fig. 4.2c). Although a global minimum can be found in this objective function, there are a lot of local minima. Gradient-based inversion methods fail to solve this inverse problem because the search vector traps in these local minima and is not able to find the global minimum.

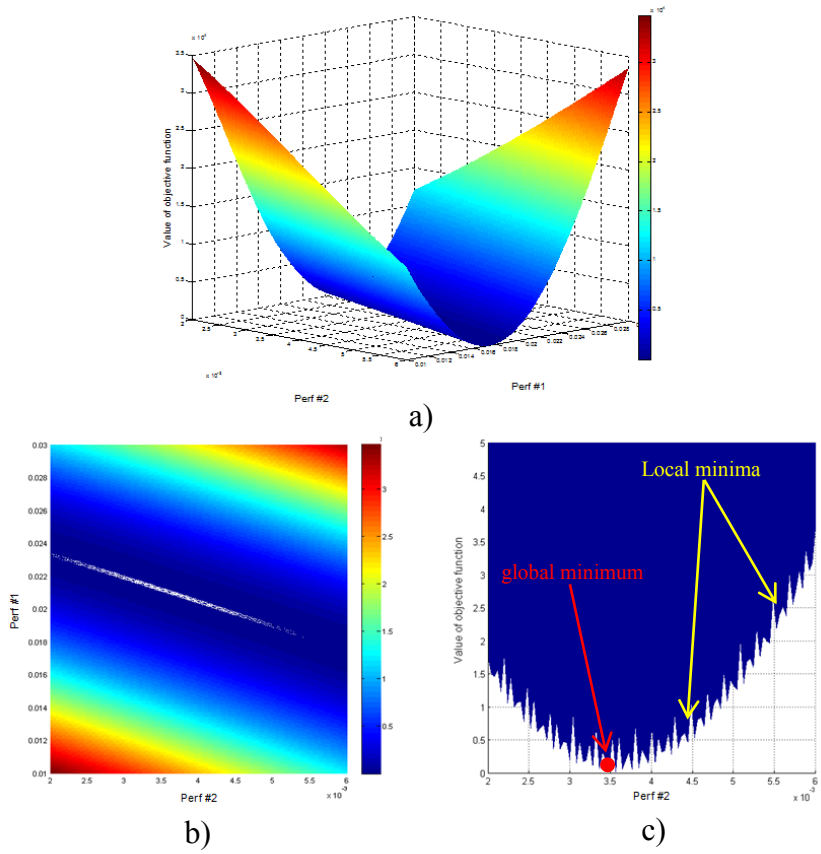

Fig. 4.2—Different views of the objective function for this case.

Stochastic inversion methods can avoid the local minimum problem since they search the global parameter space but the computation time can be longer than it is desired. **Fig. 4.3** shows the inverted temperature profile using MCMC method versus the observed data and **Table 4.1** summarizes the inversion results. Meanwhile, **Fig. 4.4** shows the convergence rate of the MCMC method for inverting this temperature profile and solving for the flux associated with the first and second zones. As we can see, if we stop the inversion after about 1000 iterations, the inversion results show about 6% error. Although temperature match looks good, the results are not in acceptable range because 6% error is too much considering the observed data is ideal and noise free. Therefore, this inversion procedure (inverting the entire profile at one step) is not a very good solution for this problem, especially when we want to invert the later profiles. For later profiles acid passes through more zones and therefore, we have to solve the inverse problem for larger number of parameters. To efficiently invert the temperature profile, we divide the profile into two parts, one from the heel to the beginning of the second set of perforations and the other one is the rest of the profile. Then these two parts of the profile can be inverted separately. The first part is inverted first and then the second part can be inverted based on the inversion result of the first part. With this procedure, we only need to solve for one parameter at each step. Although two inversions are required to be performed, this procedure is much faster than the previous one. In addition, since we are solving for only one parameter, inversion can be performed applying both MCMC and LM methods without any problem and both result in a unique answer.

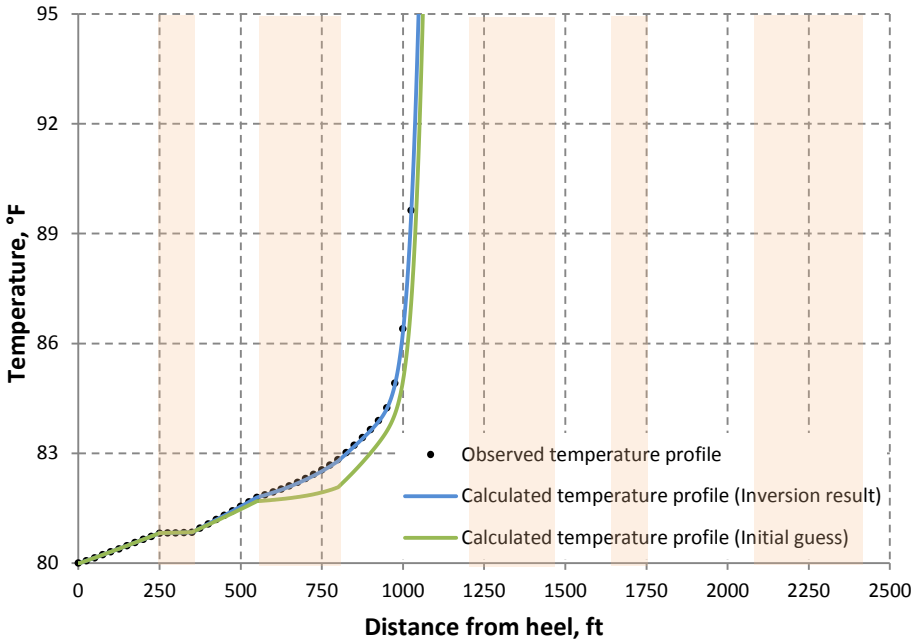

Fig. 4.3—Inverted temperature profile versus observed data.

TABLE 4.1—INVERSION RESULTS FOR THE FIRST AND SECOND SETS OF PERFORATION USING MCMC METHOD

	Perf #1	Perf #2
Initial guess	0.01	0.01
Calculated	0.02070	0.00380
True	0.02110	0.00356
Error (%)	**1.90**	**6.74**

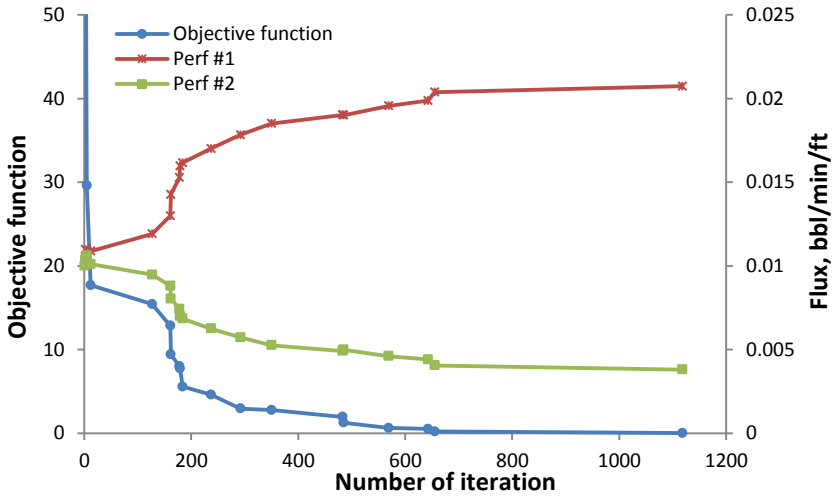

Fig. 4.4—Objective function and flux convergence using MCMC method.

Figures 4.5 and 4.6 show the inverted temperature profile for the first and the second parts, respectively. As we can observe, there is a good agreement between the observed and inverted temperature profiles. The inversion results for the first and second sets of perforations are given in **Tables 4.2 and 4.3** showing that the results from both MCMC and LM methods are very accurate and error is less than 1%.

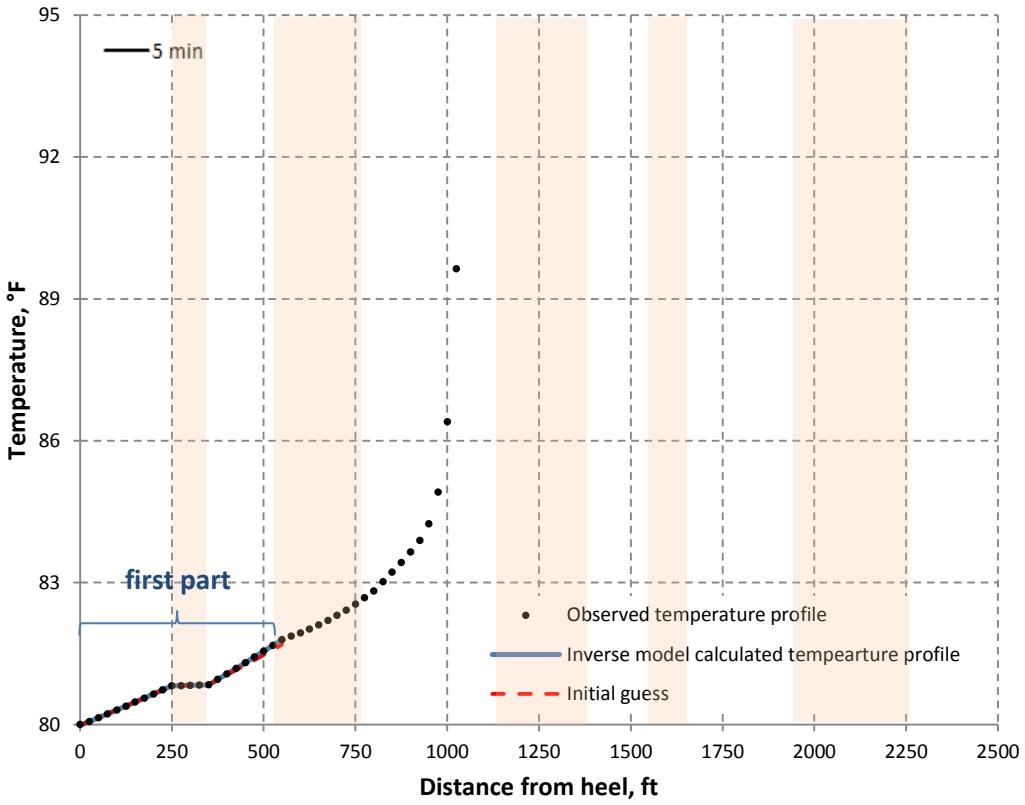

Fig. 4.5—Inverted temperature profile versus observed data (first part of the data).

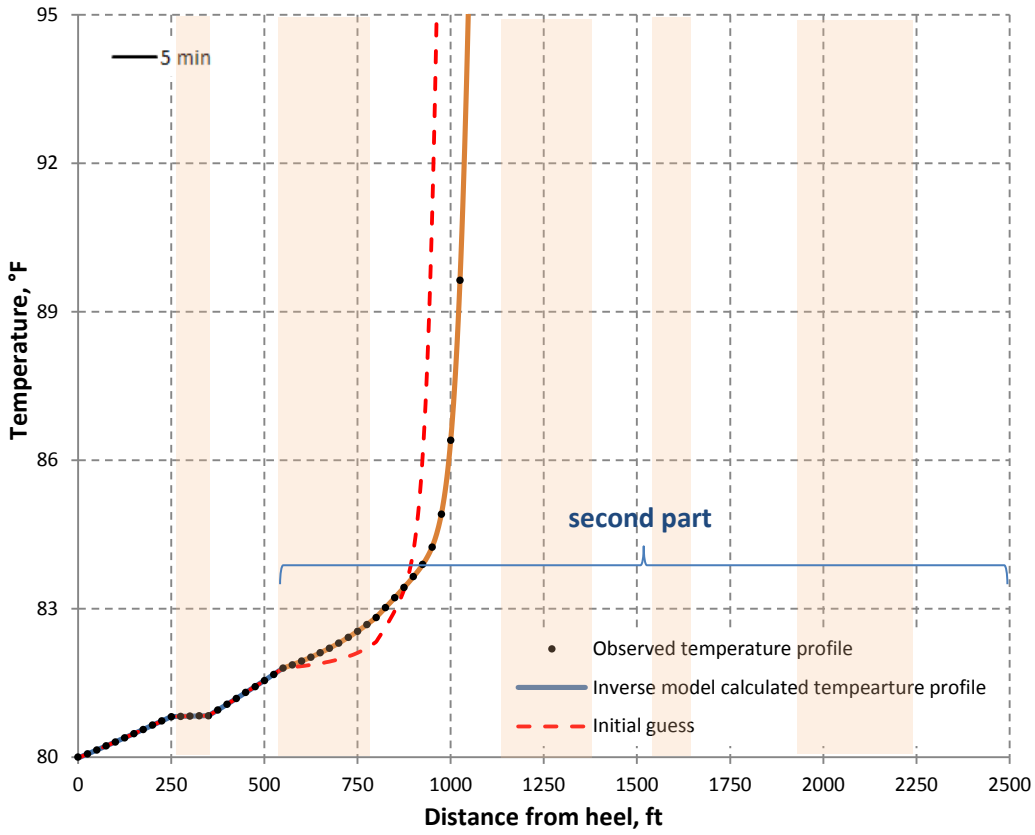

Fig. 4.6—Inverted temperature profile versus observed data (second part of the data).

TABLE 4.2—INVERSION RESULTS FOR THE FISRT SET OF PERORATION		
	Perf #1-MCMC	Perf #1-LM
Initial guess	0.01	0.01
Calculated	0.02104	0.02108
True	0.02107	0.02107
Error (%)	**0.11**	**0.06**

TABLE 4.3—INVERSION RESULTS FOR THE SECOND SET OF PERORATION		
	Perf #2-MCMC	Perf #2-LM
Initial guess	0.01	0.01
Calculated	0.00356	0.00355
True	0.00354	0.00354
Error (%)	**0.50**	**0.22**

With this inversion procedure, not only MCMC and LM methods result in almost the same accuracy but also the computation time for both are not very different. **Figs. 4.7 and 4.8** illustrate a comparison between the convergence rate of MCMC and LM methods for inverting the first and the second parts of the data, respectively. This comparison reveals that MCMC requires more iterations than LM. But since for each iteration in LM, two forward runs are necessary (M+1), the computation time is not very different than the MCMC. Therefore, with this inversion procedure, when only one parameter is being solved at each step, both methods have almost the same performance.

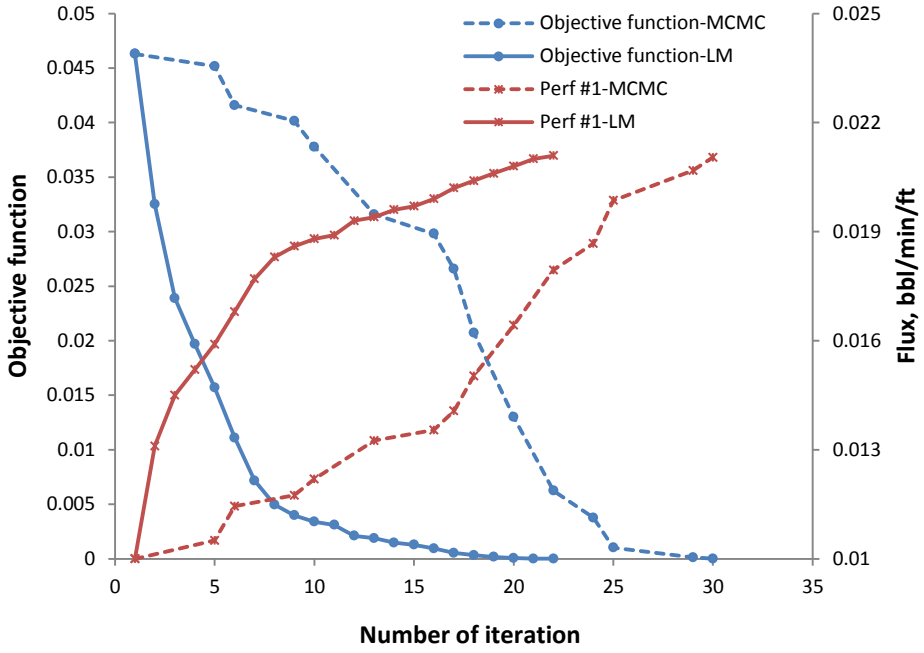

Fig. 4.7—Comparison of the rate of convergence of the objective function and flux for MCMC and LM Methods (inversion of the first part of the data).

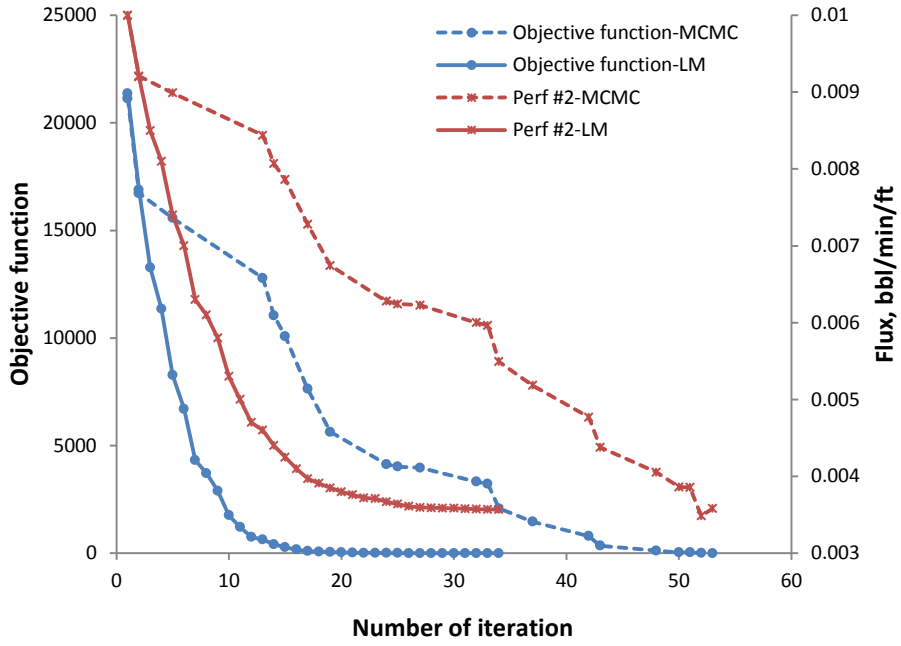

Fig. 4.8—Comparison of the rate of convergence of the objective function and flux for MCMC and LM Methods (inversion of the second part of the data).

This procedure can also be applied to invert the next observed temperature profile. As we can see in **Fig. 4.9**, after 10 minutes of injection acid front passes the first three perforation zones. Therefore, in this case, it is necessary to divide the temperature profile into three parts and invert them sequentially. **Figs. 4.10 through 4.12** show the inverted and observed temperature data for each part of this profile. Again we can see there is a good agreement between the inverted temperature and the observed data.

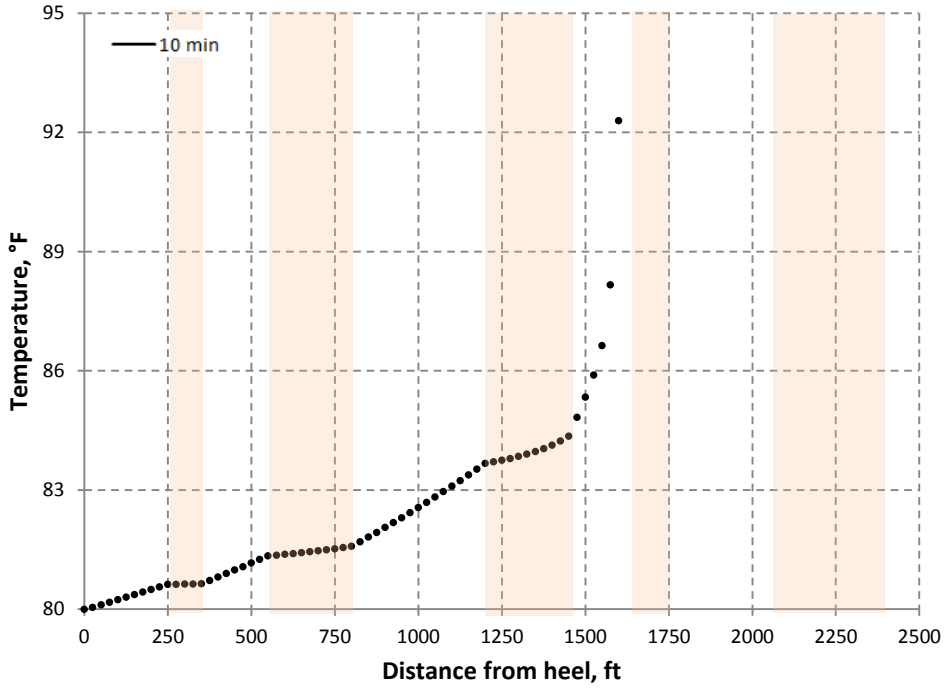

Fig. 4.9—Observed temperature profile after ten minutes of injection.

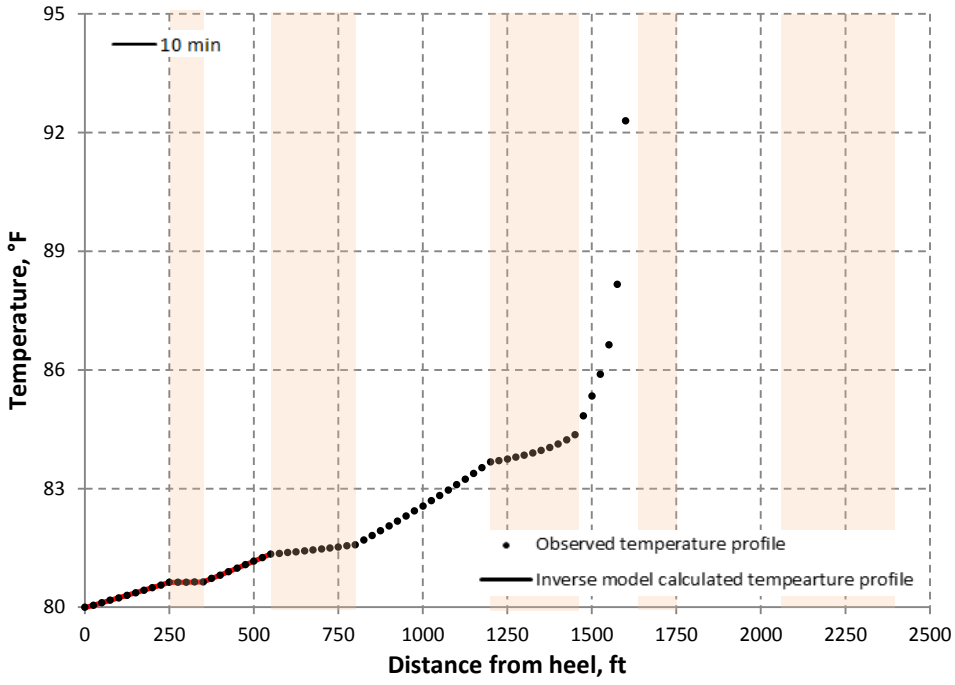

Fig. 4.10—Inverted temperature profile versus observed data (first part of the data).

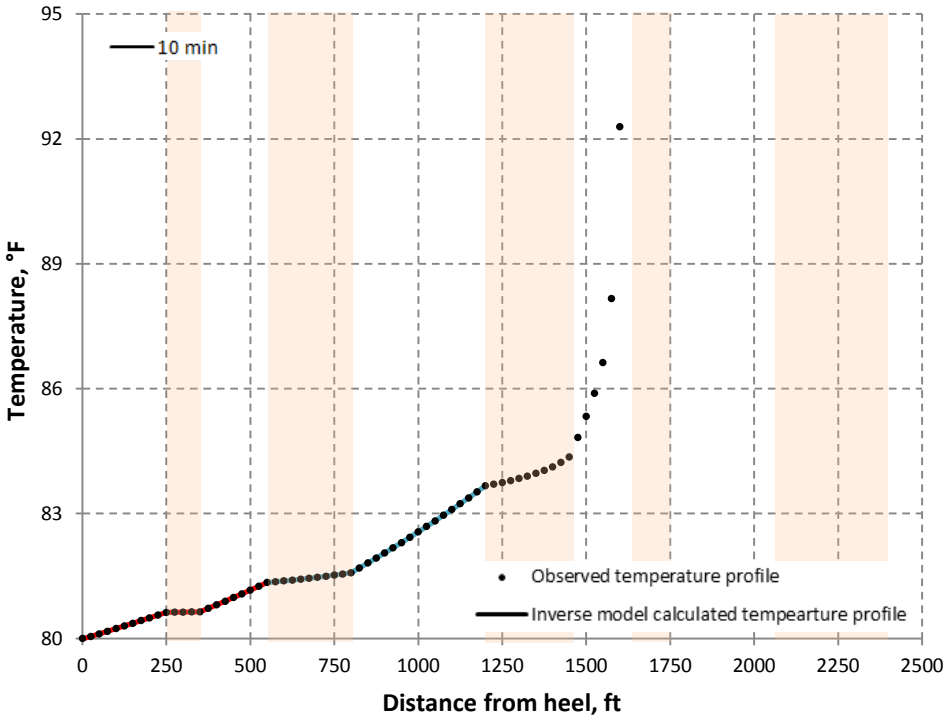

Fig. 4.11—Inverted temperature profile versus observed data (second part of the data).

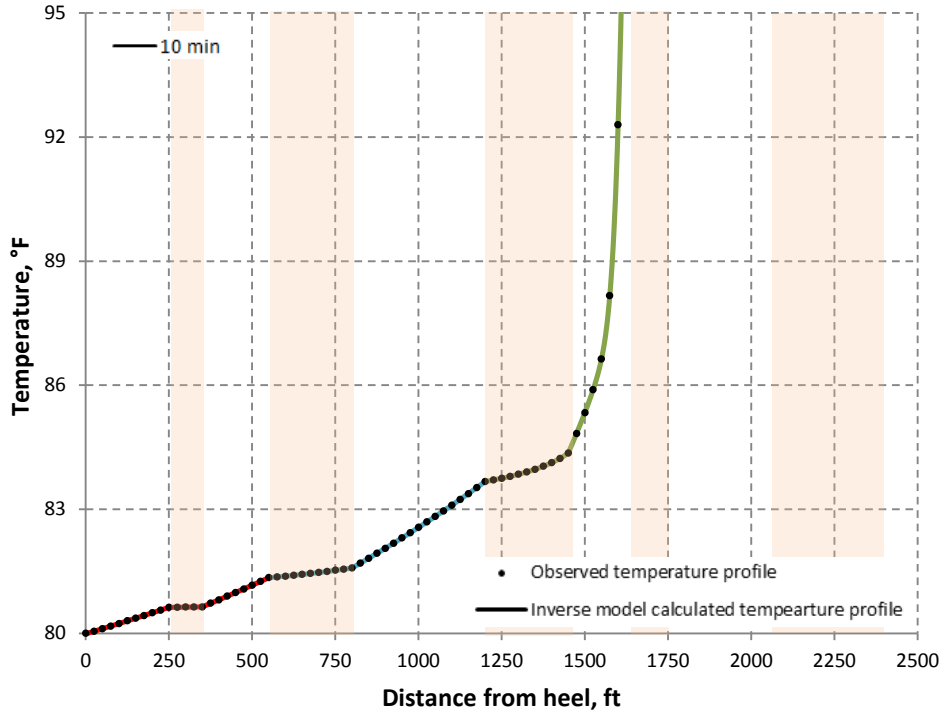

Fig. 4.12—Inverted temperature profile versus observed data (third part of the data).

Note that, to invert the first temperature profile (5 minutes after injection), we did not have any information about the injection profile. Therefore, uniform acid distribution was assumed as the initial guess. But to invert the second temperature profile (10 minutes after injection), we can take advantage of the previously calculated flux of the first two sets of perforations and use them as initial guess. This improves the computation time significantly and reduces the number of iterations to less than 10. **Table 4.4** shows the initial guesses used in this case and the inversion results that are very close to the true values.

TABLE 4.4—INVERSION RESULTS OF THE SECOND TEMPEARTURE PROFILE (10 MINUTES AFTER INJECTION)

	Perf #1	Perf #2	Perf #3
Initial guess	0.02104	0.00356	0.01
Calculated	0.01952	0.00355	0.01745
True	0.01955	0.00354	0.01749
Error (%)	**0.15**	**0.37**	**0.24**

The similar approach can be applied to invert the next four temperature profiles observed during this acid stimulation example. **Table 4.5** summarizes the inversion results of all temperature profiles observed in this example. Comparing inversion results with true values revels that this inversion procedure for interpreting the acid distribution from temperature data is accurate and reliable. Moreover, this procedure is fast and applicable for real-time monitoring of acid stimulation treatment.

TABLE 4.5—INVERSION RESULTS FOR THE ACID STIMULATION OF THE CASED-HOLE EXAMPLE						
		Perf #1	Perf #2	Perf #3	Perf #4	Perf #5
5 min	Initial guess	0.01	0.01			
	Calculated	0.02104	0.00356			
	True	0.02107	0.00354			
	Error (%)	**0.11**	**0.50**			
10 min	Initial guess	0.02104	0.00356	0.01		
	Calculated	0.01952	0.00355	0.01745		
	True	0.01955	0.00354	0.01749		
	Error (%)	**0.15**	**0.37**	**0.24**		
15 min	Initial guess	0.01952	0.00355	0.01745	0.01	0.006
	Calculated	0.01634	0.00387	0.01535	0.01585	0.00659
	True	0.01638	0.00389	0.01531	0.01589	0.00657
	Error (%)	**0.27**	**0.52**	**0.23**	**0.27**	**0.25**
20 min	Initial guess	0.01634	0.00387	0.01535	0.01585	0.00659
	Calculated	0.01463	0.00485	0.01393	0.01457	0.00795
	True	0.01460	0.00483	0.01397	0.01460	0.00793
	Error (%)	**0.18**	**0.37**	**0.25**	**0.22**	**0.21**
25 min	Initial guess	0.01463	0.00485	0.01393	0.01457	0.00795
	Calculated	0.01219	0.00766	0.01169	0.01242	0.00901
	True	0.01215	0.00769	0.01172	0.01238	0.00898
	Error (%)	**0.33**	**0.43**	**0.23**	**0.31**	**0.26**
30 min	Initial guess	0.01219	0.00766	0.01169	0.01242	0.00901
	Calculated	0.01068	0.01023	0.01039	0.01096	0.00894
	True	0.01071	0.01025	0.01036	0.01093	0.00894
	Error (%)	**0.30**	**0.22**	**0.31**	**0.29**	**0.09**

4.5 Discussion of the Practical Application

If inversion is successful in ideal cases, it does not guarantee its success in real cases. Limited data resolution, spatial data density and noise are always associated with any measured data which make the interpretation of real data difficult. Therefore, for any inversion method to be successful for practical applications, it is necessary to analyze the impact of data resolution, spatial data density and noise on the interpretation results. In this section, the required resolution, spatial data density and allowable noise level for temperature data interpretation during acid stimulation treatment are investigated and

quantified. In addition, to improve the quality of the measured temperature data a simple filtering method is introduced.

To study the resolution, data density and noise impact on inversion results, we again use the first acid stimulation example presented in the previous section. The inversion results in this section are compared with the results in the previous section where data was assumed to be ideal.

4.5.1 Sensor Resolution Impact

The inversion results presented in the previous section were obtained by assuming data resolution of 0.001 °F. To investigate the impact of data resolution on temperature data interpretation, we consider two other data resolutions, 0.01 and 0.1 °F. **Figs. 4.13 and 4.14** show the inversion results for these two sensor resolutions. In these figures discrete lines are observed data. Inverted temperature profiles are also shown in these figures with solid lines. As we can see, the inverted temperature profiles are in good agreement with the observed data for resolution of 0.01 °F as well as for resolution of 0.1 °F. The inversion results for this case are given in **Table 4.6** with inversion errors shown in bracket. Changing the data resolution from 0.001 °F to 0.1 °F does not impact the inversion results significantly. The error from inverting the temperature data with resolution of 0.01 °F is still less than 1%. This indicates that improving the data resolution from 0.01 °F to 0.001 °F is not necessary and does not affect the inversion results very much. Changing the data resolution to 0.1 °F slightly impacts the results. When resolution is 0.1 °F the inversion error increases to about 1-4%. This error is still acceptable. However, inversion of the temperature data with resolution of 0.1 °F can lead

to much more error when we add noise to the data; therefore, the resolution of 0.01 °F is recommended for interpretation.

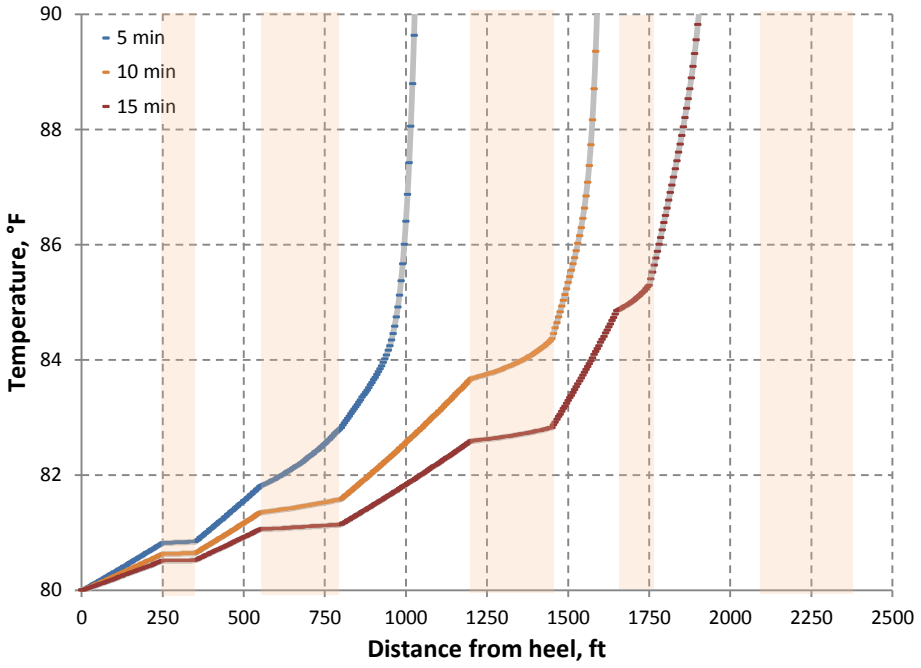

Fig. 4.13—Inverted and observed temperature data with resolution of 0.01 °F.

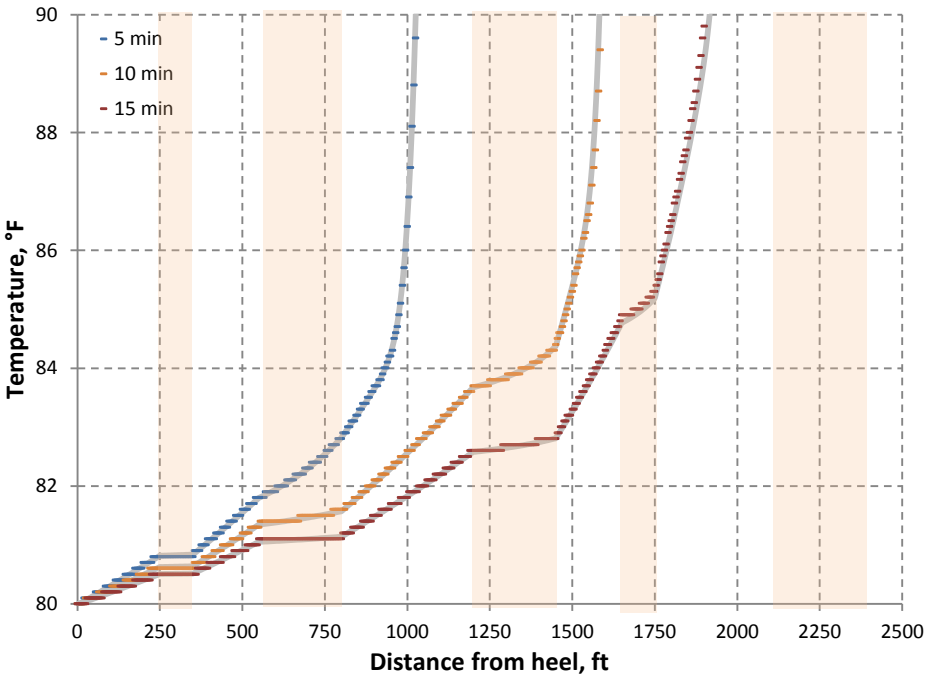

Fig. 4.14—Inverted and observed temperature data with resolution of 0.1 °F.

TABLE 4.6—INVERSION RESULTS OF THE FIRST THREE TEMPEARTURE PROFILES OF THE CASED-HOLE ACID STIMULATION EXAMPLE - RESOLUTION EFFECT						
		Perf #1	Perf #2	Perf #3	Perf #4	Perf #5
5 min	True value	0.02107	0.00354			
	R=0.01	0.02110 (0.16%)	0.00351 (0.80%)			
	R=0.1	0.02119 (0.59%)	0.00361 (1.91%)			
10 min	True value	0.01955	0.00354	0.01749		
	R=0.01	0.01950 (0.25%)	0.00351 (0.76%)	0.01753 (0.22%)		
	R=0.1	0.01968 (0.68%)	0.00362 (2.35%)	0.01757 (0.45%)		
15 min	True value	0.01638	0.00389	0.01531	0.01589	0.00657
	R=0.01	0.01635 (0.21%)	0.00392 (0.77%)	0.01529 (0.16%)	0.01584 (0.33%)	0.00660 (0.38%)
	R=0.1	0.01625 (0.82%)	0.00375 (3.60%)	0.01512 (1.27%)	0.01609 (1.24%)	0.00683 (3.93%)

4.5.2 Spatial Data Density Impact

In the previous section, the spatial density of the observed data was assumed to be 5 ft. This means the distance between two measured data points is 5 ft. To study the impact of the spatial data density on the inversion results, two other spatial densities are considered in this section, 10 and 20 ft. Assuming the sensor resolution of 0.01 °F, **Figs. 4.15 and 4.16** show the inversion results for these two data densities. Again in these figures discrete line represents the observed data and the inverted temperature profile is shown with a solid line. For both spatial data densities, there is a good agreement between the inverted temperature profiles and the observed data. The inversion results are given in **Table 4.7** with inversion errors shown in bracket. As we can see, changing the data density from 5 ft to 20 ft does not impact the inversion results significantly. Inversion error is still in acceptable range. However, if the spatial data density reduces significantly, for example to 50 or 100 ft, then it can affect the inversion results because the small temperature features that help us to interpret the injection distribution cannot be captured effectively by temperature measurements.

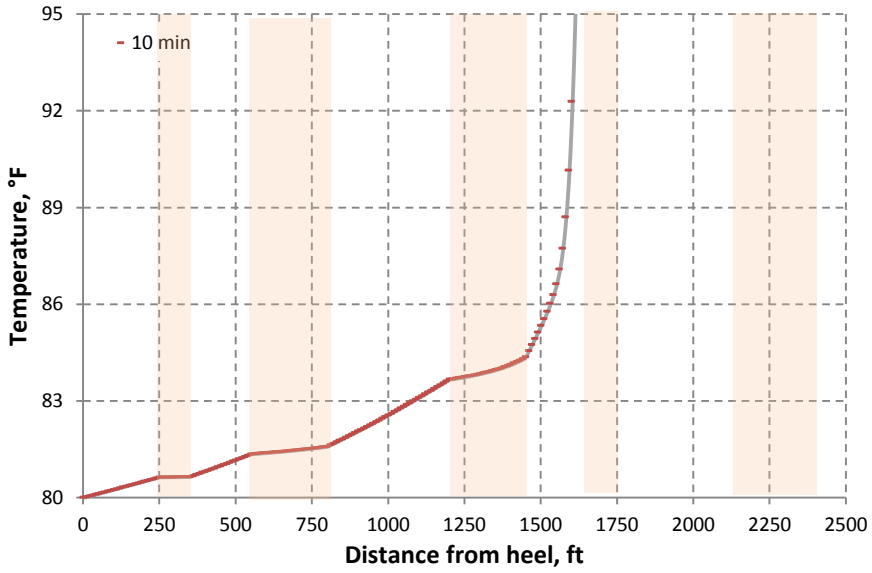

Fig. 4.15—Inverted and observed temperature data with spatial density of 10 ft.

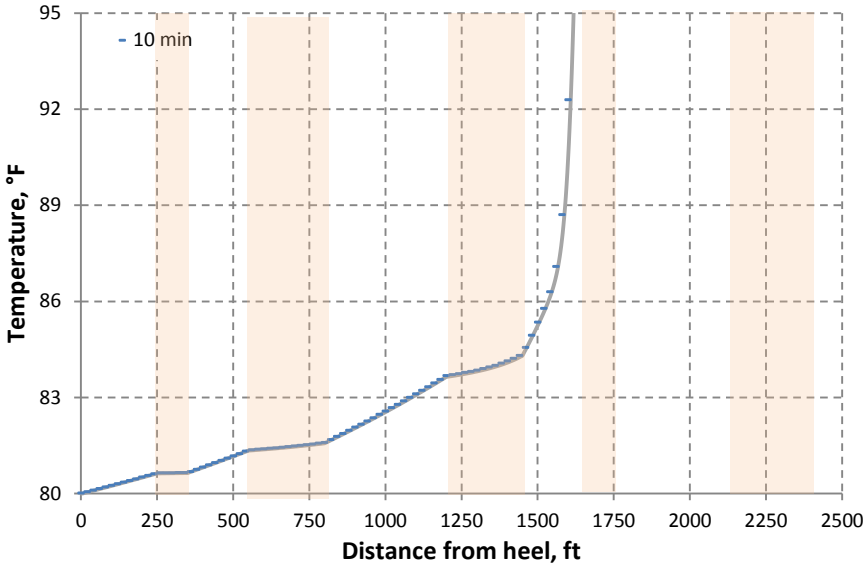

Fig. 4.16—Inverted and observed temperature data with spatial density of 20 ft.

TABLE 4.7—INVERSION RESULTS OF THE CASED-HOLE ACID STIMULATION EXAMPLE – SPATIAL DATA DENSITY EFFECT

		Perf #1	Perf #2	Perf #3
10 min	True value	0.01955	0.00354	0.01749
	S=5	0.01950 (0.25%)	0.00351 (0.76%)	0.01753 (0.22%)
	S=10	0.01971 (0.82%)	0.00359 (0.93%)	0.01762 (0.73%)
	S=20	0.01977 (1.13%)	0.00362 (2.35%)	0.01768 (1.08%)

4.5.3 Noise Impact

Besides the resolution and data density impact, there will almost always be noise or deviation between the true value and the value obtained, due to imperfections of the measuring device. Noise can add difficulty to the interpretation, especially in such a case where the inversion is based on small temperature changes. In this section, to study the impact of noise on temperature data interpretation during acid stimulation treatment, we use data resolution of 0.01 °F with spatial data density of 5 ft, and the noise is assumed to have Gaussian (normal) distribution with a mean value of zero. **Figs. 4.17 through 4.19** show the observed temperature data with three different noise levels, ±0.1 °F (σ=0.033), ±0.2 °F (σ=0.067) and ±0.5 °F (σ=0.167). The inverted temperature profiles are also shown in these figures with a grey line. Meanwhile, the inversion results of these noisy temperature data are summarized in **Table 4.8**. With the noise level of ±0.1 °F (σ=0.033), the inversion results are very close to the true values and the temperature profiles match the observed data well. When the noise level increases to ±0.2 °F (σ=0.067), more error is introduced to the inversion results and the inverted temperature profiles start deviating from the observed data, but the results are still in acceptable range. When the noise level is up to ±0.5 °F (σ=0.167), error in the inversion results goes up to about 5 to 15%. Therefore, we can conclude that the temperature data with noise level of ±0.1 and ±0.2 °F can be used to interpret the acid distribution during treatment, but data with noise level of ±0.5 °F or more will give significant error and lead to the failure of the inversion.

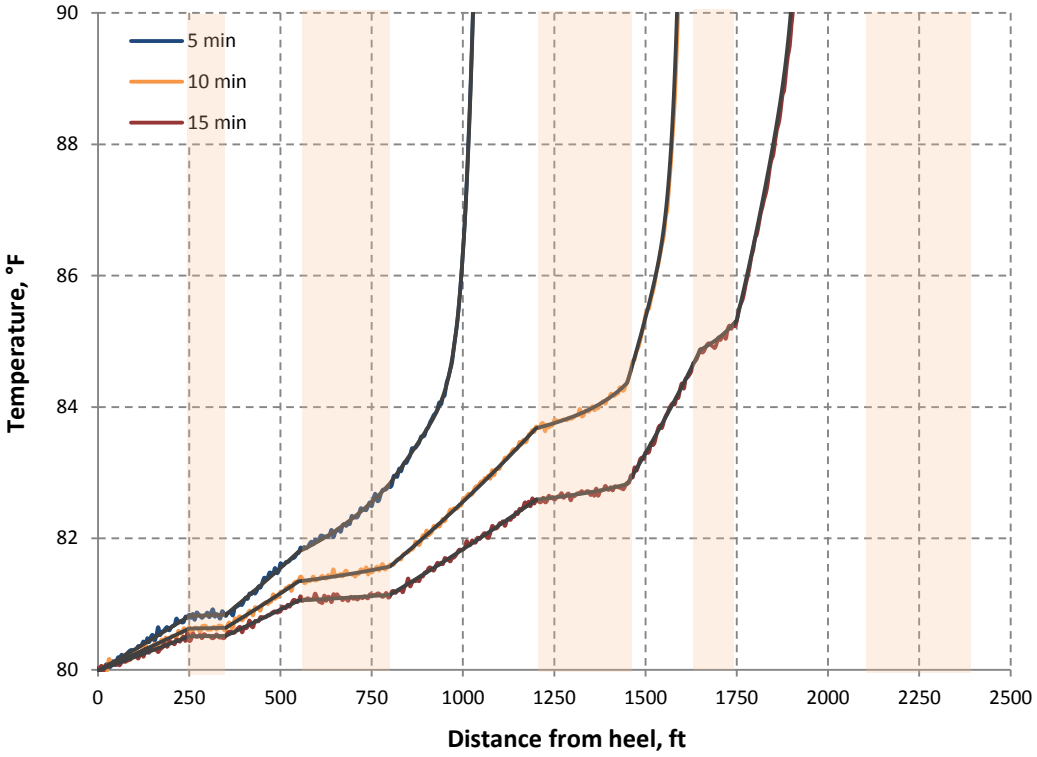

Fig. 4.17—Inverted and observed temperature data with noise level of ±0.1 °F (σ=0.033).

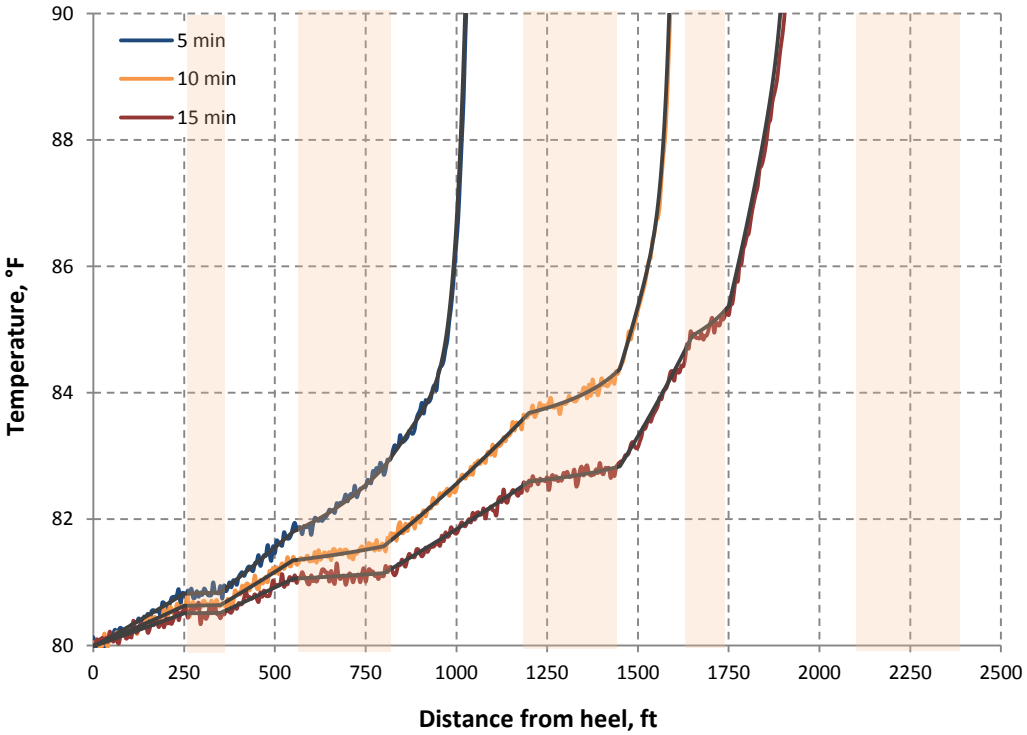

Fig. 4.18—Inverted and observed temperature data with noise level of ±0.2 °F (σ=0.067).

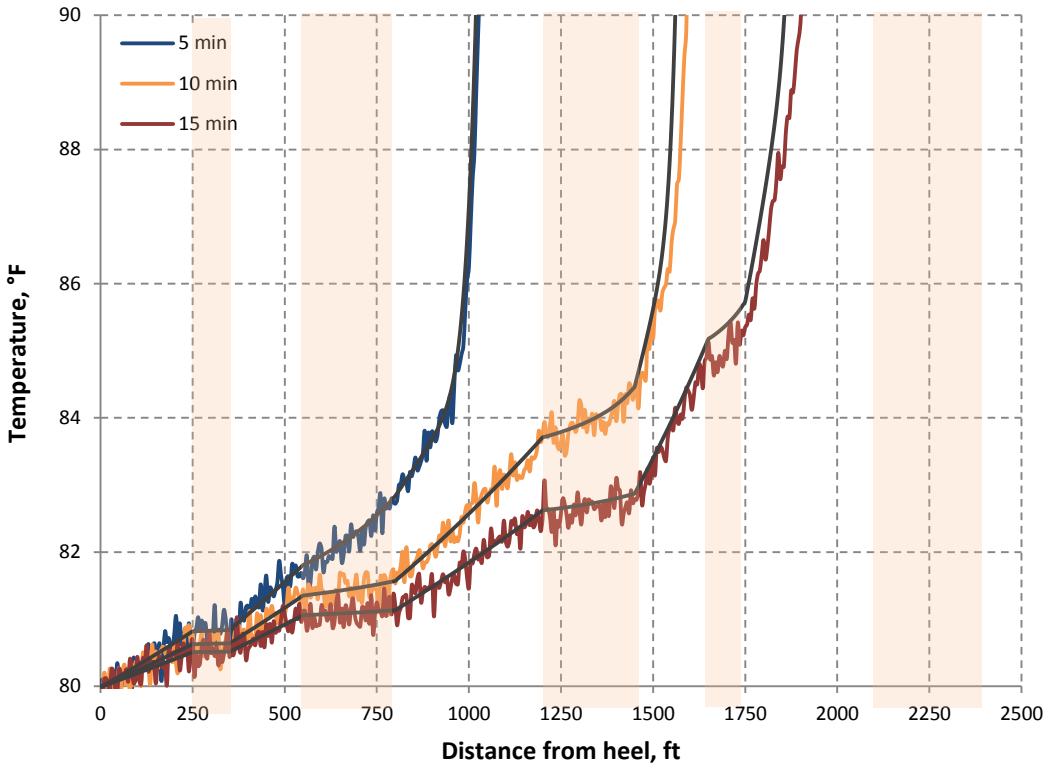

Fig. 4.15—Inverted and observed temperature data with noise level of ±0.5 °F (σ=0.167).

TABLE 4.8—INVERSION RESULTS OF THE FIRST THREE TEMPEARTURE PROFILES OF THE CASED-HOLE ACID STIMULATION EXAMPLE - NOISE EFFECT

		Perf #1	Perf #2	Perf #3	Perf #4	Perf #5
5 min	True value	0.02107	0.00354			
	σ=0. 1	0.02118 (0.54%)	0.00346 (2.33%)			
	σ=0. 2	0.02129 (1.06%)	0.00366 (3.32%)			
	σ=0. 5	0.02176 (3.29%)	0.00369 (4.17%)			
10 min	True value	0.01955	0.00354	0.01749		
	σ=0. 1	0.01968 (0.67%)	0.00363 (2.63%)	0.01734 (0.87%)		
	σ=0. 2	0.01979 (1.23%)	0.00367 (3.76%)	0.01722 (1.55%)		
	σ=0. 5	0.02033 (3.99%)	0.00378 (6.87%)	0.01808 (3.36%)		
15 min	True value	0.01638	0.00389	0.01531	0.01589	0.00657
	σ=0. 1	0.01654 (0.95%)	0.00378 (2.83%)	0.01547 (1.01%)	0.01603 (0.87%)	0.00644 (2.06%)
	σ=0. 2	0.01671 (1.99%)	0.00373 (4.11%)	0.01561 (1.93%)	0.01613 (1.49%)	0.00627 (4.57%)
	σ=0. 5	0.01711 (4.43%)	0.00435 (11.82%)	0.01599 (4.41%)	0.01508 (5.11%)	0.00565 (13.96%)

4.5.4 Improve the Procedure by Data Filtering

As we discussed, noise can affect the inversion results to some extent depending on the noise level. Therefore, it requires a data filtering before analyzing the temperature data when the noise level is high. In this study, we applied a simple moving average filtering method for de-noising and improving the inversion results. Moving average filtering method is a low pass filter which smoothes the data by replacing each data point with the average of the neighboring data points defined within a span, which can be represented by (Sui et al. 2008)

$$y_s(i) = \frac{1}{2n'+1}\left(y(i+n') + y(i+n'-1) + \ldots + y(i-n'+1) + y(i-n')\right) \quad \text{.....(4.20)}$$

where $y_s(i)$ is the smoothed value for the i^{th} data point, n' is the number of neighboring data points on either side of $y_s(i)$, and $2n'+1$ is the span. This averaging method removes the high frequency components present in the signal.

To investigate how data filtering can improve the inversion results, the case in the last section with a noise level of ±0.5 °F (shown in Fig. 4.19) is used here for illustration. Given the span of 11, the moving average filtering process is performed on this noisy data. **Fig. 4.20** compares the ideal data without noise (shown by the colored lines) and the smoothed data from the noise level of ±0.5 °F (shown by gray lines). It can be seen that the smoothed data resulting from the moving average filtering matches the ideal data very well.

After filtering process, inversion can be performed using the filtered data instead of the original data. The inversion results from the smoothed data are given in **Table 4.9**. We can see that the inversion results after filtering are improved significantly. Results are

very close to the true values and errors are down to about 1-4% which is almost in the same range as errors introduced by noise level of ±0.2 °F.

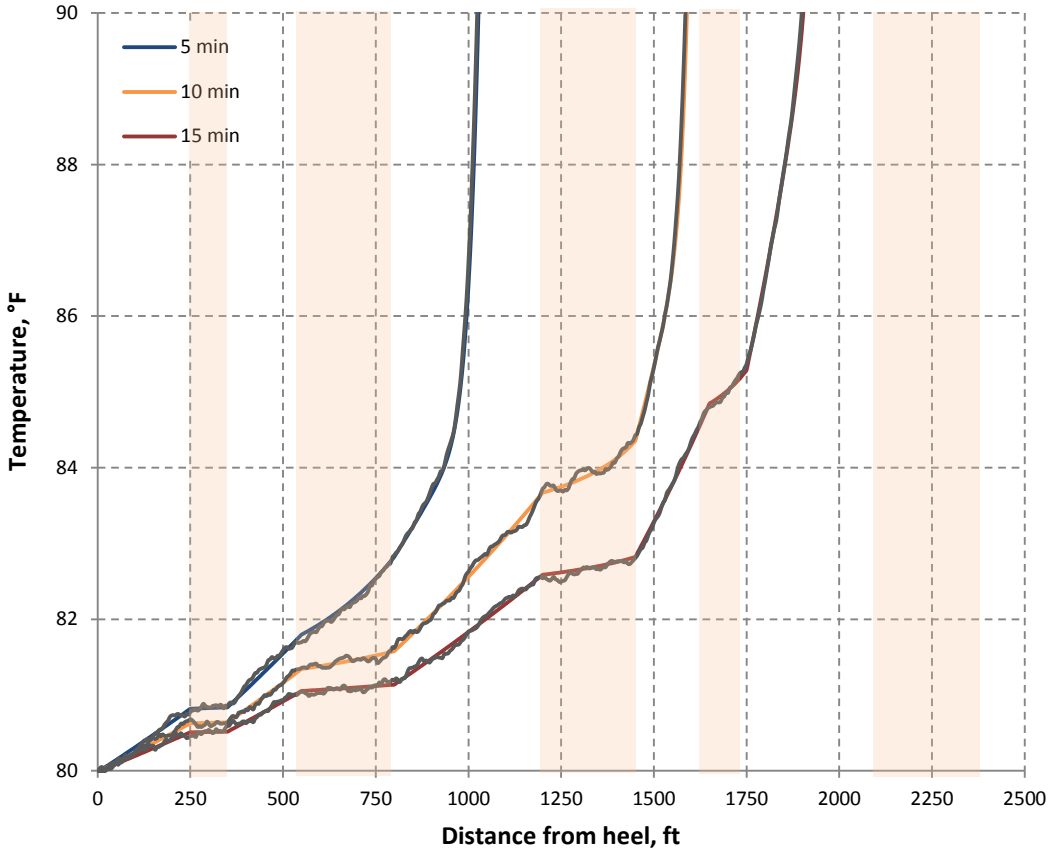

Fig. 4.20—Comparison of the ideal data and smoothed data from the noise level of ±0.5 °F.

TABLE 4.9—COMPARISON OF TRUE VALUES AND INVERSION RESULTS AFTER FILTERING

		Perf #1	Perf #2	Perf #3	Perf #4	Perf #5
5 min	True value	0.02107	0.00354			
	Calculated	0.02089 (0.84%)	0.00363 (2.47%)			
10 min	True value	0.01955	0.00354	0.01749		
	Calculated	0.01975 (1.03%)	0.00361 (2.06%)	0.01765 (0.91%)		
20 min	True value	0.01638	0.00389	0.01531	0.01589	0.00657
	Calculated	0.01660 (1.31%)	0.00378 (2.83%)	0.01555 (1.54%)	0.01609 (1.24%)	0.00633 (3.68%)

In addition to moving average filter, we evaluated other filtering methods such as applying different wavelet transforms available in the MATLAB Toolbox. But in spite of

its simplicity, the moving average filter works better in this case for reducing random noise while retaining the trend of the temperature data. **Fig. 4.21** illustrates a comparison between the distribution of the original noise and remaining noise after applying moving average and Meyer wavelet (shown in **Fig. 4.22**).

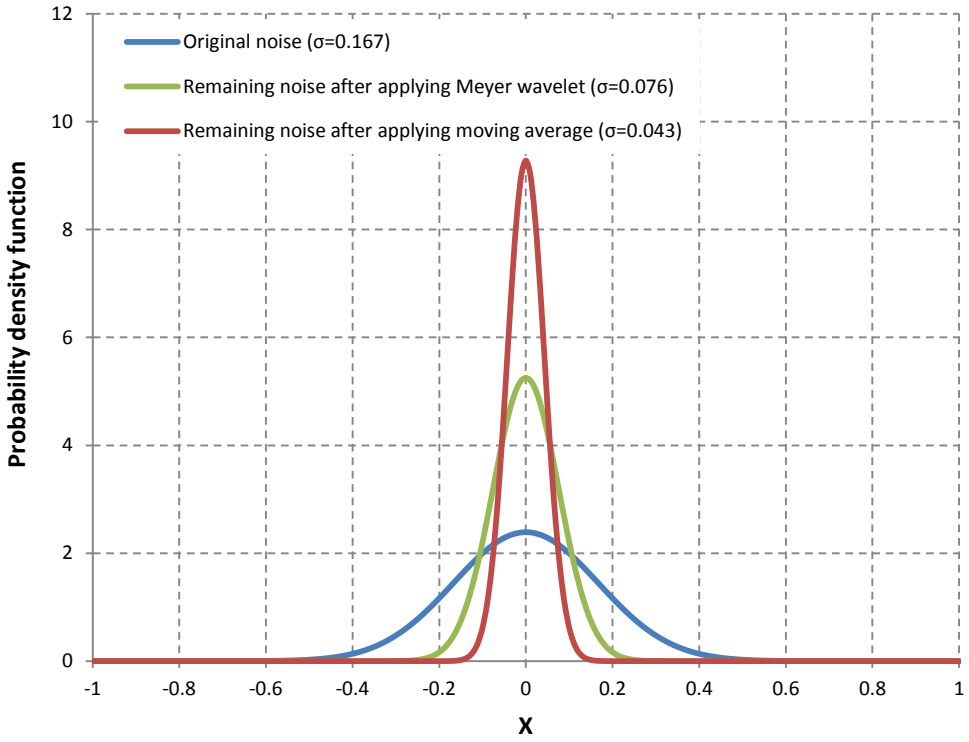

Fig. 4.21—Comparison of the original noise and the remaining noise after filtering by Meyer wavelet and moving average method.

We can observe that the moving average reduce the standard deviation of the original noise more than Meyer wavelet. Moving average reduce it from 0.167 to 0.043, while Meyer wavelet reduce it to 0.076. Moreover, implementing moving average filter is much simpler than wavelet transforms.

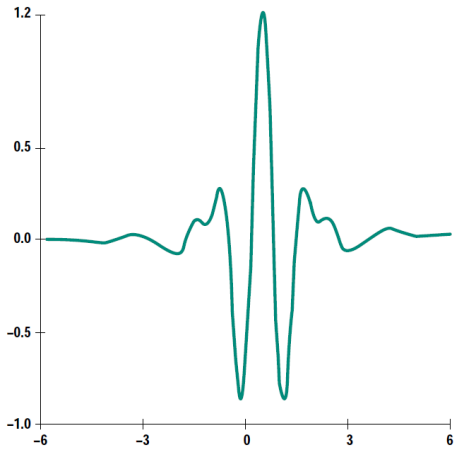

Fig. 4.22—The Meyer wavelet (Mallat, 1998).

This example indicates that data filtering is a crucial step in the temperature data interpretation and when data noise level is in an acceptable range, data filtering can significantly improve the interpretation accuracy. In addition, moving average can be considered as a proper filtering method for de-noising the measured temperature data during acid stimulation treatment and it is recommended based on the results of this study.

5. SKIN EVOLUTION MONITORING

5.1 Introduction

We can now use the knowledge of the acid distribution along the wellbore and extend the real-time monitoring and evaluation of the acid stimulation treatment in horizontal wells to calculate the evolving skin factor as a function of injection time and location along the wellbore. As the skin factor is a reflection of the injectivity, it will indicate directly if the acid stimulation is effective and if diversion is successful.

By monitoring the evolution of the skin factor during the treatment one can ensure that the acidizing treatment is removing the damage from the formation, a sufficient volume of acid is being injected into the formation, and more importantly, the injection is not damaging the formation, which can happen if the treatment is not designed correctly. The effect of the individual fluid stages pumped during the treatment can be evaluated. This information can be used for evaluating the effectiveness of diversion processes as well as optimizing future treatments.

The approach to monitor the evolving skin along the lateral is simple. We can use a proper pressure transient model to calculate skin factor by integrating the inversion results of the temperature data (acid injection profile) with either surface or bottomhole injection pressure. In this section we first discuss the calculation of skin factor from treatment data and then we illustrate the skin evolution monitoring in detail by presenting an example.

5.2 Skin Calculation

To calculate skin factor during treatment a suitable pressure transient model for horizontal wells is required because transient behavior is in effect for a time that greatly exceeds acid injection time and therefore, during the entire treatment we are dealing with transient flow regime in the formation. This type of flow, also known as infinite-acting flow, occurs when the boundary effect is not observed. This flow ends when all the outer boundaries of the reservoir are reached by the propagating pressure disturbance. During this period, the well behaves as if it was placed in a reservoir with infinite size.

The transient flow behavior of horizontal wells was the subject of many studies for many years (Clonts and Ramey 1986; Ozkan and Joshi 1989; Odeh and Babu 1990; Kuchuk et al. 1991). In 1991, Kuchuk et al. presented an analytical solution for transient pressure behavior of a horizontal well completed in an infinite anisotropic medium bounded above and below by horizontal planes (**Fig. 5.1**), using Laplace transform. Their solution is based on the uniform-flux, line-source solution and also averaging the pressure along the length of the well.

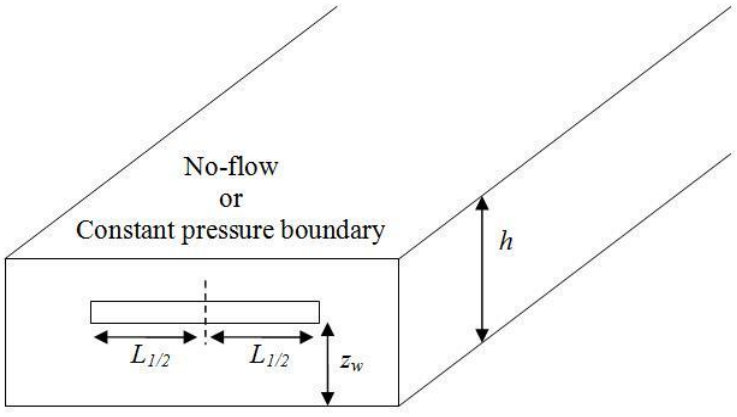

Fig. 5.1—Geometry model used in Kuchuk et al.'s model.

Kuchuk et al. identified four different flow periods during the transient flow of a horizontal well including first radial flow, second radial flow, intermediate-time linear flow and late-time radial flow. They presented specific equations for each of these flow periods as well as equations for determining the length of each period. For the most acid stimulation treatments the pumping time is on the order of hours, and therefore the first radial flow period covers the time period of most acid stimulation treatments.

The first flow pattern for horizontal wells that identified by Kuchuk et al. is actually elliptic-cylindrical. After some time, the elliptic-cylindrical flow period becomes approximately radial. This radial flow around the wellbore may continue until the effect of the nearest boundary is felt at the wellbore. The behavior of this period is equivalent to the behavior of fully penetrating vertical well in an infinite reservoir. The equation for the first radial flow period in oilfield units may be written as

$$q = \frac{2\sqrt{k_H k_V}\, L_{1/2}\left(p_i - p_w\right)}{162.6 B\mu\left[\log\left(\frac{\sqrt{k_H k_V}\, t}{\phi\mu c_t r_w^2}\right) - 3.2275 + 0.8686\, s - 2\log\frac{1}{2}\left(\sqrt[4]{\frac{k_H}{k_V}} + \sqrt[4]{\frac{k_V}{k_H}}\right)\right]} \quad \text{.....(5.1)}$$

where q is the rate (injection or production) and k_H and k_V are the horizontal and vertical permeability, respectively. $L_{1/2}$ is the half-length of the horizontal wellbore and p_i and p_w are the initial reservoir pressure and wellbore pressure, respectively. B is the fluid formation volume factor, μ is fluid viscosity and c_t is the total compressibility. t in this equation is the time of production or injection and s is the skin factor.

The start of the effect of the nearest boundary (no-flow or constant pressure) or the end of this flow period can be determined as

$$t = \frac{\phi\mu c_t}{0.0002637\ \pi k_V}\min\left\{z_w^2, \left(h - z_w\right)^2\right\} \quad \text{.....(5.2)}$$

where h is the reservoir thickness and z_w is the distance of the wellbore from the lower boundary as shown in Fig. 5.1.

For typical values of the parameters for an acid stimulation treatment of k_H=10 md, I_{ani}=0.2, ϕ=0.2, μ=1 cp, c_t=5×10^{-5} psi^{-1}, h=100 ft and z_w=50 ft, the first radial flow period ends after about 15 hours which is in the range of pumping time for most acid stimulation treatments.

Note that if the pumping time is intended to be long, it is required to calculate the length of the first radial flow period to make sure the radial flow assumption is valid during the pumping time, and if it is necessary use the corresponding equation for the second radial flow period which can written as

$$q = \frac{\sqrt{k_H k_V}\, L_{1/2} (p_i - p_w)}{162.6 B\mu \left[\log\left(\frac{\sqrt{k_H k_V}\, t}{\phi \mu c_t r_w^2} \right) - 3.2275 + 0.4343\, s - \log\left[\left(1 + \sqrt{\frac{k_H}{k_V}} \right) \frac{z_w}{r_w} \right] \right]} \quad \text{.....(5.3)}$$

From Eq. 5.1, skin factor can be calculated as

$$s = 1.151 \left[\frac{2\sqrt{k_H k_V}\, L_{1/2}}{162.6 qB\mu} (p_i - p_w) - \log\left(\frac{\sqrt{k_H k_V}\, t}{\phi \mu c_t r_w^2} \right) + 2\log \frac{1}{2}\left(\sqrt[4]{\frac{k_H}{k_V}} + \sqrt[4]{\frac{k_V}{k_H}} \right) + 3.2275 \right] \text{.(5.4)}$$

The above equations are only valid for injection at a constant rate. However, injection rate is hardly constant during an acid stimulation treatment and it varies most of the time throughout the treatment. Applying the principle of superposition (Lee et al. 2003) the transient flow equation of the first radial flow period for multiple rates can be expressed as

$$\frac{p_i - p_w}{q_n} = \frac{162.6B\mu}{2\sqrt{k_H k_V}\,L_{1/2}}\left[\sum_{j=1}^{n}\left(\frac{q_j - q_{j-1}}{q_n}\log(t_n - t_{j-1})\right) + \log\left(\frac{\sqrt{k_H k_V}}{\phi\mu c_t r_w^2}\right) - 2\log\frac{1}{2}\left(\sqrt[4]{\frac{k_H}{k_V}} + \sqrt[4]{\frac{k_V}{k_H}}\right) - 3.2275 + 0.87s\right] \quad \text{.....(5.5)}$$

where n is the number of injection rate changes and q_n is the injection rate during n^{th} time increment.

Consequently, skin factor during an acid stimulation treatment can be calculated as

$$s = 1.151\left[\frac{2\sqrt{k_H k_V}\,L_{1/2}}{162.6B\mu}\left(\frac{p_i - p_w}{q_n}\right) - \sum_{j=1}^{n}\left(\frac{q_j - q_{j-1}}{q_n}\log(t_n - t_{j-1})\right) - \log\left(\frac{\sqrt{k_H k_V}}{\phi\mu c_t r_w^2}\right) + 2\log\frac{1}{2}\left(\sqrt[4]{\frac{k_H}{k_V}} + \sqrt[4]{\frac{k_V}{k_H}}\right) + 3.2275\right] \quad \text{.....(5.6)}$$

We can adopt Hill and Zhu's inverse injectivity method (1996) and rewrite Eq. 5.5 in the following form

$$\frac{p_i - p_w}{q_n} = m\Delta t_{sup} + b \quad \text{.....(5.7)}$$

where m and b are function of reservoir and fluid properties and skin factor. They can be express as

$$m = \frac{162.6B\mu}{2\sqrt{k_H k_V}\,L_{1/2}} \quad \text{.....(5.8)}$$

$$b = m\left(\log\left(\frac{\sqrt{k_H k_V}}{\phi\mu c_t r_w^2}\right) - 2\log\frac{1}{2}\left(\sqrt[4]{\frac{k_H}{k_V}} + \sqrt[4]{\frac{k_V}{k_H}}\right) - 3.2275 + 0.87s\right) \quad \text{.....(5.9)}$$

and Δt_{sup} is the superposition time function which is defined as

$$\Delta t_{sup} = \sum_{j=1}^{n}\left(\frac{q_j - q_{j-1}}{q_n}\log(t_n - t_{j-1})\right) \quad \text{.....(5.10)}$$

Eq. 5.7 suggests that a plot of the inverse injectivity versus the superposition time function is a straight line with slop *m* and intercept *b*, as long as all parameters (notably skin factor) remain constant. We can take advantage of this property and determine the reservoir permeability as well as initial skin factor during an injectivity test prior to acid injection. For example pre-flush data can be used for this purpose since during pre-flush a non-reacting fluid is usually injected into the formation and therefore, skin factor remains constant. The inverse injectivity can be plotted versus the superposition time function during the pre-flush and consequently the reservoir permeability and the initial skin factor can be determined from the calculated *m* and *b*.

During acid injection, the reservoir permeability remains constant. Therefore the calculated reservoir permeability during the pre-flush can be used to determine the evolving skin factor during the acid injection period.

5.3 Skin Evolution Monitoring Example-No Diversion

In this section we set an example to illustrate how we can determine the local reservoir permeability, initial skin factor as well as skin evolution during treatment. In this example we assume the same wellbore and completion configurations as the example presented in Section 3. Previously it was presumed that reservoir is homogenous, but in this section we assume the formation is heterogeneous along the lateral. Therefore, each zone is considered to have different permeability and different initial skin factor. Consequently, the injectivity of each zone will be different and therefore, each will show a different skin evolution during treatment.

The treatment is assumed to be 50 minutes, which includes pre-flush for 20 minutes followed by 30 minutes of acid injection. The pumping schedule is shown in **Fig. 5.2**. During pre-flush, we simplify the pumping schedule to a step-rate injection as we will be able to plot the inverse injectivity versus superposition time function and determine the reservoir permeability and initial skin factor associated with each zone.

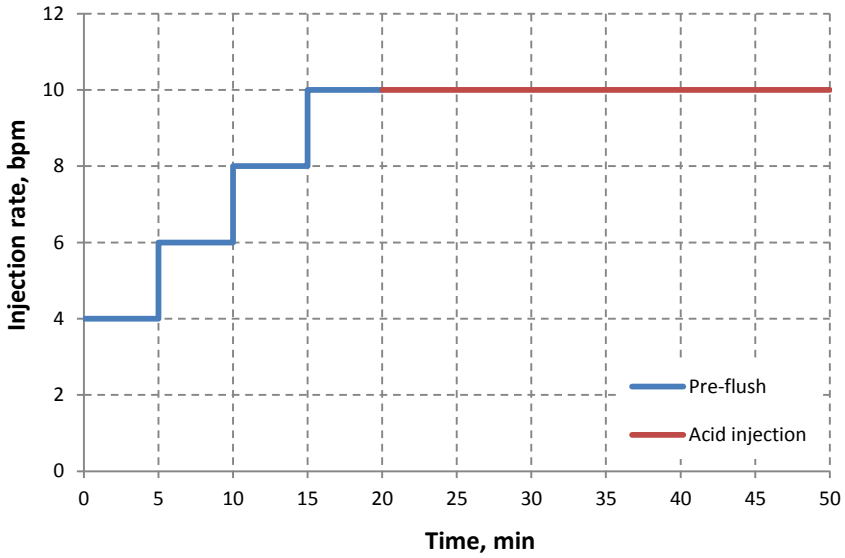

Fig. 5.2—Pumping schedule during this treatment.

Considering the wellbore configuration, the injection rate history, the fluid and formation properties presented in Table 3.1 and 3.2, the results of this treatment can be simulated using a horizontal well matrix acidizing simulator. **Figs. 5.3 and 5.4** illustrate the variation of the fluid flux in each zone and the bottomhole pressure history, respectively. Pressure is measured at the heel of the lateral and it is assumed that the pressure drop is negligible along the lateral.

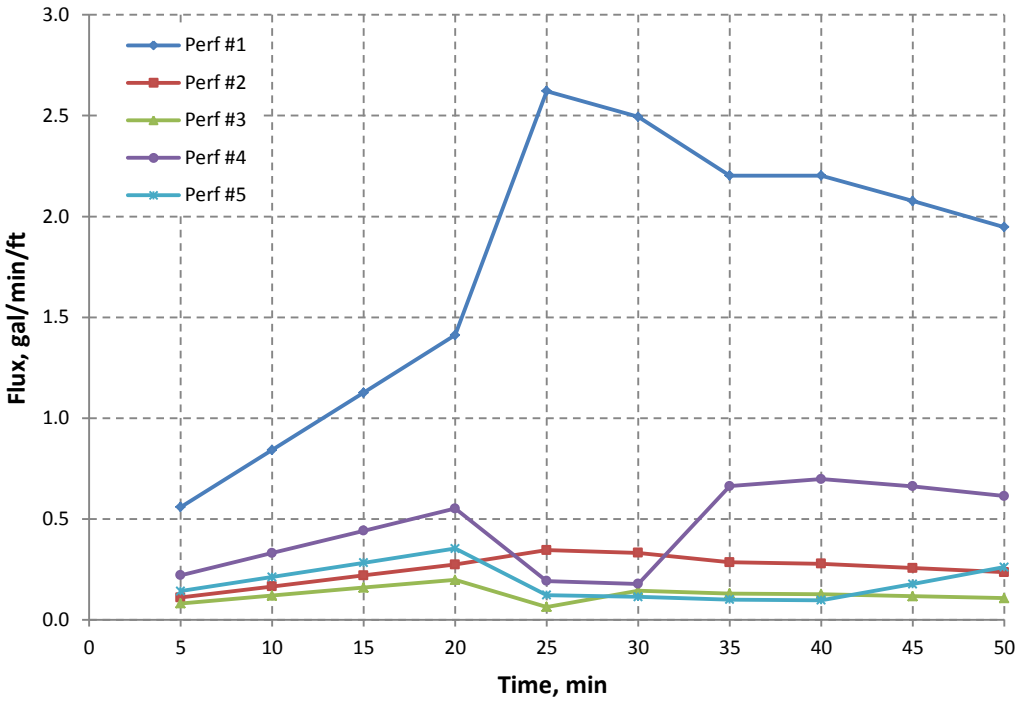

Fig. 5.3—Simulated fluid fluxes during this treatment.

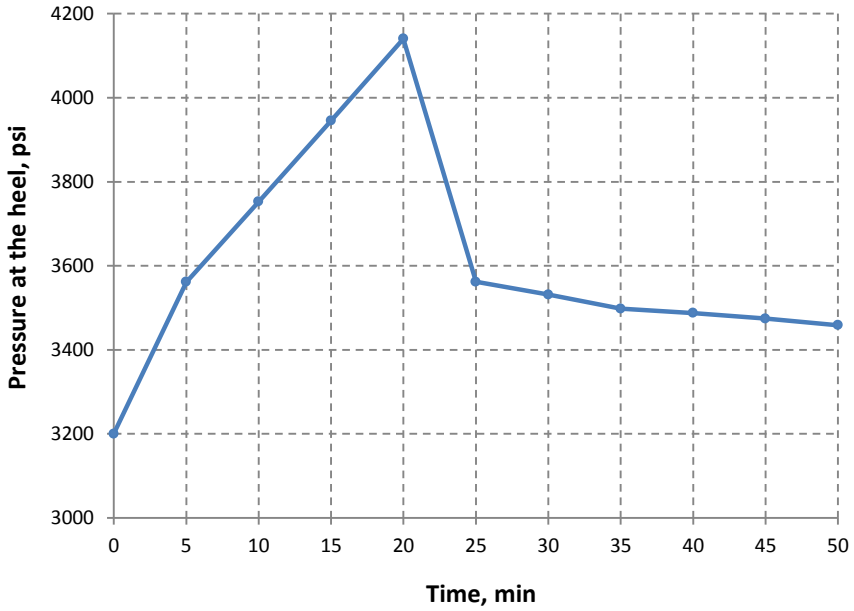

Fig. 5.4—Simulated bottomhole pressure during this treatment.

Using the simulated fluid flux (Fig. 5.2), temperature behavior during this treatment can be simulated by the forward model. Assuming that the DTS resolution is 0.01 °F and the noise level is ±0.5 °F (σ=0.167), the simulated temperature data is shown in **Fig. 5.5**. In this section, we consider the simulated temperature data as observed data for the purpose of illustration. The injection profile is interpreted from the observed temperature data every five minutes.

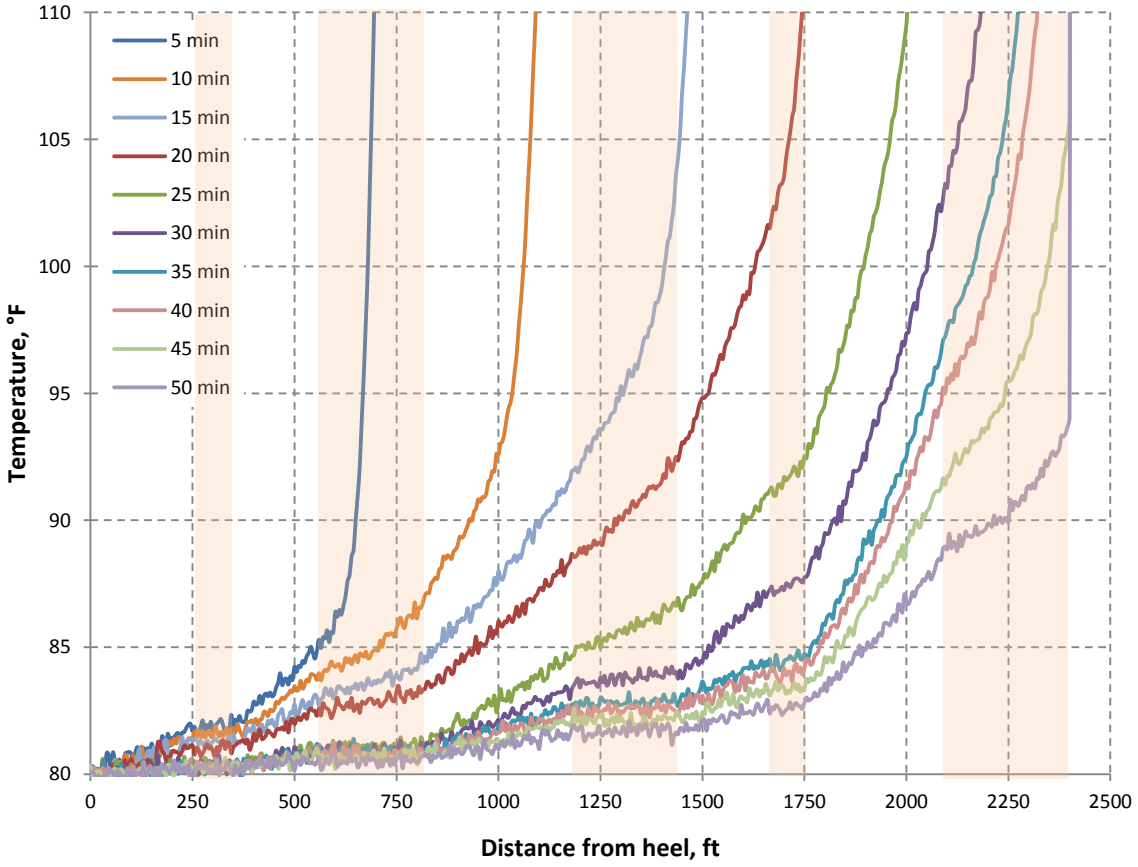

Fig. 5.5—Simulated wellbore temperature behavior during this treatment.

Following briefly illustrates the steps required for real-time skin evolution monitoring of this treatment using pressure and temperature data.

5.3.1 Data Filtering

As previously discussed, it is first required to filter and de-noise the temperature data in order to achieve reliable inversion results. Thus, moving average filtering method is applied to filter the data.

5.3.2 Injection Distribution Determination

The proposed inversion procedure in the last section can be applied to the smoothed temperature data to determine the injection profile every five minutes. **Fig. 5.6** shows the inverted temperature profiles versus the smoothed temperature data, while **Table 5.1** summarizes the inversion results which are in terms of fluid flux with unit of bbl/min/ft.

As we see from Fig. 5.6, temperature data does not provide us with any information about the fluid flux in the third zone until we obtain the third temperature profile (15 minutes) and the fourth and fifth zones until we obtain the fourth temperature profile (20 minutes). However, the fluid flux in these zones for the missing periods can be estimated by determining the flux in later times (for example 15 or 20 minutes after injection) and assuming the injectivity of each zone does not change during the pre-flush. The estimated fluid fluxes are indicated in bracket in Table 5.1.

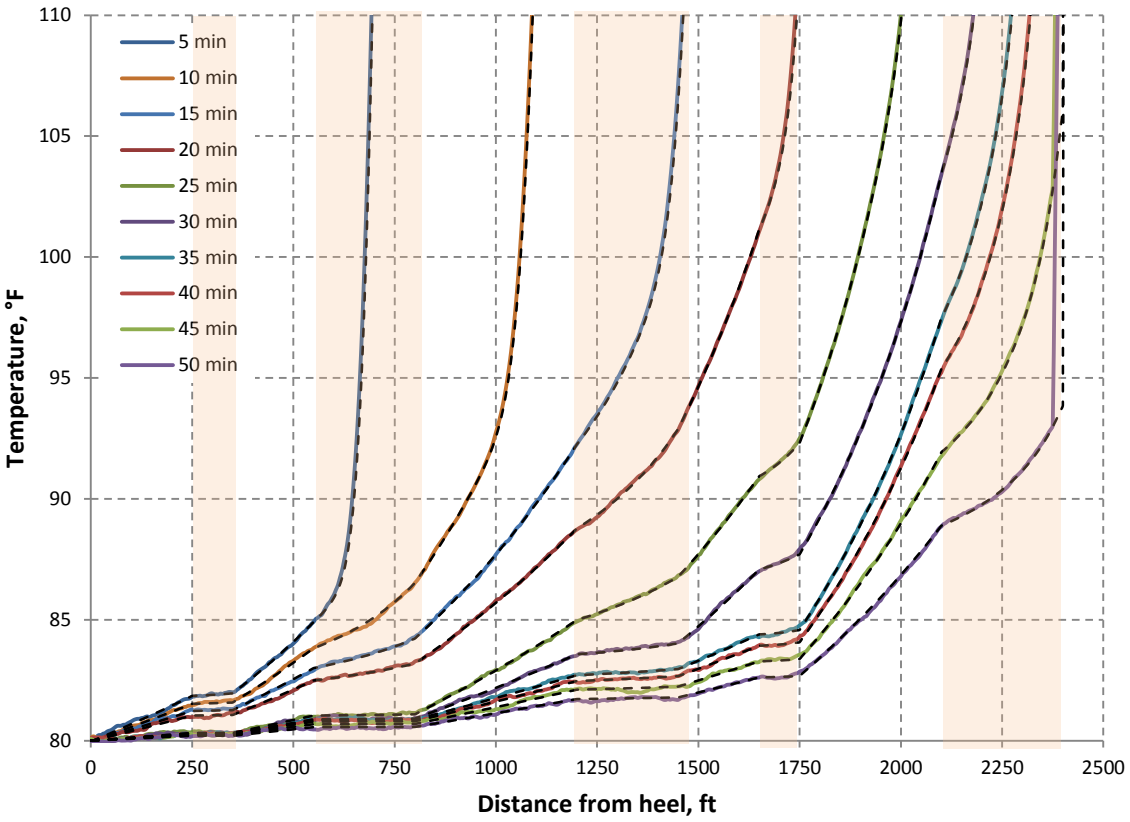

Fig. 5.6—Inverted temperature profiles versus the smoothed temperature data.

TABLE 5.1—INVERSION RESULTS FOR THIS CASE

Time, min	Perf #1	Perf #2	Perf #3	Perf #4	Perf #5
5	0.0133	0.0026	(0.0019)	(0.0052)	(0.0034)
10	0.0200	0.0039	(0.0028)	(0.0077)	(0.0050)
15	0.0267	0.0052	0.0038	(0.0105)	(0.0067)
20	0.0332	0.0065	0.0047	0.0131	0.0084
25	0.0624	0.0082	0.0015	0.0046	0.0029
30	0.0594	0.0079	0.0034	0.0042	0.0027
35	0.0522	0.0068	0.0031	0.0158	0.0024
40	0.0524	0.0066	0.0030	0.0166	0.0023
45	0.0494	0.0061	0.0028	0.0158	0.0042
50	0.0464	0.0056	0.0025	0.0146	0.0062

5.3.3 Reservoir Permeability and Initial Skin Factor Determination

At this step, we can plot the inverse injectivity versus superposition time during the pre-flush since we have all the information that is required for this purpose including the reservoir pressure, the wellbore pressure history and the fluid flux associated with each zone. **Figs. 5.7 through 5.11** illustrate the plot of inverse injectivity versus superposition time function for each zone during the pre-flush. As we expected, plotting inverse injectivity versus superposition time function yields a straight line. The slop and the intercept of each plot are given in table 5.2. Eq. 5.8 and 5.9 can be used to calculate the reservoir permeability and initial skin factor associated with each zone from the corresponding slop and the intercept, respectively. The results of this calculation are summarized in Table 5.3, while Table 5.4 gives the assumed fluid and formation properties used in this section to calculate permeability and skin factor. As we can see, the first zone has higher permeability than the others. This permeability contrast can significantly affect the stimulation results by causing more fluid to be injected into this zone and prevent the others to take sufficient acid. In the next step, we can monitor the skin evolution to evaluate the treatment results.

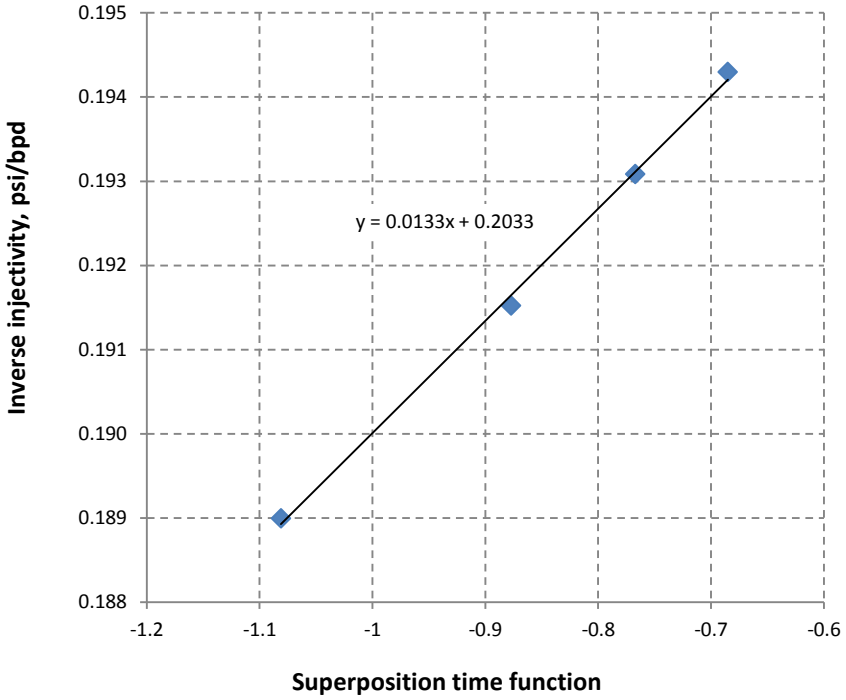

Fig. 5.7—Inverse injectivity versus superposition time function plot for the first zone.

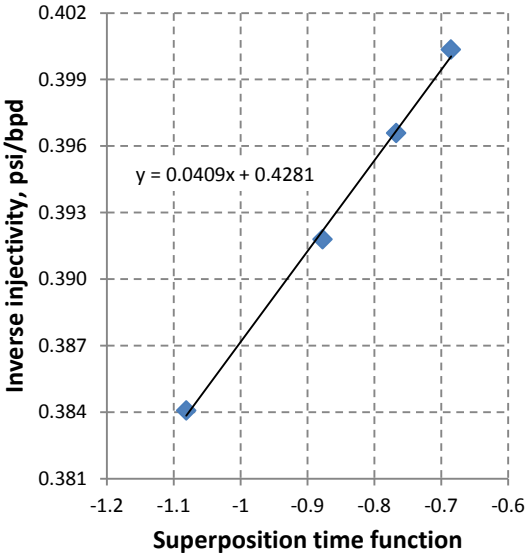

Fig. 5.8—Inverse injectivity versus superposition time function plot for the second zone.

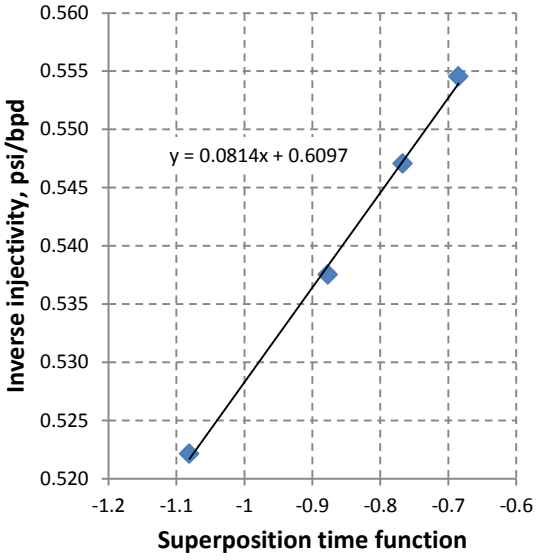

Fig. 5.9—Inverse injectivity versus superposition time function plot for the third zone.

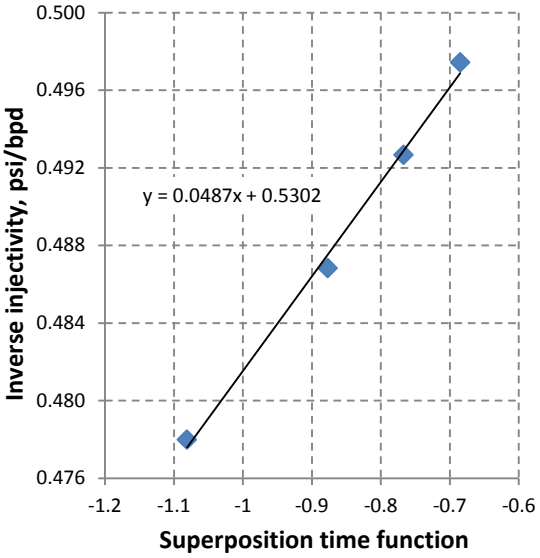

Fig. 5.10—Inverse injectivity versus superposition time function plot for the fourth zone.

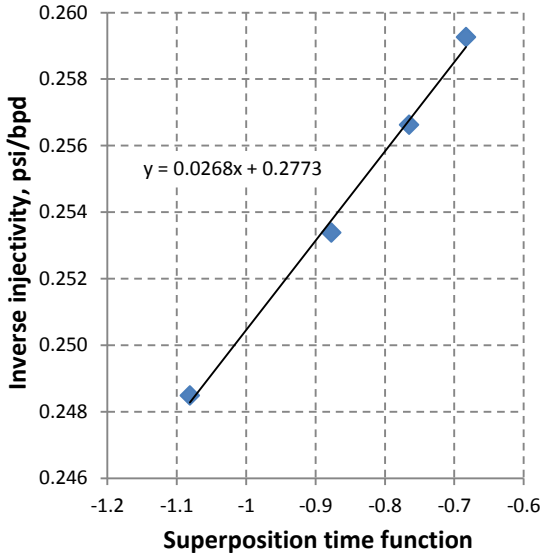

Fig. 5.11—Inverse injectivity versus superposition time function plot for the fifth zone.

TABLE 5.2—SLOP AND INTERCEPT OF INVERSE INJECTIVITY VERSUS SUPERPOSITION TIME FUNCTION PLOT FOR EACH ZONE

	Perf #1	Perf #2	Perf #3	Perf #4	Perf #5
m	0.0133	0.0409	0.0814	0.0487	0.0268
b	0.2033	0.4281	0.6097	0.5302	0.2773

TABLE 5.3—CALCULATED RESERVOIR PERMEABILITY AND INITIAL SKIN FACTOR ASSOCIATED WITH EACH ZONE

	Perf #1	Perf #2	Perf #3	Perf #4	Perf #5
Permeability (k)	61	8	4	17	10
Initial skin factor (s_i)	10.6	6.1	3.0	6.2	5.8

TABLE 5.4—PARAMETERS USED TO CALCULATE PERMEABILITY AND SKIN FACTOR

Reservoir pressure (p_e)	3200	psi
Formation volume factor (B)	1	rb/stb
Formation fluid viscosity (μ)	0.5	cp
Total compressibility (c_t)	5×10^{-6}	psi^{-1}
Porosity (ϕ)	0.2	fraction
Wellbore radius (r_w)	0.25	ft
Anisotropy (I_{ani})	1	fraction

5.3.4 Evolving Skin Calculation

At this step, all the information required to calculate the evolving skin factor during the acid injection period is determined including the pressure and rate history and the permeabilities of each zone. Eq. 5.6 can be used to calculate the skin factor as a function of injection volume (time) in each zone.

Figures 5.12, 14, 16, 18 and 20 shows the pressure and the injection rate history associated with each zone, while **Figs. 5.13, 15, 17, 19 and 21** show the resultant skin evolution during the acid injection period. **Table 5.5** also summarizes the calculated skin factor for each zone. As we can see, real-time monitoring of skin change can assist us to identify zones that are being over treated or under treated. For example, in this case the first and second zones are being over treated because after a while their skin factors do not change in spite of injecting a lot of acid into these zones. While, the other zones specially the fifth one, need further stimulation. Acid reached these two zones later than others and the skin evolution plot suggest that they required more stimulation and their skin factors can be reduced further if more acid is injected into these zones.

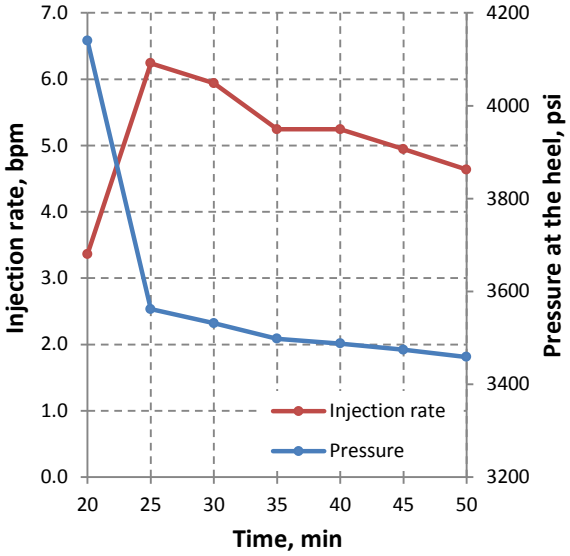

Fig. 5.12—Pressure and injection rate history of the first zone.

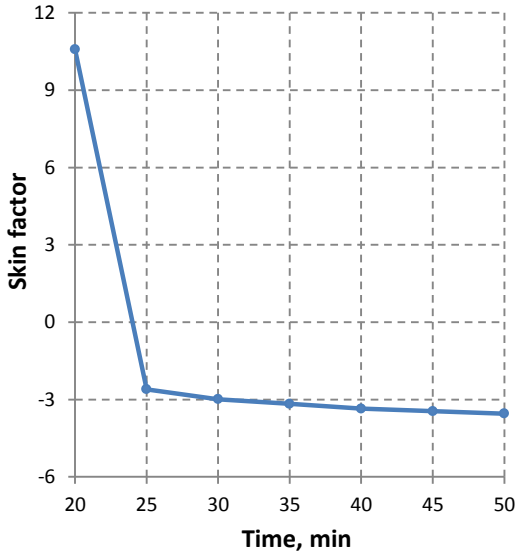

Fig. 5.13—Skin evolution of the first zone.

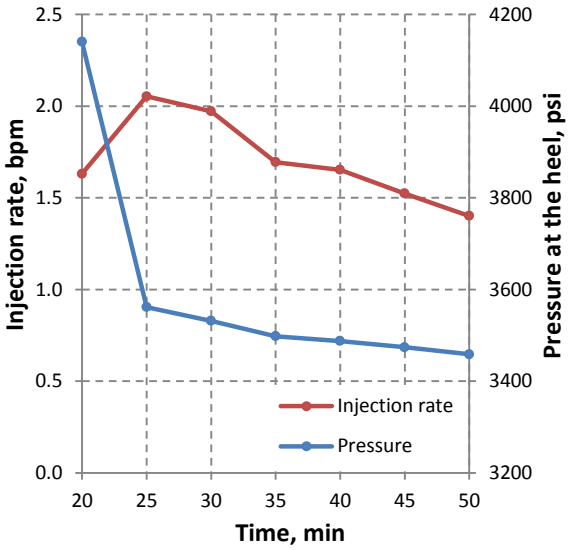

Fig. 5.14—Pressure and injection rate history of the second zone.

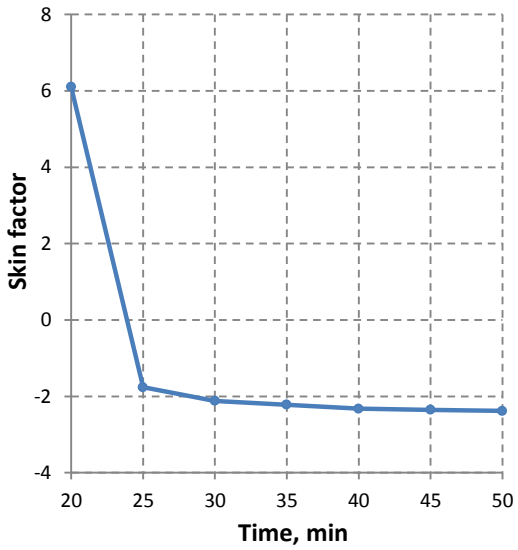

Fig. 5.15—Skin evolution of the second zone.

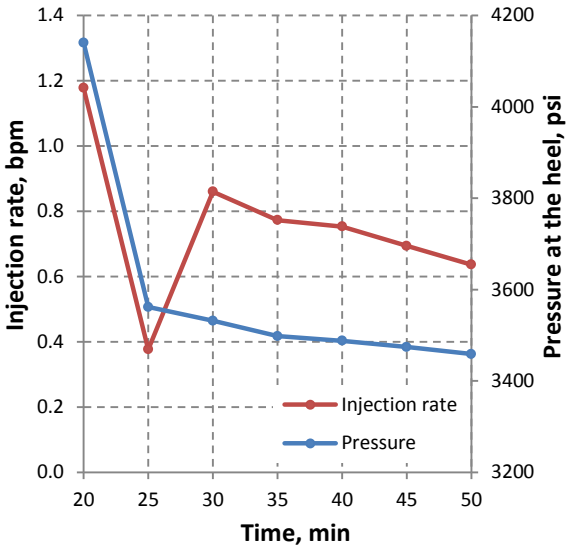

Fig. 5.16—Pressure and injection rate history of the third zone.

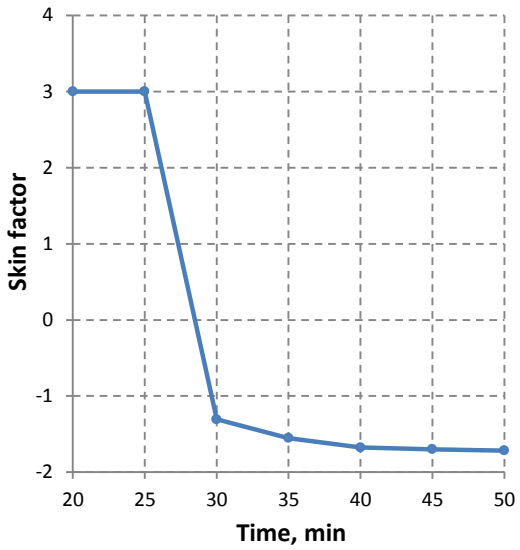

Fig. 5.17—Skin evolution of the third zone.

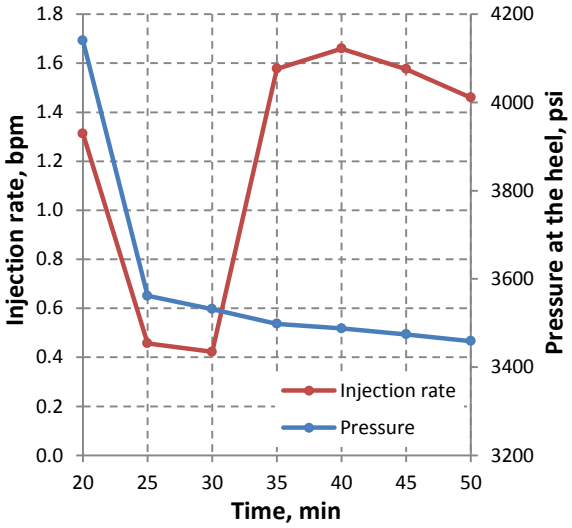

Fig. 5.18—Pressure and injection rate history of the fourth zone.

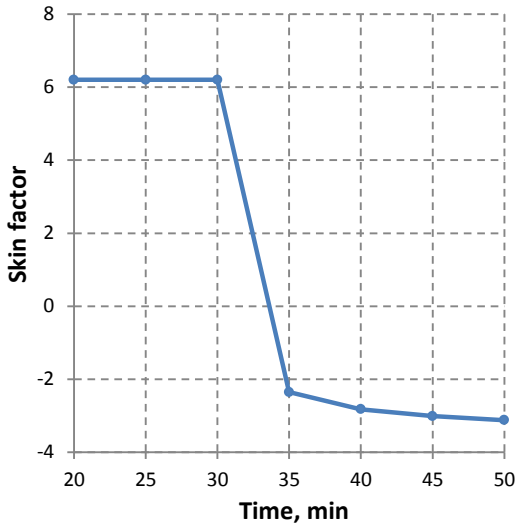

Fig. 5.19—Skin evolution of the fourth zone.

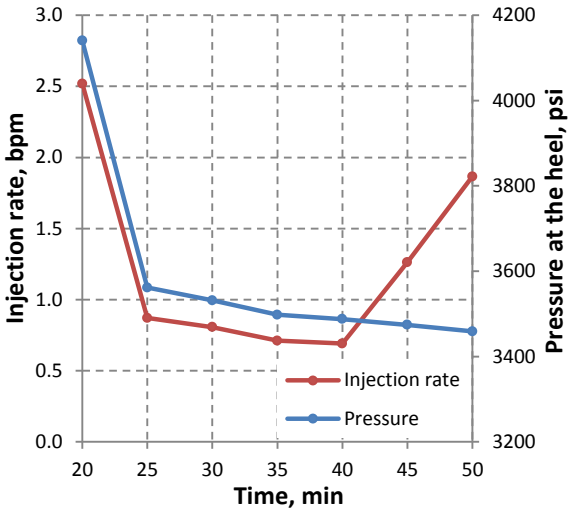

Fig. 5.20—Pressure and injection rate history of the fifth zone.

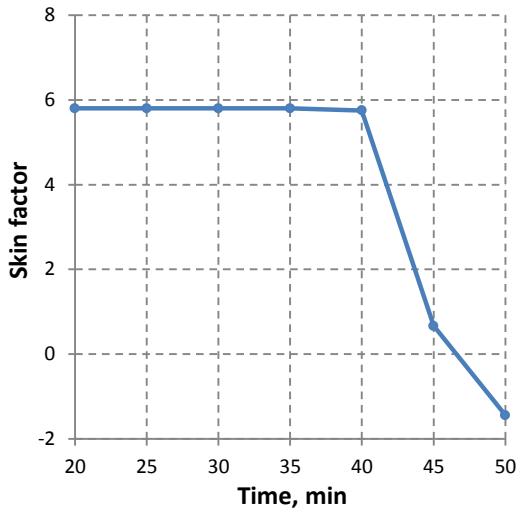

Fig. 5.21—Skin evolution of the fifth zone.

TABLE 5.5—SUMMARY OF THE SKIN EVOLUTION DURING THIS TREATMENT

Time, min	Perf #1	Perf #2	Perf #3	Perf #4	Perf #5
20	10.6	6.1	3.0	6.2	5.8
25	-2.6	-1.8	3.0	6.2	5.8
30	-3.0	-2.1	-1.3	6.2	5.8
35	-3.2	-2.2	-1.6	-2.4	5.8
40	-3.4	-2.3	-1.7	-2.8	5.8
45	-3.5	-2.4	-1.7	-3.0	0.7
50	-3.5	-2.4	-1.7	-3.1	-1.4

5.4 Skin Evolution Monitoring Example-Diversion

In previous example it was assumed that no diversion was used and from the real-time skin monitoring we observed that some zones were being over treated while others needed more stimulation. In this situation, to optimize the treatment, diversion can be applied to divert acid from the over treated zones to others. To illustrate how the effectiveness of diversion can be monitored with this method, in this example we assume that in the middle of the acid injection period, 15 minutes after acid injection, 10 bbl of

non-reacting viscos fluid is added as diverter with viscosity of 100 cp. **Fig. 5.22** shows the pumping schedule for this example.

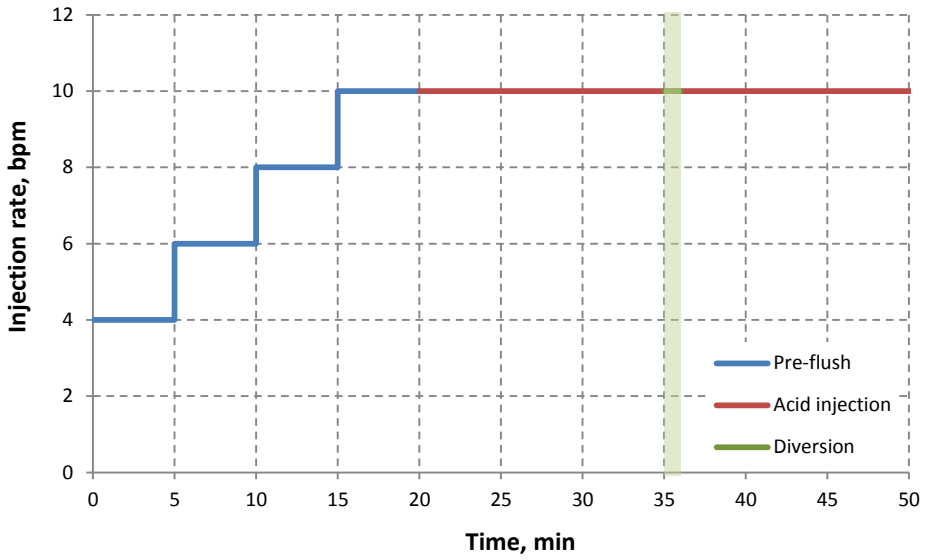

Fig. 5.22—Pumping schedule during this treatment.

The simulated fluid flux and pressure history during the acid injection period for this case are shown in **Fig. 5.23 and 5.24**, respectively. As we can see, before applying diversion (35 minutes after the start of the injection or 15 minutes after the start of the acid injection) everything is exactly the same as the previous example, but when we apply diversion the flux variation and the pressure response is different. Diversion causes an immediate increase in the skin factor of the first zone which is the zone that takes most of the fluid. Consequently, pressure jumps due to increase in overall skin factor and also the fluid distribution changes due to diverting the fluid from the first zone to the others.

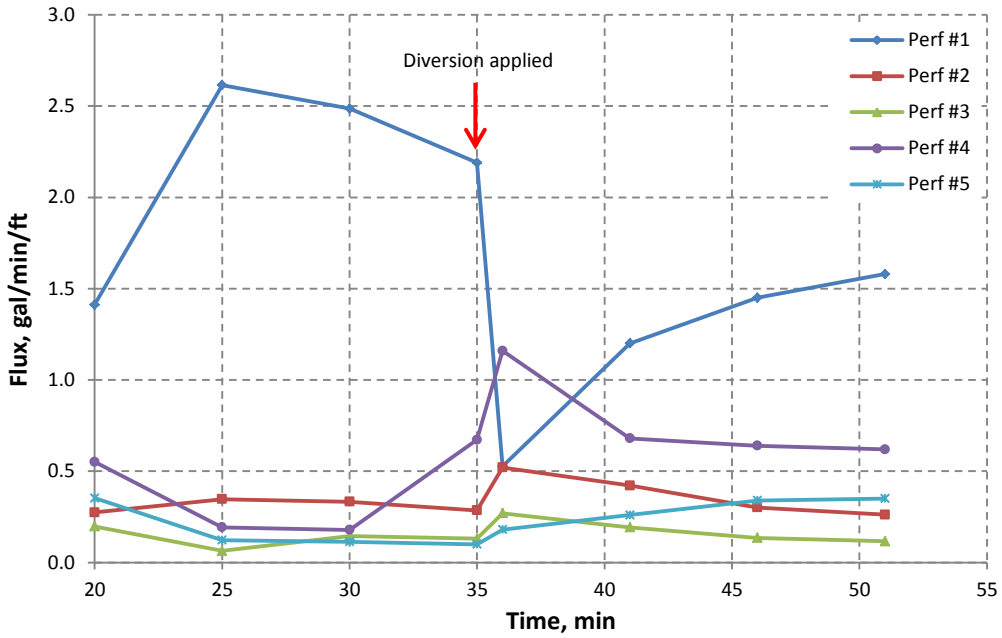

Fig. 5.23—Simulated fluid fluxes during the acid injection period.

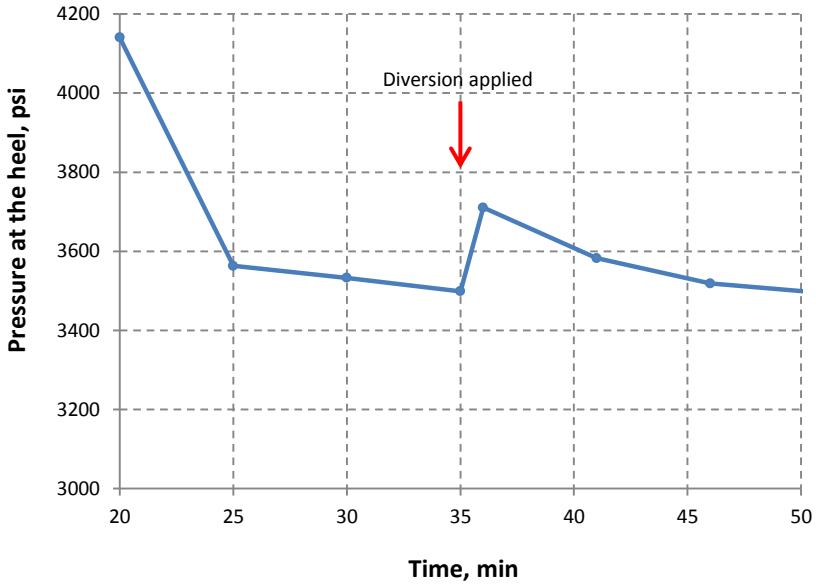

Fig. 5.24—Simulated bottomhole pressure during the acid injection period.

Considering the simulated treatment results, the wellbore temperature behavior right before and after applying diversion is shown in **Fig. 5.25**. Compare to the pervious

example, we can observe more cooling along the fifth zone in this case since the diversion causes the fluid to divert from the first zone to the fifth one.

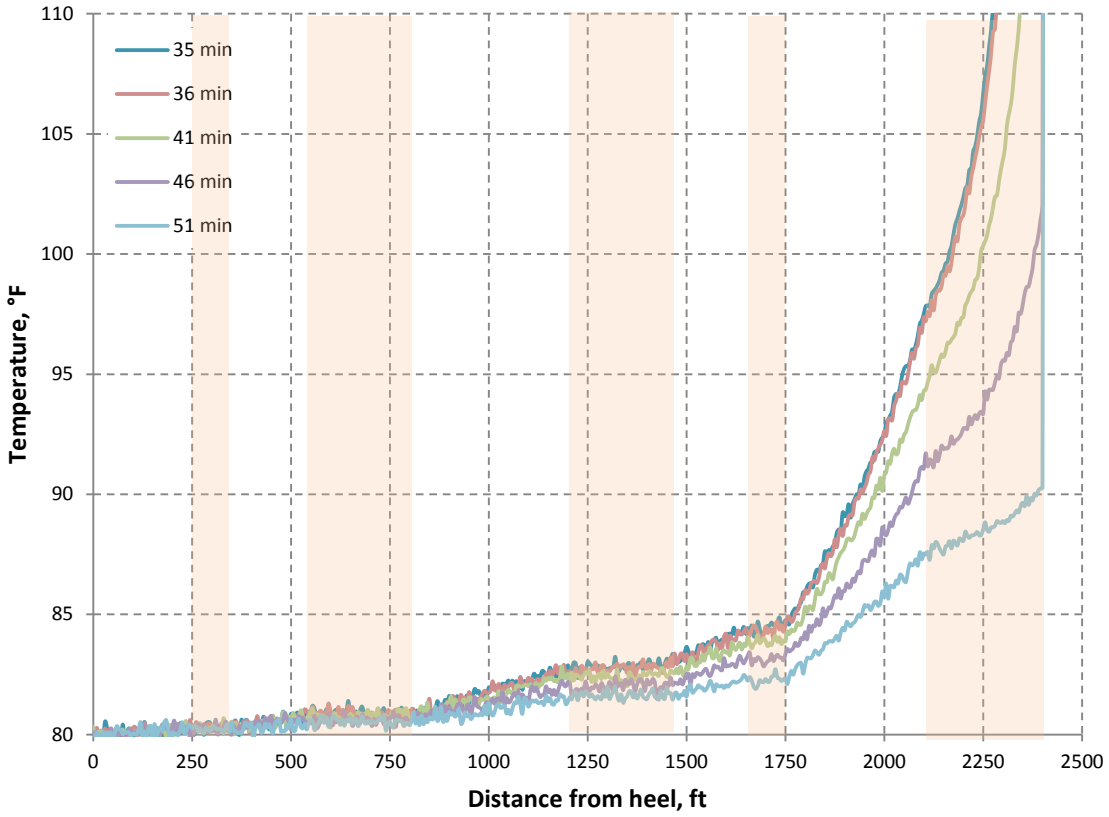

Fig. 5.25—Simulated wellbore temperature behavior right before and after applying the diversion.

Similar to the previous example, we consider the simulated temperature behavior as the observed data which is used to determine the injection profile after performing the de-noising and filtering process. **Fig. 5.26** shows the filtered temperature data while **Table 5.6** summarizes the inverse model calculated fluid fluxes right before and after applying the diversion. Again, the unit of the inverted fluid fluxes is bbl/min/ft.

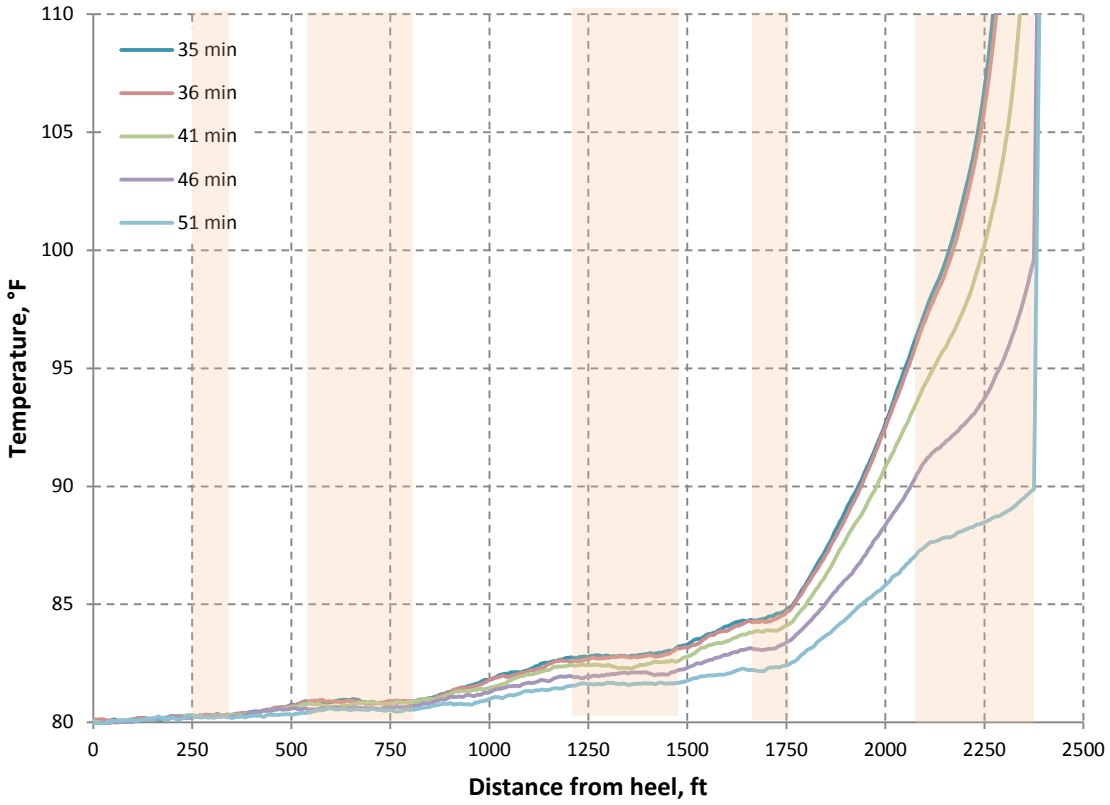

Fig. 5.26—Smoothed temperature data right before and after applying the diversion.

TABLE 5.6—INVERSION RESULTS BEFOR AND AFTER APPLYING THE DIVERSION

Time, min	Perf #1	Perf #2	Perf #3	Perf #4	Perf #5
35	0.0522	0.0068	0.0031	0.0158	0.0024
36	0.0125	0.0124	0.0064	0.0276	0.0043
41	0.0286	0.0100	0.0046	0.0162	0.0062
46	0.0345	0.0072	0.0032	0.0152	0.0081
51	0.0376	0.0062	0.0028	0.0147	0.0083

Using the similar approach as the previous example, the inverted injection profile and the pressure data can be used along with the calculated reservoir permeabilities from the previous section to monitor the skin evolution after applying the diversion. **Figs. 5.27, 29, 31, 33 and 35** shows the pressure and the injection rate history of each zone during the acid injection period, while **Figs. 5.28, 30, 32, 34 and 36** show the calculated skin

evolution. The red arrow in these figures shows when diversion was applied. **Table 5.7** also summarizes the calculated evolving skin factor for each zone. As we can observe, skin factor in the first zone jumps immediately after applying the diversion. This is because; this zone is the most permeable zone and therefore, it is taking most of the acid. When diversion is applied, almost all of the viscous fluid is injected into this zone and causes its skin factor to increase. As a result, the injectivity of this zone decreases and therefore, acid diverts to the other zones, specifically the fluid flux increases in the third and fifth zones which were not being treated well before the diversion was applied.

Comparing the calculated skin factors at the end of this treatment with the ones from the previous example reveals that the diversion was effective and improved the treatment results in this case.

Note that, the calculate skin evolutions show that even those zones that are not affected by the diversion show a small increase in their skin factor immediately after applying the diversion. This is not real and it is an artifact due to using the measured pressure at the heel to calculate the skin factor for each zone instead of using the local pressure measurement.

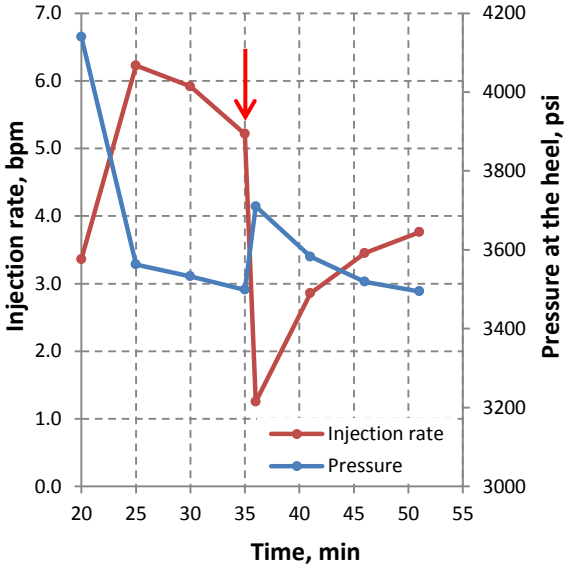

Fig. 5.27—Pressure and injection rate history of the first zone.

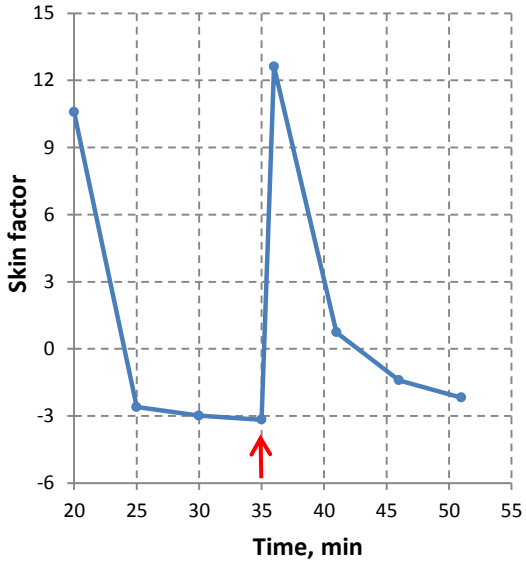

Fig. 5.28—Skin evolution of the first zone.

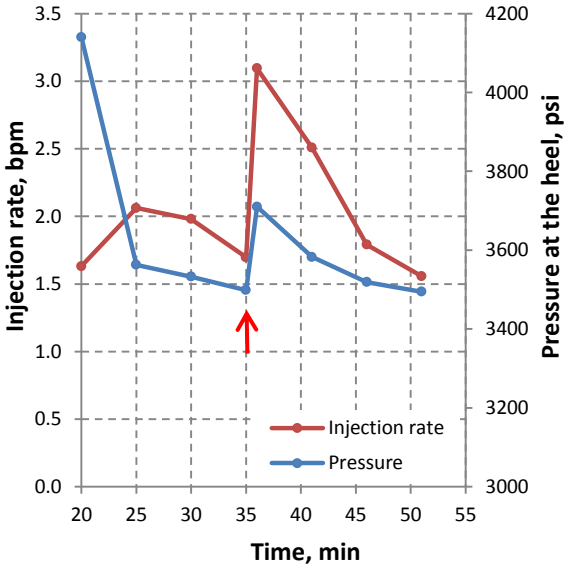

Fig. 5.29—Pressure and injection rate history of the second zone.

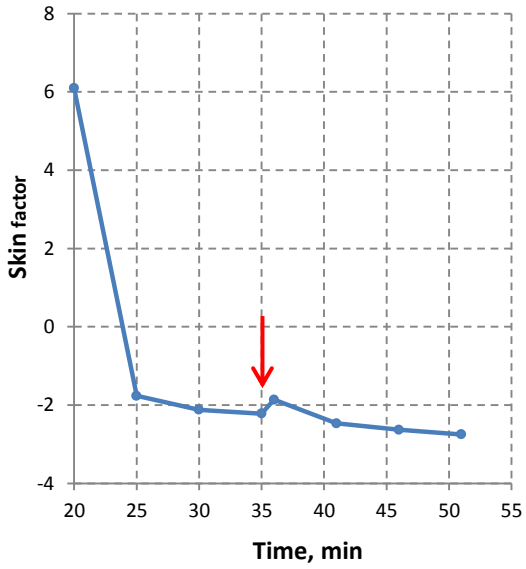

Fig. 5.30—Skin evolution of the second zone.

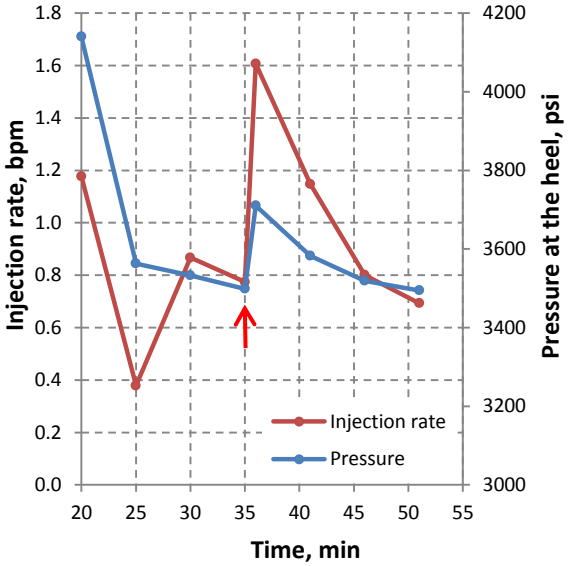

Fig. 5.31—Pressure and injection rate history of the third zone.

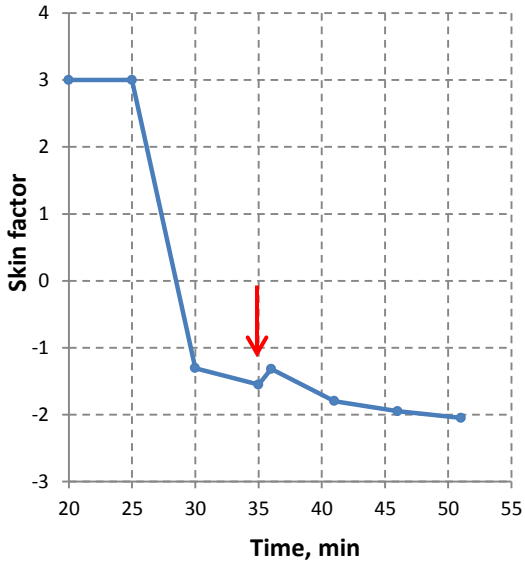

Fig. 5.32—Skin evolution of the third zone.

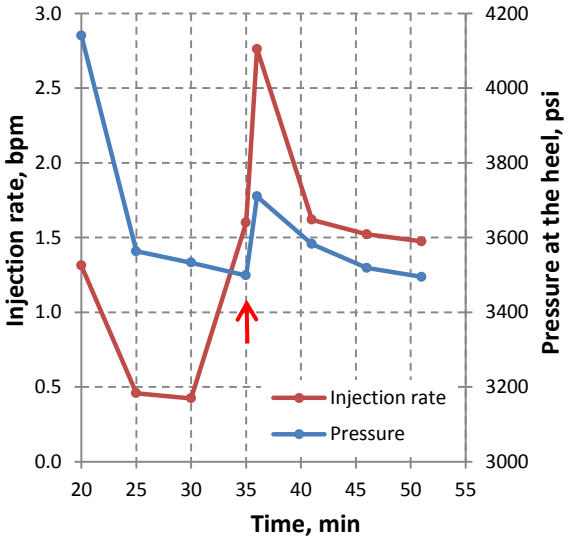

Fig. 5.33—Pressure and injection rate history of the fourth zone.

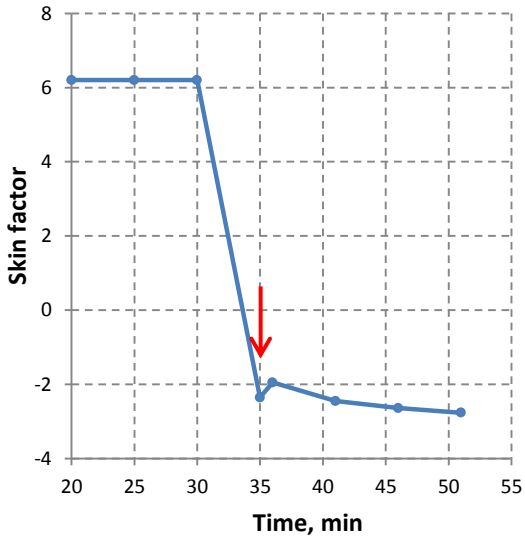

Fig. 5.34—Skin evolution of the fourth zone.

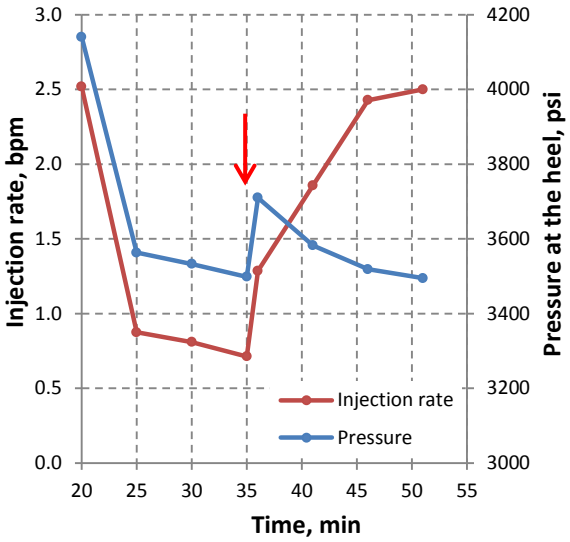

Fig. 5.35—Pressure and injection rate history of the fifth zone.

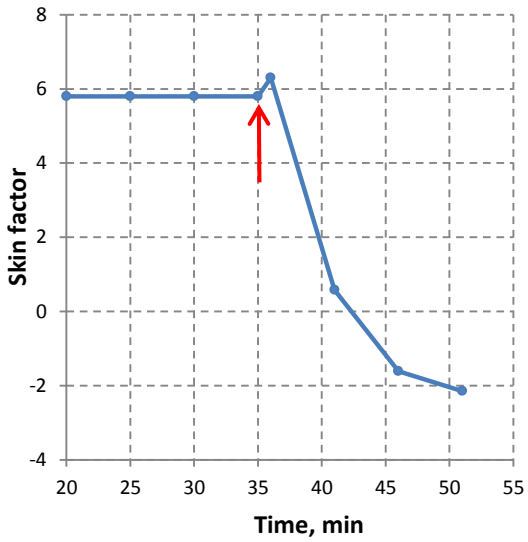

Fig. 5.36—Skin evolution of the fifth zone.

TABLE 5.7—SUMMARY OF THE SKIN EVOLUTION BEFOR AND AFTER APPLYING THE DIVERSION

	Perf #1	Perf #2	Perf #3	Perf #4	Perf #5
35	-3.2	-2.2	-1.6	-2.4	5.8
36	12.6	-1.9	-1.3	-2.0	6.3
41	0.7	-2.5	-1.8	-2.5	0.6
46	-1.4	-2.6	-2.0	-2.6	-1.6
51	-2.2	-2.8	-2.1	-2.8	-2.1

These two examples show that monitoring the evolution of the local skin factor during a treatment can help to evaluate the effectiveness of the individual fluid stages pumped during the treatment. This information can be used for assessing the effectiveness of diversion processes as well as optimizing future treatments.

6. CONCLUSIONS

We described the development of a new method for real-time monitoring of matrix acidizing in horizontal wells. With this method, treatment can be evaluated by calculating evolving skin factor along the wellbore using transient pressure and temperature data. As the skin factor is a reflection of the injectivity, it will indicate directly if the acid stimulation is effective and if diversion is successful.

We first presented a new method for quantifying the acid placement using dynamic temperature data measured by DTS or other tools. A forward model is developed to simulate the temperature behavior along the wellbore during both injection and shut-in periods. This model couples a wellbore and a near-wellbore thermal model considering the effect of both mass and heat transfer between the wellbore and the formation. The wellbore thermal model is used to solve the temperature profile along the wellbore where we measure the temperature by DTS. The model includes the effects of convection and conduction in the wellbore and conduction from the formation. The near-wellbore model is used to simulate the transient temperature response in the formation during treatment. The model includes the effects of convection and conduction in the near-wellbore region and also heat generated by the reaction between acid and rocks.

Both wellbore and near-wellbore models are validated separately. They are simplified to be able to be solved analytically, and then the numerical solutions validate against the analytical solutions. Furthermore, the coupled model is validated by comparing the results of the numerical solution of the coupled model with Ramey's analytical solution of the wellbore temperature during injection.

The developed forward model has been applied to several hypothetical cases to study the effects of acid distribution and diversion effectiveness on transient wellbore temperature behavior during both injection and shut-in periods. Results reveal that dynamic temperature data can provide us with enough information to identify the acid flow profile. Moreover, some sensitivity studies are performed to discuss the factors that affect the temperature behavior during treatment. It was found out that the interpretation of the temperature data can be challenging when injection rate is high due to fast wellbore cooling. In addition, results show that the interpretation of the temperature data is much easier when the temperature difference between injected acid and formation is high. It was also concluded that the formation type has an insignificant effect on temperature response since the higher reaction heat of dolomite causes a tiny increase in the peak in the near-wellbore temperature response and this has an insignificant effect on the temperature gradient at the wellbore.

In the next step, with the developed forward model, an inversion procedure is developed to interpret the acid distribution profile from the measure temperature profiles. With this procedure, both inversion methods (stochastic or gradient-based) can be applied. Inversion results revels that the proposed inversion procedure for interpreting the acid distribution from temperature data is accurate and reliable. Moreover, this procedure is fast and applicable for real-time monitoring of acid stimulation treatment.

The potential impact of sensor resolution, spatial data density and noise on the temperature data interpretation is investigated as well. Results indicate that temperature resolution and data noise level can have significant impacts on the interpretation results. It is concluded that the resolution of 0.01 °F is more preferable for interpretation, and a

temperature data with noise level up to ±0.2 °F can be still used to interpret the acid distribution during treatment, but data with noise level of ±0.5 °F or more is hard to be used for interpretation and leads to failure of inversion. To use the data with noise level of ±0.5 °F or more, it is necessary to filter the data and when data noise level is in an acceptable range, data filtering can significantly improve the interpretation accuracy.

In the final step of this work, we proposed an approach to estimate the reservoir permeability and the initial skin factor along the lateral from a step-rate test during pre-flush by mean of pressure and temperature data. Then we extend the real-time monitoring and evaluation of the acid stimulation treatment in horizontal wells to calculate the evolving skin factor as a function of injection time and location along the wellbore. The approach to monitor the evolving skin along the lateral is to use a proper pressure transient model to calculate skin factor by integrating the inversion results of the temperature data (acid injection profile) with either surface or bottomhole injection pressure. Examples are presented to illustrate the proposed acid stimulation monitoring procedure and the calculations in details.

REFERENCES

Behenna, F.R. 1994. Interpretation of Matrix Acidizing Treatment Using a Continuously Monitored Skin Factor. Paper SPE 27401 presented at the SPE Formation Damage Control Symposium, Lafayette, Louisiana, 7-10 February.

Clanton, R.W., Haney, J.A., Pruett, R., Wahl, C.L., Goiffon, J.J., and D. Gualtieri, D. 2006. Real-Time Monitoring of Acid Stimulation Using a Fiber-Optic DTS System. Paper SPE 100617 presented at the SPE Western Regional/AAPG Pacific Section/GSA Cordilleran Section Joint Meeting, Anchorage, Alaska, 8-10 May.

Clonts, M.D. and Ramey, H.J. Jr. 1986. Pressure-Transient Analysis for Wells with Horizontal Drainholes. Paper SPE 15116 presented at the SPE California Regional Meeting, Oakland, California, 2-4 April.

da Motta, E.P., dos Santos, J.A.C.M., Zhu, D., and Hill, A.D. 1997. Field Evaluation and Optimization of Matrix Acidizing Treatments. Paper SPE 37460 presented at the SPE Production Operations Symposium, Oklahoma City, Oklahoma, March 9-11.

Data-Gupta, A. and King, M. J. 2007. *Streamline Simulation: Theory and Practice*. Textbook Series, SPE, Richardson, Texas.

Economides, M.J., Hill, A.D., and Ehlig-Economides, C. 1993. *Petroleum Production Systems*. Upper Saddle River, New Jersey: Prentice Hall, Inc.

Glasbergen, G., Gualtieri, D., Trehan, R., Van Domelen, M., and Nelson, M. 2007. Real-Time Diversion Quantification and Optimization Using DTS. Paper SPE 110707 presented at the SPE Annual Technical Conference and Exhibition, Anaheim, California, 11-14 November.

Glasbergen, G., Gualtieri, D., Van Domelen, M., and Sierra, J. 2009a. Real-Time Fluid Distribution Determination in Matrix Treatments Using DTS. *SPE Production & Operations* **24** (1): 135-146. SPE-107775-PA.

Glasbergen, G., Yeager, V, Reyes, R, and Everett, D. 2009b. Fluid Diversion Monitoring: The Key to Treatments Optimization. Paper SPE 122353 presented at the SPE European Formation Damage Conference, Scheveningen, The Netherland, 27-29 May.

Hastings., W. K. 1970. Monte Carlo Sampling Methods Using Markov Chains and Their Applications. *Biometrika* **57** (1): 97–109.

Hill, A.D. and Zhu, D. 1996. Real-Time Monitoring of Matrix Acidizing Including the Effects of Diverting Agents. *SPEPF* **11** (2): 95-101. SPE-28548-PA.

Johnson, D., Sierra, J., Gualtieri, D., and Kaura, J. 2006. DTS Transient Analysis: A New Tool to Assess Well-Flow Dynamics. Paper SPE 103093 presented at the SPE Annual Technical Conference and Exhibition, San Antonio, Texas, 24-27 September.

Johnson, D., Sierra, J., Kaura, J., and Gualtieri, D. 2006. Successful Flow Profiling of Gas Wells Using Distributed Temperature Sensing Data. Paper SPE 103097 presented at the SPE Annual Technical Conference and Exhibition, San Antonio, Texas, USA, 24-27 September.

Kuchuk, F.J., Goode, P.A., Wilkinson, D.J., and Thambynayagam, R.K.M. 1991. Pressure-Transient Behavior of Horizontal Wells With and Without Gas Cap or Aquifer. *SPEFE* **6** (1): 86-94. SPE-17413-PA.

Lee, J., Rollins, J.B., and Spivey, J.P. 2003. *Pressure Transient Testing*. Textbook Series, SPE, Richardson, Texas.

Li, Z. 2010. Predicting Horizontal Well Flow Profiles and Well Optimization by Downhole Temperature and Pressure Data. PhD dissertation, Texas A&M University, College Station, Texas (December 2010).

Li, Z. and Zhu, D. 2010. Predicting Flow Profile of Horizontal Well by Downhole Pressure and Distributed-Temperature Data for Waterdrive Reservoir. *SPE Production & Operations* **25** (3): 296-304. SPE-124873-PA.

Ma, X., Al-Harbi, M., Datta-Gupta, A., and Efendiev, Y. 2008. An Efficient Two-Stage Sampling Method for Uncertainty Quantification in History Matching Geological Models. *SPE Journal* **13** (1): 77-87. SPE-102476-PA.

Mallat, S.G., 1998. *A Wavelet Tour of Signal Processing*. San Diego, California: Academic Press.

Marquardt, D.W. 1963. An Algorithm for Least-Squares Estimation of Nonlinear Parameters. *Journal of the Society for Industrial and Applied Mathematics* **11** (2): 431-441.

McLeod, H.O. and Coulter, A.W. 1969. The Stimulation Treatment Pressure Record: An Overlooked Formation Evaluation Tool. *JPT* **21** (8): 952-960. SPE-2287-PA.

Metropolis, N., Rosenbluth, A. W., Rosenbluth, M. N., Teller, A. H., and Teller, E. 1953. Equations of State Calculations by Fast Computing Machines. *Journal of Chemical Physics* **21** (6): 1087–1092.

Mishra, V., Zhu, D., and Hill, A.D. 2007. An Acid-Placement Model for Long Horizontal Wells in Carbonate Reservoirs. Paper SPE 107780 presented at the SPE European Formation Damage Conference, Scheveningen, The Netherlands, 30 May-1 June.

Montgomery, C.T., Jan, Y.M., and Niemeyer, B.L. 1995. Development of a Matrix Acidizing Stimulation Treatment Evaluation and Recording System. *SPEPF* **10** (4): 219-224. SPE-26579-PA.

Odeh, A.S. and Babu, D.K. 1990. Transient Flow Behavior of Horizontal Wells: Pressure Drawdown and Buildup Analysis. *SPEFE* **5** (1): 7-15. SPE-18802-PA.

Oliver, D. S., Cunha, L. B. and Reynolds, A. C. 1997. Markov chain Monte Carlo Methods for Conditioning a Permeability Field to Pressure Data. *Mathematical Geology* **29** (1): 61-91.

Oliver, D. S., Reynolds, A. C., Liu, N. 2008. *Theory for Petroleum Reservoir Characterization and History Matching*. Cambridge, UK: Cambridge University Press.

Ozkan, E, Raghvan, R., and Joshi, S.D. 1989. Horizontal Well Pressure Analysis. *SPEFE* **4** (4): 567-575. SPE-16378-PA.

Paccaloni, G. 1979a. Field History Verifies Control, Evaluation. *Oil and Gas Journal* **77** (48): 61-65.

Paccaloni, G. 1979b. New Method Proves Value of Stimulation Planning. *Oil and Gas Journal* **77** (47): 155-160.

Paccaloni, G. and Tambini, M. 1993. Advances in Matrix Stimulation Technology. *JPT* **45** (3): 256-263. SPE-20623-PA.

Prouvost, L.P. and Economides, M.J. 1987. Real-Time Evaluation of Matrix Acidizing Treatments. *Journal of Petroleum Science and Engineering* **4** (4): 401-407. SPE-17156-PA.

Prouvost, L.P. and Economides, M.J. 1989. Applications of Real-Time Matrix Acidizing Evaluation Methods. *SPEPE* **1** (2): 145-154.

Perry, R.H., Green, D.W., and Maloney, J.O. 1963. *Perry's Chemical Engineers' Handbook*. New York: McGraw-Hill Book Co.

Ramey, H. J. 1962. Wellbore Heat Transmission. *JPT* **14** (4): 427-435. SPE-96-PA.

Robert, C. and Casella, G. 1999. *Monte Carlo Statistical Methods*. New York: Springer-Verlag.

Sui, W. 2009. Determining Multilayer Formation Properties from Transient Temperature and Pressure Measurements. PhD dissertation, Texas A&M University, College Station, Texas (August 2009).

Sui, W., Zhu, D., Hill, A. D., and Ehlig-Economides, C. A. 2008a. Determining Multilayer Formation Properties From Transient Temperature and Pressure Measurements. Paper SPE 116270 presented at the SPE Annual Technical Conference and Exhibition, Denver, Colorado, 21-24 September.

Sui, W., Zhu, D., Hill, A. D., and Ehlig-Economides, C. A. 2008b. Model for Transient Temperature and Pressure Behavior in Commingled Vertical Wells. Paper SPE 115200 presented at the SPE Russian Oil and Gas Technical Conference and Exhibition, Moscow, Russia, 28-30 October.

Tan, X., Zhu, D., and Hill, A.D. 2009. Determining Acid Distribution Using Distributed Temperature Measurements. Paper SPE 124743 presented at the SPE Annual Technical Conference and Exhibition, New Orleans, Louisiana, 4-7 October.

Tan, X., Tabatabaei, M., Zhu, D., and Hill, A.D. 2011. Measurement of Acid Placement with Temperature Profiles. Paper SPE 144194 presented at the SPE European Formation Damage Conference, Noordwijk, The Netherland, 7-10 June.

Thomas, Jr., J., Frost, R.R., and Harvey, R.D., 1973. Thermal Conductivity of Carbonate Rocks. *Engineering Geology* **7**:3-12.

Wadsley, A.W. 2005. Markov Chain Monte Carlo Methods for Reserves Estimation. Paper SPE 10065 presented at the International Petroleum Technology Conference, Doha, Qatar, 21-23 November.

Wang, X., Lee, J., Thigpen, B., Vachon, G., Poland, S., and Norton, D. 2008. Modeling Flow Profile Using Distributed Temperature Sensor (DTS) System. Paper SPE 111790 presented at the SPE Intelligent Energy Conference and Exhibition, Amsterdam, The Netherlands, 25-27 February.

Yoshioka, K. 2007. Detection of Water or Gas Entry into Horizontal Wells by Using Permanent Downhole Monitoring System. PhD dissertation, Texas A&M University, College Station, Texas (May 2007).

Yoshioka, K., Zhu, D., and Hill, A. D. 2007a. A New Inversion Method to Interpret Flow Profiles from Distributed Temperature and Pressure Measurements in Horizontal Wells. *SPE Production & Operations* **24** (4): 510-521. SPE-109749-PA.

Yoshioka, K., Zhu, D., Hill, A. D., Dawkrajai, P., and Lake, L. W. 2007b. Prediction of Temperature Changes Caused by Water or Gas Entry Into a Horizontal Well. *SPE Production & Operations* **22** (4): 425-433. SPE-100209-PA.

Zhu, D., Hill, A.D., and da Motta, E.P. 1998. On-Site Evaluation of Acidizing Treatment of a Gas Reservoir. Paper SPE 39421 presented at the SPE Formation Damage Control Symposium, Lafayette, Louisiana, 18-19 February.

Zhu, D., Hill, A.D., and Looney, M.D. 2000. Evaluation of Acid Treatments in Horizontal Wells. Paper SPE 59804 presented at the SPE Permian Basin Oil and Gas Recovery Conference, Midland, Texas, 21-23 March.

VITA

Name:	Seyed Mohammad Tabatabaei Bafruei
Address:	Harold Vance Department of Petroleum Engineering Texas A&M University 3116 TAMU – 712 Richardson Building College Station, TX 77843-3116
Email Address:	mohammad.tabatabaei@pe.tamu.edu
Education:	B.S., Mechanical Engineering, Sharif University of Technology, Tehran, Iran, August 2006 B.S., Petroleum Engineering, Sharif University of Technology, Tehran, Iran, August 2006 M.S., Petroleum Engineering, University of Louisiana at Lafayette, LA, USA, August 2008 Ph.D., Petroleum Engineering, Texas A&M University, TX, USA, December 2011